Fluid Inerter Based Vibration Suppression: Modelling Methodology

By

XIAOFU LIU

Department of Mechanical Engineering
UNIVERSITY OF BRISTOL

A dissertation submitted to the University of Bristol in accordance with the requirements of the degree of DOCTOR OF PHILOSOPHY in the Faculty of Engineering.

MAY 2019

Word count: 47,524

Abstract

Inerter is the mechanical analogue of the capacitor via the force-current analogy. It has the property that the force across the terminals is proportional to their relative acceleration. Vibration absorbers with a combination of stiffness, damping and inertance have been shown to be effective through numerous theoretical studies.

A case study is carries out to investigate the potential reduction in road damage by incorporating the inerter element into truck suspension systems. Initially, quarter-car, pitch-plane and roll-plane models with two low-complexity inerter-based linear suspension layouts are investigated in the frequency domain. Reductions of the J_{95} road damage index for each model are identified against conventional parallel spring-damper truck suspension layouts. Subsequently, the nonlinearities of leaf springs are incorporated into the pitch-plane and roll-plane time-domain models. It has been verified that the benefits brought by the inerter integrated suspension are still present.

There are mainly two types of physical realisation for the inerter. Compared with flywheel-based inerters, the fluid-based forms have advantages of improved durability, structural simplicity, inherent damping and similarity with existing damper constructions. In this work, two prototypes of a helical-tube fluid inerter and a fluid-inerter integrated damping (FID) device are built for the modelling studies.

In order to improve the understanding of the physical behaviour of the fluid-based devices, especially caused by the hydraulic resistance and inertial effects in the external tube, this work proposes a comprehensive model identification methodology. Firstly, a modelling procedure is established, which allows the topological arrangement of the mechanical networks to be obtained by mapping the damping, inertance and stiffness effects directly to their respective hydraulic counterparts. Secondly, an experimental sequence is introduced, which separates the element-property identifications into smaller subsets. Meanwhile, an experimental set-up is introduced, where two pressure gauges are used to accurately measure the pressure drop across the external tube. Using the proposed modelling methodology, the theoretical models with improved confidence are obtained for a helical-tube fluid inerter prototype.

Furthermore, previous studies focused on accurate modelling of a specific fluid-based inerter device, while there has been no investigation on whether the dynamic models are still valid when its design parameters change. A model is termed here as being generalisable when it is able to sufficiently accurately characterise the terminal behaviour while allowing its design parameters to vary within their pre-defined ranges. Therefore, the generalisable model is developed for an example FID device design. The sources of remaining discrepancies are further analysed. The methodology to establish the generalisable model presented here is applicable to other design parameter selections as well as other designs of fluid-based vibration suppression devices.

Dedication and acknowledgements

Firstly, I would like to express my sincere gratitude to my supervisors, Dr Jason Zheng Jiang, for his countless support and encouragement throughout my doctoral studies. I also want to thank my co-supervisor, Dr Branislav Titurus, for his valuable guidance and insightful suggestions to my project. I extend the thanks to my previous co-supervisor, Dr Andrew Harrison, for his support and guidance to my work in the first year. The PhD would not have been possible without their dedication and help.

Second, I would like to thank all my colleagues working in Actlab. Prof. David Stoten, thank you for the experimental safety lessons. Dr Ying Zhang, Dr Yuan Li and Dr Jiannan Luo, thank you for the accompany and help in both the academic study and personal life. Many thanks also to Hui yuan, Tim Lewis, Kaiqiang Zhang, Yiyuan Li, Ming Zhu and Siming Chen, for their kindness and helpful discussion.

Furthermore, I would like to express my special thanks to my friend, Yi Liu, for introducing this valuable PhD opportunity to me, as well as all my friends in Bristol for sharing the moments of happiness during my 4 years here.

I would also like to thank Daniel, Clive, Mictroy and Guy, for their help and suggestions to the experimental works.

Last but not least, I am truly grateful to my parents for their constant support and deeply love throughout my entire life. Also, a huge thanks to my dear wife and son, love you both forever, you are the reason that I fight for.

XIAOFU LIU
May 2019

AUTHOR'S DECLARATION

I declare that the work in this dissertation was carried out in accordance with the requirements of the University's Regulations and Code of Practice for Research Degree Programmes and that it has not been submitted for any other academic award. Except where indicated by specific reference in the text, the work is the candidate's own work. Work done in collaboration with, or with the assistance of, others, is indicated as such. Any views expressed in the dissertation are those of the author.

SIGNED: [redacted] DATE: 06/05/2019

Journal publications

Liu, X., Titurus, B. and Jiang, J.Z., 2019. Generalisable model development for fluid-inerter integrated damping devices. *Mechanism and Machine Theory*, 137, pp.1-22.

Liu, X., Jiang, J.Z., Titurus, B. and Harrison, A., 2018. Model identification methodology for fluid-based inerters. *Mechanical Systems and Signal Processing*, 106, pp.479-494.

Conference publications

Liu, X., Jiang, J.Z., Titurus, B., Harrison, A.J. and McBryde, D., 2017. Testing and modelling of the damping effects for fluid-based inerters. *Procedia engineering*, 199, pp.435-440.

Jiang, J., Liu, X. and Harrison, A., 2015. Passive suspension incorporating inerters for road damage improvement of heavy vehicles. *In International Symposium on Dynamics of Vehicles on Road and Tracks*.

TABLE OF CONTENTS

List of Tables

List of Figures

Figure **Page**

Notation

In this work, the numerical subscripts of the hydraulic variables: pressure difference Δp, hydraulic resistance R, hydraulic inertance I and hydraulic compliance C denote different flow branches with corresponding flow rates Q in the hydraulic networks. Also, in equivalent mechanical networks, the numerical subscripts of the mechanical variables: relative velocity Δv, force F, damping c, inertance b and stiffness k indicate the specific hydraulic branches which caused corresponding mechanical effects. In addition, the abbreviations in subscripts: h indicates helical tube, io indicates inlet/outlet, v indicates needle valve, c indicates fluid compressibility, s indicates leakage, b indicates inertance, I indicates hydraulic inertance, and R indicates hydraulic resistance.

Chapter 3

J_{95}	The 95th percentile aggregate fourth power force
z_r	Vertical displacements of road surface
z_u	Vertical displacements of axle
z_s	Vertical displacements of vehicle body
m_u	Unsprung mass
m_s	Sprung mass
k_s	Static stiffness
c_s	Damper damping
k_t	Tyre stiffness
V	Vehicle speed
ω	Angular frequency
w	Spectrum slope
G_0	Road roughness
S_{A^4}	Aggregate fourth power tyre force
F_s	Static tyre force
F_{ENV}	The upper and lower boundary for the envelope
β	The spring parameter for the rate of hysteresis
k_u	Upper envelope stiffness
k_l	Lower envelope stiffness
F_u	Upper envelope friction
F_l	Lower envelope friction
a	Half wheelbase

r	Sprung mass distributed ratio
I_s	Sprung mass moment of inertia
T_{12}	Time delay
b	Inertance
l_t	Distances between tyres and unsprung mass roll centre
l_s	Distances between suspensions and sprung mass roll centre
h_s	Height of sprung mass roll centre
h_{sr}	Height of sprung mass centre of gravity
h_u	Height of unsprung mass centre of gravity
θ_s	Sprung mass roll angle
θ_u	Unsprung mass roll angle
I_u	Unsprung mass moment of inertia
n	Wave number
q_s	Vehicle lateral acceleration
R_u	Roll stiffness about the unsprung mass roll centre
R_s	Roll stiffness about the sprung mass roll centre
f_0	Lower boundary of frequency

Chapter 4

B	Bulk modulus
V	Volume of the fluid
δV	Volume change of the fluid
δp	Pressure change of the fluid
$\dot{V}$	Total volumetric flow rate between the cylinder chambers
$\dot{p}$	Time derivative of the pressure
p_1, p_2	Absolute pressure of the fluid in each chamber
x_p	Piston displacement
$\dot{x}_p$	Piston velocity
A_p	Effective area of the piston
Q_j	Flow rate of the jth path
N_F	Number of flow paths
Q_p	Volumetric flow rate caused by the piston moving
Q_N	Total flow rate thought the flow paths
Q_B	Volumetric flow rate caused by the fluid compressibility
q	Constant regard to the characteristics of the flow resistances
F	Force
Δv	Relative velocity
k	Mechanical stiffness
c	Mechanical damping
m	Mechanical inertia
b	Mechanical inertance
Δp	Pressure difference
Q	Flow rate

C Hydraulic compliance
R Hydraulic resistance
I Hydraulic inertance
F_p Terminal force
Δv_p Relative terminal velocity
F_H Hydraulic force

Chapter 5

d_1 Cylinder bore size
d_0 Cylinder rod diameter
L_s Cylinder stroke
L Cylinder chamber length
f_b Break frequency
c' Linearised parasitic damping coefficient
ω Frequency in rad/s
ρ Fluid density
l Total length of the external tube
D_h Tube hydraulic diameter
R Tube helix radius
A_1 Effective piston area
A_2 Tube cross-sectional area
d_0 Rod diameter
d_1 Cylinder diameter
d_2 Tube inner diameter
N No. of tube turns
t Tube thickness
μ Fluid dynamic viscosity
N_u The number of U-bends
N_s The number of straight tubes
l_u Length of each U-bend
l_s Length of each straight tube
F_h Theoretical tube damping force by the helical-tube design
F_m Theoretical tube damping force by the meander-tube design
x Strut displacement
F Strut force
V Voltage
h Head of water

Chapter 6

Δv_c Constant velocity
f Friction
V_1, V_2 The volume of cylinder each chamber
V The total volume of cylinder chambers

B_w	Nominal bulk modulus of water
B_a	Nominal bulk modulus of air
B_e	Effective bulk modulus
V_a	Volume of air
Re	Reynold number
u	Flow velocity
λ	Curvature ratio
Re_c	Critical Reynold number
f_c	Fanning friction factor
D	Tube helix diameter

Chapter 7

k_s	Coupler stiffness
p	Backlash
K_v	Valve flow coefficient
h	Valve lift
n_a	Valve opening level

Abbreviations

FID	Fluid-inerter integrated damping
DOF	Degrees-of-freedom
TMDI	Tuned mass-damper-inerter
TMD	Tuned mass-damper
TID	Tuned-inerter-damper
FSI	Fixed-size-inerter
VD	Viscous damper
MLG	Main-landing-gear
TVMD	Tuned viscous mass damper
CVT	Continuously variable transmission
FRC	Frequency response curve
PVID	Parallel Viscous Inerter Damper
EIMD	Electromagnetic inertial mass damper
ACTLab	Automatic control and testing laboratory
LVDT	Linear Variable Differential Transformer
LAR	Least Absolute Residuals

CHAPTER 1

INTRODUCTION

1.1 Background

Vibration is defined as the oscillation of a mechanical system about its equilibrium position, which is one of the most notable phenomena for engineering [1]. Some vibration can be useful, such as the voice coil in loudspeaker or the tuning fork. However, more vibrations are harmful to either the environment or the human beings. Numerous examples of such vibration are shown in a wide range of areas, including the economic losses due to road damage by heavy vehicles or the track wear by rail vehicles; as well as the safety issues of building structures subject to earthquakes or aircraft during landing. Therefore, to mitigate the undesired vibration by using effective and reliable vibration suppression systems is crucially important in engineering studies.

A conventional vibration control system is usually constructed by chosen numbers of spring, damper and mass elements. According to whether the energy supply is required or not, the control system can be classified into three groups: active, semi-active, and passive. Even though the active or semi-active control usually bring the best vibration suppression performance, the passive control has the advantage of stability, reliability and low cost. While the passive control is still widely accepted in most areas, the relevant investigations have been restricted to parameter studies and nonlinearity analysis due to the limitation of device structure and the avaliable network layouts of existing elements. Since inerter was first introduced in 2002 [2], using inerter-based vibration absorber for passive vibration control has become a popular research topic.

The inerter is a novel element for vibration control in mechanical system, which has the property that the force through the device is proportional to the relative acceleration across the terminals [2]. The proportional coefficient is defined as inertance. Based on the force-current analogy, the inerter is the true mechanical dual of a capacitor. Unlike the mass element, it has

two movable terminals. The introduction of the inerter element fundamentally expanded the range of achievable dynamic properties that can be achieved passively. Incorporating inerter(s) into a vibration suppression system is deemed as beneficial based on large number of theoretical works in various areas, such as the road vehicles, railway vehicles, tall buildings, cables of cable-supported bridge and aeroplane landing gears.

Physical realisations of inerter take different forms, but most of those fall into two categories: the flywheel-based and fluid-based. The flywheel-based inerter works by driving a flywheel through a transmission mechanism, such as rack-and-pinion or ball-screw, to provide amplified inertance. Such device has been successfully applied in the suspension of Formula One racing cars since 2005 [3]. However, these transmission mechanisms are originally designed for precise positioning, which limits the maximum load that can be applied as the large vibration force could lead to excessive wear of the transmission mechanism. This is the key factor restricts the real applications of inerter-based vibration absorbers only in racing industry where the device can be replaced after every race.

On the other hand, the fluid-based inerters were recently introduced, which have natural crossover with existing damping design, and hence will have higher load capability. Other benefits include durability, structural simplicity, and the convenience to integrate with other damping effects (e.g. piston valve damping). The device inertance is generated by the acceleration of the mass fluid flowing through the external tube channel. While there are multiple designs of the fluid-based inerter, this work focuses on the study of a helical-tube fluid inerter design.

The previous works of fluid-based inerter have shown noticeable discrepancies between the experimental results and established models, especially for the damping effects [4]. This work aims to establish a lumped parameter hydraulic model, and an equivalent mechanical model for a helical-tube fluid inerter. By using these two models, the damping, inertance and stiffness effects in the mechanical network can be linked directly with the resistances, inertances and compliances in the hydraulic system. This analogy will not only help to understand the properties of fluid-based inerters better but also facilitates future design of hydraulic vibration absorption systems. Meanwhile, a system identification procedure for fluid-based devices is presented. Following this procedure, the friction, stiffness and various damping effects are identified, separately, for more accurate estimation of each parameter. Moreover, to measure the pressure drop across the external tube more precisely, two pressure gauges are fitted at the inlet and outlet. As a result, a nonlinear model that can accurately characterise the dynamic properties of a helical-tube fluid inerter prototype has been established.

Furthermore, in previous works [4, 5], the presented models are developed for specific fluid inerter design parameter settings, and several other designs integrating both fluid inertance and orifice induced damping have also been introduced, which are phrased as fluid-inerter integrated damping (FID) devices here. To date, no investigation on the terminal dynamic behaviour of FID device has been carried out. Therefore, this work aims to establish an approach to develop a model

for an example FID device design with verified accuracy while allowing the key design parameters to change within their pre-defined ranges, a type of model termed as generalisable models in this work. In order to conveniently adjust the piston valve damping property for model identification, a bypass needle valve design is adopted in the test rig design. A methodology for developing a generalisable model will also be demonstrated, with the key design parameters of the helical tube and valve damping changing within their respective pre-determined ranges. The established model will then be validated by comparing its dynamic responses with the experimental results obtained for two additional design parameter settings. The approach developed in this work for generalisable model establishment uses the analogy between the hydraulic and equivalent mechanical networks, as well as tailored experiments to identify the properties of elements in such networks. While there exist other models and methods, the developed approach has the advantages of providing more physical insights which link the physical hydraulic elements with the device terminal force-velocity behaviour, effectively reducing the required experimental effort because smaller subsets of element properties can be identified separately, and be directly applied to the design and analysis of more complex damping systems.

It is noted that this thesis incorporates material from four published papers by the author, which are listed in page vii.

1.2 Thesis outline

This thesis is organised as follows.

Chapter 2 presents the review of associated literature regarding the concept of inerter based on the analogy between the mechanical and electrical networks. This is followed by a large number of theoretical applications showing the verified benefits of inerter-based vibration suppression approach in multiple areas. Further review of studies introduce the physical realisations of inerter, along with the modelling and testing of inerter devices for each realisation. The motivation of this work will then be addressed based on the reviewed literature and existing problems.

A numerical case study of truck suspension incorporating inerters to minimise road damage is presented in Chapter 3. While comprehensive analysis and parameter optimisation of selected vehicle models are carried out to verify the advantage of using inerter in the suspension, the results will be used to facilitate the later modelling process of the inerter-based devices, and motivate the research focus of FID device in later chapters.

Based on the analogy between the mechanical and hydraulic networks, Chapter 4 first build the correspondence between the mechanical and hydraulic elements by applying the physical relationships between the cross/through variables, which is used for the modelling of fluid-based vibration suppression devices. Then the introduction to the working principle of fluid-based inerters is followed by the construction of the hydraulic network of the design. The equivalent mechanical network is also derived through the network synthesis method. Similarly, the same

procedure is used to develop the hydraulic and mechanical networks for the conceptual design of the FID device.

On the basis of the schematics and corresponding networks of the fluid-based inerter devices presented in Chapter 4, Chapter 5 develops the prototype and test rig for a helical-tube fluid inerter with selected design parameters, which will be used for experimental tests in Chapter 6. Subsequently, a compact helical-tube fluid inerter is built for discussion of the possibility of incorporating inerter into existing damper device, and a meander-tube fluid inerter is introduced for damping effects study. The experimental tests of these alternative designs of fluid-based inerter will be considered for future work. Moreover, the prototype and fit-for-purpose test rig of a specific helical-tube FID device is developed based on the the schematics and corresponding networks introduced in Chapter 4. In the end, the calibration of the equipped measuring instruments in the test rig are carried out.

In Chapter 6, based on the helical-tube fluid inerter prototype built in Chapter 5, a series of constant velocity tests are used to identify the friction and various damping effects of the fluid-based inerter model constructed in Chapter 4. Then, the identification of the stiffness effect is carried out by using sinusoidal wave tests to complete the full dynamic model. Furthermore, the comparison between the theoretical model and experimental data at different amplitudes and frequencies is presented, followed by analysis of the remaining discrepancies.

According to the altered flow distribution and mechanical properties in the FID device prototype built in Chapter 5, Chapter 7 firstly complete the mechanical network characterising the device's terminal behaviour and establishes a model identification methodology for each key element in the network. The schematic diagrams, hydraulic networks and mechanical networks are systematically used to illustrate each test configuration for properties' identification. Moreover, the key design parameters' variation and the corresponding tests are explained. Results of the properties' identification and the influence of design parameters on damping properties are presented and discussed. Consequently, the generalisable model of the FID device is established and experimentally verified using the dynamic test data of two additional design parameter settings.

Finally, the conclusions are summarised in Section 8, along with a list of potential future works.

CHAPTER 2

LITERATURE REVIEW

2.1 Overview

There are three classical mechanical modelling elements that can be used for vibration suppression: the spring, damper and mass. The spring is an elastic element that stores the potential energy from vibration input, the damper is a dissipative element that converts the input energy into heat, and the mass is an inertial element that stores the input energy as kinetic energy [6–8]. Both the spring and damper elements can be realised as individual vibration control devices, while the mass is restricted by its one-terminal property, which can only be used for vibration suppression when combining with the spring(s) and/or damper(s). Recently, the inerter [2] was introduced as an alternative inertial element with two terminals, and the corresponding physical device was also proven to be beneficial for vibration suppression.

In this chapter, the review of associated literature is presented to first introduce the concept of inerter based on the analogy between the mechanical and electrical networks. Then, a large number of theoretical applications are presented to illustrate the benefits of inerter-based vibration suppression approach in multiple areas. This is followed by further review of the research on the inerter physical realisations; as well as the modelling and testing of inerter device realisations. In the end, based on the previous results and identified problems, the motivation for this work will be explained.

2.2 The inerter concept

The inerter is a novel element for vibration control in mechanical system, which was introduced by Smith in 2002 [2]. Different from the mass element, the inerter has two terminals, with the

property that the applied force is proportional to the relative acceleration across the element terminals [9].

The concept of inerter was inspired by the force-current analogy between the mechanical and electrical networks [10], which can be represented by the following correspondences [2]:

Mechanical		**Electrical**
Force (F)	$\Longleftrightarrow$	Current (I)
Velocity (v)	$\Longleftrightarrow$	Voltage (V)
Mechanical ground	$\Longleftrightarrow$	Electrical ground
Kinetic energy	$\Longleftrightarrow$	Electrical energy
Potential energy	$\Longleftrightarrow$	Magnetic energy
Spring (k)	$\Longleftrightarrow$	Inductor (L)
Damper (c)	$\Longleftrightarrow$	Resistor (R)
Mass (m)	$\Longleftrightarrow$	Capacitor (C)

As it is shown, in the mechanical network, the two-terminal connected elements spring (k) and damper (c) are equivalent to the inductor (L) and resistor (R) in the electrical network. However, the mass element in mechanical network has only one terminal due to the relative velocity across it is always zero, which generally does not correspond to the capacitor in electrical network with two terminals. The inerter was introduced to complete the analogy between these two networks. Based on the definitions of through and across variables in [10], the force (F) and current (I) are through variables that require only one measurement point inside the system, while the velocity (v) and voltage (V) are across variables that are measured by the difference between two points outside the system (e.g. terminals). These concepts can be used to link the corresponding elements, respectively, and preserve the topological connection between the mechanical and electrical networks [11].

With the inerter involved, the analogy is updated as illustrated in Fig. 2.1, where the admittance $Y(s)$ is defined as the ratio of applied force on the element (F) to relative velocity across the element ($\Delta v = v_2 - v_1$) and s denotes a complex number [2]. The defining force through each element has the proportional relationship with the relative displacement, acceleration and velocity for the spring, inerter and damper, respectively. The corresponding proportional coefficients are stiffness (k), inertance (b) and damping (c), with units of N/m, kg and Ns/m. The symbol of inerter is chosen to be a flywheel, which will be used throughout this work.

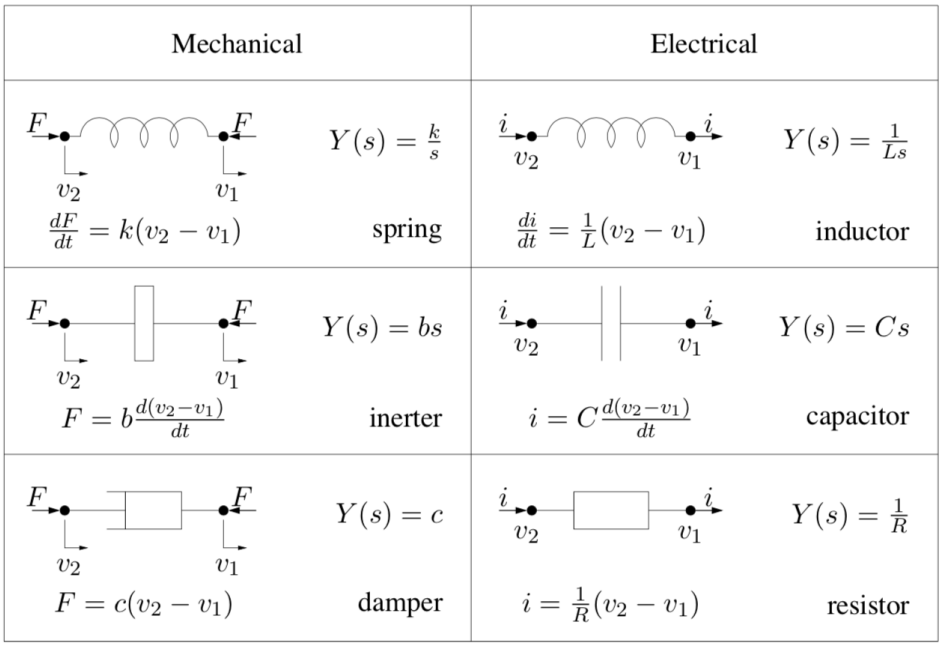

Figure 2.1: Analogy between mechanical and electrical networks with corresponding element symbols and definition equations with admittance $Y(s)$ as proposed in [2].

2.3 Applications of inerter

The inerter was first used in the suspension of Formula One racing car in 2005, where it helped McLaren team to win the Spanish Grand Prix. However, the name 'J-damper' was known by public until a few articles in *Autosport* revealed the true identity of the inerter in 2008, e.g. [3, 9]. After, the promising benefits of incorporating inerter(s) into vibration suppression systems have been demonstrated in various applications, which spread over a wide range of areas. Selected literature is reviewed in this section, including railway engineering, civil engineering aerospace engineering and automotive engineering.

2.3.1 Railway engineering

Using inerter in train suspension systems was investigated using one-wheel train model by Wang et al. [12], with conclusions confirming the advantages on both the passenger comfort and dynamic wheel load by applying higher-order controller. The realisation of optimum admittance was also proven to be achievable through Bott-Duffin methods. Meanwhile, Wang and Minkai [13] successfully verified the benefits for lateral stability of train suspension system employing inerter with 12 degrees-of-freedom (DOF) train model and 16-DOF train model. Further work carried out by Wang et al. [14] with a 28-DOF full-train model, concluded that the critical speed, settling time and passenger comfort can be all effectively improved, compared with the conventional suspension layout. Subsequently, Jiang et al. [15] investigated the 7-DOF plain-view train model

and found that the reduction of lateral body movement and acceleration can be achieved by employing the inerter into the secondary train suspension systems. Also, the study of side-view model proved the benefits of using inerter to raise the vertical ride comfort. Afterwards, Jiang et al. [16, 17] continued to investigate the two-axle railway vehicle models. The results indicated that up to 39% and 12.2% improvement of the lateral and vertical ride comfort can be potentially obtained by employing the inerters in both the lateral and vertical suspensions. Recently, a work by Lewis et al. [18] proves that incorporating inerter in the lateral suspension of trains is able to improve the passenger comfort by up to 43% and reduce the track wear at the same time.

2.3.2 Civil engineering

Since the inerter was introduced, a large amount of studies have been carried out on the potential benefits to employ inerter (or similar inertial device) in the vibration suppression systems of the civil engineering structures. Wang et al. [19] identified the potential improvement due to using inerter in 1-DOF and 2-DOF building models to reduce the vibrations caused by traffic and earthquakes. An advanced tuned mass-damper-inerter (TMDI) was introduced by Marian and Giaralis [20]. In comparison with the traditional tuned mass-damper (TMD), this TMDI could reduce the vibration from randomly support-excited chain-like structural systems with lighter weight, alternatively, it could improve the performance with the same total weight. In the meantime, Lazar et al. [21] studied the potential of reducing the vibrations from base excitation inputs, such as earthquakes, by using the Tuned-Inerter-Damper (TID) in a multi-storey building model. In the work of Brzeski et al. [22], a device connecting the additional viscous damper and inerter to the TMD was introduced and the influence of the attachment stiffness was also assessed. Another Fixed-Size-Inerter (FSI) concept was proposed by Zhang et al. [23] to diminish the maximum relative displacement of the 3-storey building, and the earthquake input signals was used to validate the performance benefits of the proposed device. More recently, the benefits of replacing TMD with lighter TMDI to reduce the peak top-floor acceleration resulting from wind-induced oscillations was verified by Giaralis and Petrini [24].

Moreover, Lazar et al. [25] investigated the possibility to replace the viscous damper (VD) by TID to control the vibration of the bridge cables. The results confirmed advantages of the TID, including the ability to overcome the maximum level modal damping limitation provided by the VD when connected to a specified position. Afterwards, a systematic approach was presented by Luo et al. [26] to identify the beneficial vibration controller layout for the cable vibration suppression. Applying this methods, several optimum inerter-based layouts were identified and verified to improve the cable critical damping ratio when compared with the traditional VD.

2.3.3 Aerospace engineering

In the work by Dong et al. [27], the inerter involved in the suspension system was found to be able to improve the shimmy of landing gear performance. The torsional vibration models with

and without lateral flexibility were both studied to conclude that the inerter could effectively reduce the corresponding natural frequency and settling time within certain range of inertances. Subsequently, incorporating inerter to the landing gear shimmy-suppression device was further studied by Li et al. [28] to identify the advantage of inerter involved layouts when compared to the optimised spring-damper layout. The results demonstrated the 16.7% decrease of peak amplitude and up to 57.3% improvement of the settling time for the torsional-yaw motion. Following this work, Li et al. [29] also investigated the benefits of two proposed inerter-based layouts for shimmy-suppression device on a main-landing-gear (MLG) system. This research showed reduced lower bound on the maximum zero-shimmy region and raising the maximum width in damping of the zero-shimmy region. Furthermore, adding the additional inerter into the landing gear shock strut was proven to be beneficial for the touchdown performance, by Li et al. [30], while the improvements of the strut efficiency, maximum strut load, and maximum strut stroke were identified as well.

2.3.4 Automotive engineering

The performance benefits in passive vehicle suspensions employing inerters has been identified by Smith and Wang [31]. The root-mean-square body acceleration (ride comfort) J_1, dynamic tyre load (tyre grip) J_3 and dynamic load carrying (handling) J_5 performances of a quarter-car model were studied with various inerter involved suspension struts (layouts S2-S8 in Fig. 2.2), and compared with the conventional strut (layout S1 in Fig. 2.2). The optimisation results showed that up to 10% improvements can be achieved. Similar results were obtained for the full-car model simulations. It is noted that the listed strut layouts in Fig. 2.2 are commonly adopted for vehicle suspension investigations, where the S1, S3, S4 will be particularly studied in Chapter 3 for heavy vehicle application. In 2009, Scheibe and Smith [32] analytically solved the global optima of the J_1, J_3 criteria and their combination. In comparison with of the same strut layout as in [31], the optimisation results of J_1 and J_3 in [31] therefore can be proved as global optima for different sets of parameter values. More importantly, the analytical solution based on the quarter-car model parameters and the suspension static stiffness were much less time-consuming than the previous numerical optimisation studies for other sets of vehicle parameters. Kuznetsov et al. [33] also found the analytical solution for optimisation of the ride comfort based on the ISO 2631 standard. Subsequently, Li et al. [34] carried out the multi-objective parametric optimisation of the J_1, J_3 and suspension deflection M_3 criteria, where M_3 is measured by the standard H_2 norm of the suspension relative displacement. The Chebyshev goal programming approach was used to balance these 3 objectives. The numerical results showed that the proposed inerter-based suspension improves J_1 and J_3, while keeping M_3 constant when compared with the conventional passive suspension. In the meantime, Hu et al. [35] investigated all combinations of any two of the performance measures J_1, J_3 and M_3. The conclusions also indicated that the suspension deflection could be set as a constraint to maximise the improvement of J_1 and J_3.

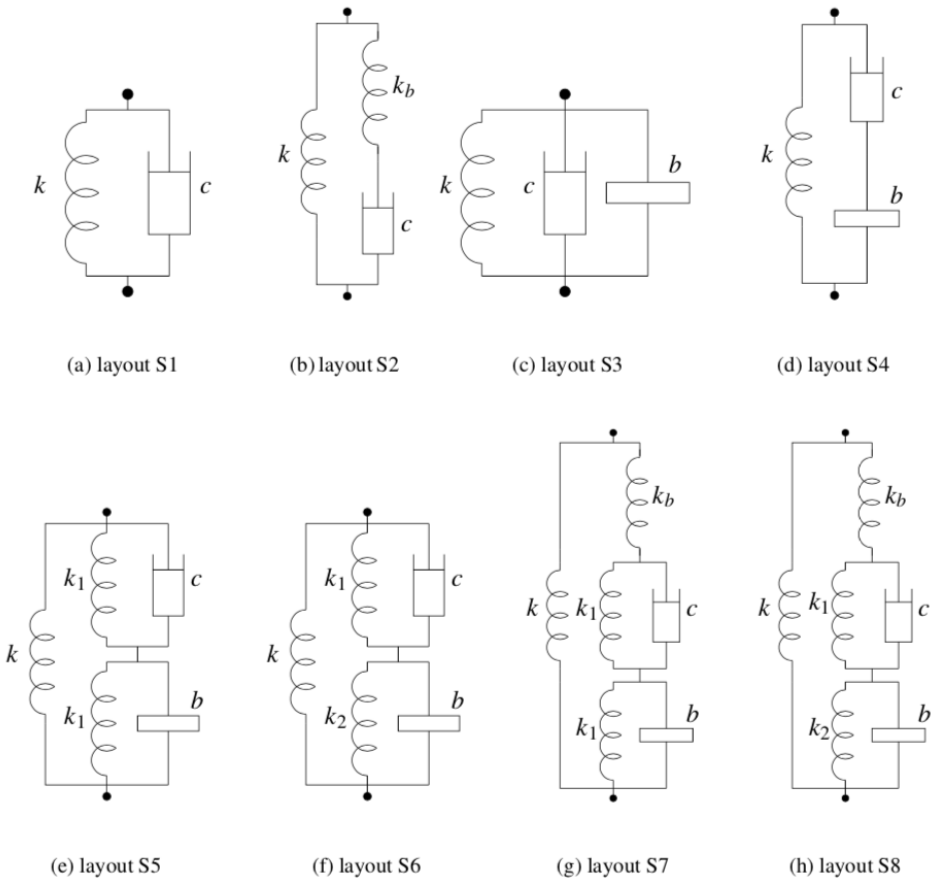

Figure 2.2: Candidate suspension strut layouts for vehicle applications as introduced in [31].

Furthermore, the semi-active vehicle suspension with inerter were studied by Zhang et al. [36] and Chen et al. [37], comparing these with the ordinary semi-active suspension and passive suspension, respectively. Significant performance benefits of ride comfort, suspension deflection and tyre grip were identified for the inerter-based semi-active suspension. Apart from the ride comfort and handling performance of the passenger vehicles, the dynamic tyre load of trucks were also investigated in [38, 39] to verify the the advantages of inerter-based suspension for heavy vehicles. Another practical and important performance index for heavy vehicles is the road damage, which is not only related to the economic benefits, but also affects the safety of the vehicles and passengers. Therefore, a numerical case study of the truck suspension design to minimise road damage will be presented in Chapter 3 to provide an evidence of the promising applications of the inerter-based suspensions in automotive area.

2.4 Physical realisation of inerters

The physical realisations of the inerters may be classified into two main types, the flywheel-based and the fluid-based. For flywheel-based inerters, multiple physical realisations were introduced with model parameters identified via experimental testing [40–45]. Effects of nonlinearities of these realisations, such as backlash and friction, were also investigated [12, 46]. On the other hand, the helical-tube fluid inerter, as a typical fluid-based design, was initially discussed in [4]. It has the advantages of durability, structural simplicity and low cost, compared to the flywheel-based design. In addition, there are also other alternative designs of the inerter, such as the combined hydraulic-mechanical and mechatronic inerters [47, 48].

2.4.1 Flywheel-based inerter

In this class, there are mainly two types of designs for the flywheel-based inerter. One is the rack-and-pinion inerter, which was first introduced together with the inerter concept by Smith [2]. As shown in Fig. 2.3, the flywheel is driven by the piston rod (terminal 2) moving through a rack, pinions and gear. The ratio of the inertance to the overall mass depends on the size of the pinions, gear and flywheel. The force (F) applied through the inerter is defined as [2]:

$$F = m\left(\frac{\gamma}{r_3}\right)^2\left(\frac{r_2}{r_1}\right)^2\dot{v} \tag{2.1}$$

where γ is the radius of the flywheel, r_3 is the radius of the flywheel pinion, r_2 is the radius of the gear wheel, r_1 is the radius of the rack pinion and $\dot{v}$ is the relative terminal acceleration. Therefore, the inertance b is equal to $m\left(\frac{\gamma}{r_3}\right)^2\left(\frac{r_2}{r_1}\right)^2$, where $\left(\frac{\gamma}{r_3}\right)^2\left(\frac{r_2}{r_1}\right)^2$ represents the inertance to mass ratio. A major advantage of inerter is that it can generate large inertial force while keeping small the overall mass of the device. To this end, all the rack-and-pinion parameters can be simply adjusted to meet the expected inertance requirements.

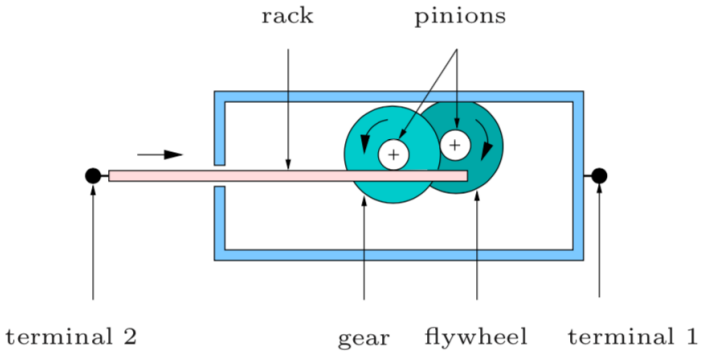

Figure 2.3: Schematic of the rack-and-pinion inerter adopted from [2].

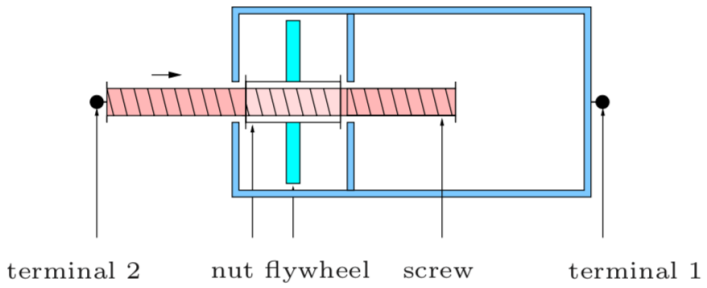

Figure 2.4: Schematic of the ball-screw inerter adopted from [40].

The other design is the ball-screw inerter, which was proposed later in [49]. As the schematic shows in Fig. 2.4, the flywheel is fixed to the nut, and the moving ball screw drives the nut and flywheel to rotate. The applied force (F) through the device is defined as [49]:

$$F = m\gamma^2\left(\frac{2\pi}{p}\right)^2\dot{v} \tag{2.2}$$

where p is the pitch of the screw. Therefore, the inertance to mass ratio is equal to $\gamma^2(2\pi/p)^2$, in which the γ and p are adjustable to alter the inertance.

The prototypes of both designs were build in Engineering Department of Cambridge University [40] as shown in Fig. 2.5, and patented by Malcolm [49] The experimental testing was carried out to verify the admittance of the two prototypes by using the standard hydraulic damper test rig. A buffer network of parallel spring-damper was employed in series with the tested inerter. It was used to overcome the nonlinear issues caused by the backlash in the device. With the updated model incorporating the optimised levels of backlash, the admittance of the tested devices was demonstrated to be the same as for the ideal inerter within the frequency from 1 to 10 Hz.

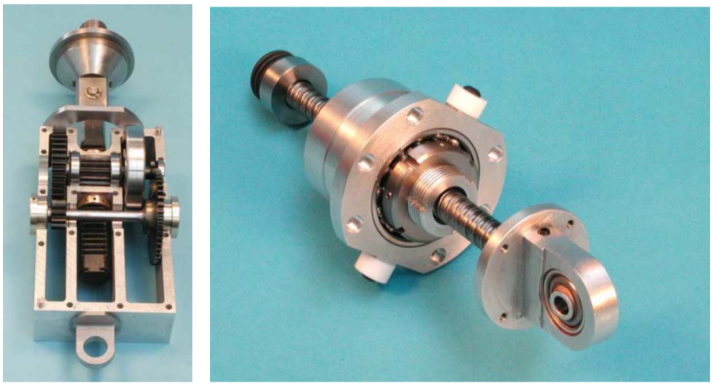

Figure 2.5: The prototypes of the rack-and-pinion inerter (left) and the ball-screw inerter (right) built in Cambridge University [40].

Subsequently, the ball-screw design was treated as a mass amplifier and incorporated into a new seismic control device, called Tuned Viscous Mass Damper (TVMD) [41]. This device was tested under the excitation from real earthquake signals, and compared with the conventional damper with the same damping value. The results illustrated the performance benefits of the inerter-based TVMD towards the vibration reduction caused by the ground motion. The rack-and-pinion inerter was built and tested in a vehicle suspension system under the quarter-car test rig by Wang et al. [42]. It was shown that the passenger comfort can be improved by the inerter-based suspension when compared with the conventional suspension for the frequency range from 2 to 8 Hz. Another novel TMD device introduced by Brzeski et al. [43] incorporated the rack-and-pinion inerter in combination with a Continuously Variable Transmission (CVT). The prototype of such design was then built and the frequency response curve (FRC) of the TMD employed in the 1-DOF damped structure was tested and compared with the structure without the device [44]. The results evidenced the beneficial damping properties of this inerter-based TMD and the corresponding numerical model was also validated. Further work was carried by Lazarek et al. [45] to identify the parameters of the previously proposed model and study the efficiency of the TMD. The robustness of the model was verified through free and forced vibration tests. The proposed device was shown to be effective for the wide range of vibration suppression conditions.

Furthermore, the nonlinearities of the ball-screw inerter were investigated by Wang and Su [46], including the friction, backlash and elastic effects. With the identified properties, the corresponding nonlinear model of the inerter was also presented and used to analyse the influence of these nonlinearities on the performance of the vehicle suspensions. It was concluded that the ride comfort, dynamic tyre loads and load carrying are negatively affected when compared to the ideal inerter-based suspension, however, still better performance than for the conventional spring-damper suspension was indicated. In the later work by Wang et al. [12], the similar influence was identified against the passenger comfort and the dynamic wheel load of the train suspension system.

2.4.2 Fluid-based inerter

The most common design of the fluid-based inerter is the helical-tube fluid inerter, which was introduced by Swift et al. [4] with the schematic shown in Fig. 2.6. The inertance here is generated by the acceleration of the fluid mass flowing through the external (tube) channel. The initial model of this design was established to consider the various damping effects, compressibility of the fluid as well as the device inertance. Then, the corresponding prototype was built and tested to verify the proposed model under the constant strut velocities and sinusoidal strut displacement with various sets of amplitudes and frequencies. Also, the influence of temperature, fluid types and tube dimensions on the identified values of the leakage damping and the effective stiffness were studied. Apart from the durability and structural simplicity, the ease of integration with the

existing damper constructions is another advantage of the helical-tube fluid inerter. Therefore, several designs, which integrate both fluid inertance and orifice induced damping, were proposed [4]. As shown in Fig. 2.7(a), a flow restriction (using a shim stack or a pressure relief valve) can be added at one end of the helical channel to provide an extra damping in parallel to the inertance. Alternatively, a flow restriction can be realised by a variable orifice or shim stack in the piston, which generates an adjustable damping in series to the inertance, as shown in Fig. 2.7(b). Both designs are useful for vibration suppression applications, as the achievable damping properties have been fundamentally altered and expanded. Several patents presenting the mechanism of those fluid inerter devices have been filed as well [50–52].

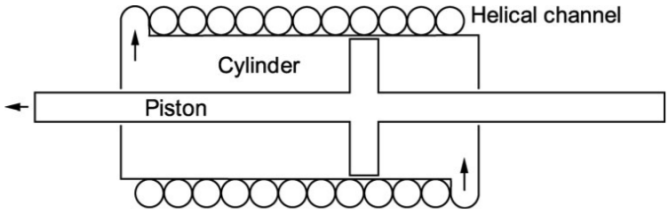

Figure 2.6: The schematic of the helical-tube fluid inerter adopted in [4].

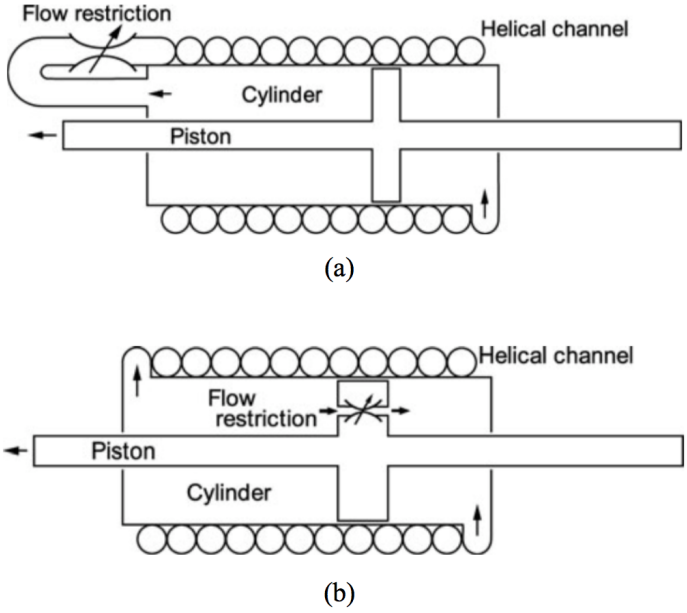

Figure 2.7: The schematic of the alternative designs for the helical-tube fluid inerter with (a) a tube flow restriction and (b) an orifice in the piston (right) adopted in [4].

Subsequently, a similar fluid-based inerter with rectangular spiral bypass pipe was developed and tested by Matsuoka et al. [53] towards the vibration reduction in civil engineering structures. The seismic tests were carried out on a 3-storey structure to confirm the benefits of this device

for reducing the peak accelerations and relative displacements of the structure. The inertance properties of the helical-tube fluid inerter were investigated also in [54] by means of experimental verification of the inertance model for the prototype (shown in Fig. 2.8) with different tube sizes and pitch of the helix. The damping characteristics, and potential improvements for vehicle dynamics were also studied in [5]. A nonlinear model of fluid inerter was taken into a full-car suspension model to investigate the potential improvement on reducing body accelerations by optimisation of the suspension parameters. The influence of the nonlinear damping and friction with regards to the vehicle suspension performance were further analysed by Shen et al. [55]. It was found that no significant detrimental effects were observed except for the worsened performance at low frequencies. More recently, Deastra et al. [56] employed the fluid inerter in the Parallel Viscous Inerter Damper (PVID) to constitute a novel structural vibration suppression system, whilst a customised approach was presented to select the main inerter parameters to provide the expected properties. This approach was then applied to a seismic vibration control case [57], which investigates the benefits of employing the fluid-inerter based TMD on a bases isolation of buildings. Additionally, the research by Titurus [58] developed a full nonlinear dynamic model of the device with fluid-induced damping, stiffness, and inertia effects. This approach identified the links between different types of liquid-based vibration control devices and highlighted the significance of the nonlinear damping and compressibility phenomena in these devices.

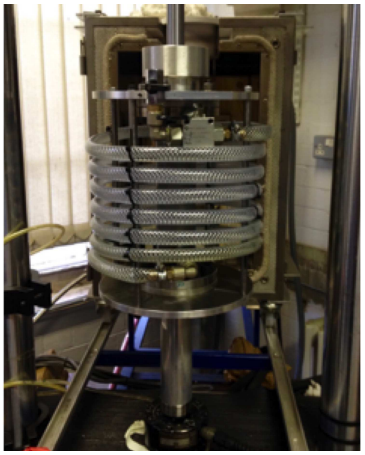

Figure 2.8: The helical inerter prototype built at University of Sheffield [54].

2.4.3 Other realisations

The combined hydraulic-mechanical inerter was introduced in [47] as an alternative design of the inerter. This concept is mainly composed of a hydraulic cylinder and hydraulic motor, with the schematic and prototype shown in Fig. 2.9. The inertance is generated through conversion of the linear motion of the piston rod to the rotational motion of the flywheel which is connected to the

hydraulic motor. To validate the proposed model, the prototype was tested and compared with the simulations. As a conclusion, the hydraulic inerter was deemed to be effective in delivering the designed performance.

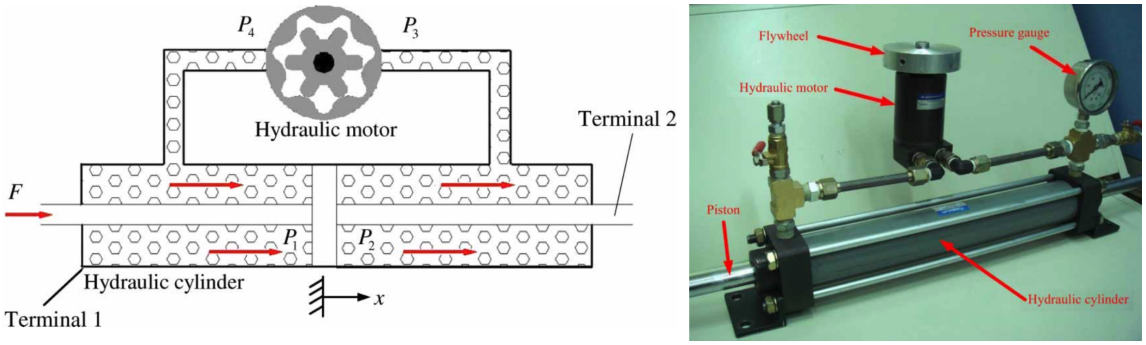

Figure 2.9: The hydraulic inerter schematic (left) and prototype (right) built at the Department of Mechanical Engineering, National Taiwan University [47].

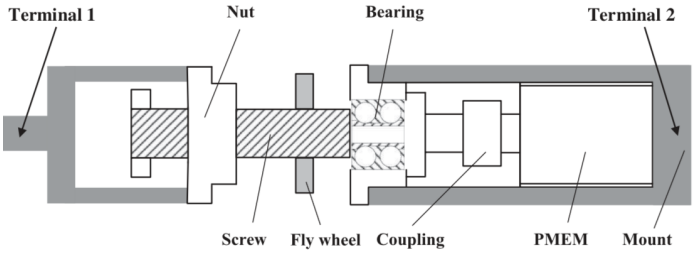

Figure 2.10: The schematic of the mechatronic strut [59].

Another design consisting of a ball-screw inerter and permanent magnet electric machinery (PMEM) was introduced by Wang and Chan [48]. This mechatronic strut combines the mechanical and electrical admittance to achieve the high-order control network. The performance benefits of such device were experimentally verified towards the use in the vehicle suspension [59], full-train system [14] and optical table [60], respectively and compared with their corresponding nonlinear models.

A similar electromagnetic inertial mass damper (EIMD) was built by Nakamura et al. [61]. This design connected the ball-screw to a electric generator. The ability of the EIMD to suppress the structural vibration (e.g. earthquake) was investigated using shaking table tests of the 3-storey and 15-storey shear building models. The results showed the reduction of the story drifts and accelerations by the EIMD when compared with the conventional dampers.

2.5 Summary and Motivation

The literature review in Section 2.2 explains the principle of inerter concept and discusses the novelty of this concept based on the analogy between the mechanical and electrical networks. Then, various applications of the inerter in multiple fields demonstrate the advantages of using inerter for vibration suppression systems in Section 2.3.

Subsequently, the common physical realisations of inerters, their models and tests, are discussed in Section 2.4. The pure mechanical flywheel-based inerter has been specifically discussed along with its variety of mechanism designs, e.g. rack-and-pinion and ball-screw, as well as widely used applications, including the road vehicles, rail vehicles and structures. However, certain disadvantages are noted for the flywheel-based inerters, such as the excessive wear of transmission mechanism, which is the key factor restricting the real applications of the inerter-based vibration absorbers.

The fluid-based inerter was introduced and improved durability and simplicity of the design was highlighted. Additionally, the helical-tube fluid-based design has inherent damping effects, which facilitates easy integration with the conventional dampers. All of these advantages indicate promising development of the fluid-based inerter for the future applications. Currently, there are only limited studies focused on the fluid-based inerter. It can be seen from previous work by Swift et al. [4] that noticeable discrepancies between experimental results and available theoretical models existed, in particular, for the damping effects. On the other hand, similar to all the relevant studies [5, 54–57], the models in [4] were developed for the specific fluid inerter design parameter settings. This means that when one or more of the design parameters change, for example, the tube length, tube diameter or helix diameter, there is limited confidence in the resulting model's accuracy. Consequently, it is generally not practical to use this type of non-generalisable models for shock absorber design.

Therefore, this work aims to establish a modelling methodology for the fluid-based inerters with verified accuracy, while allowing the key design parameters to change within their pre-defined ranges. Such type of model is termed as generalisable models in this work. Furthermore, to take full advantage of the inherent damping, a few designs combining additional orifice induced damping with the fluid-based inerter have been proposed in [4]. However, no detailed modelling study characterising the dynamic properties for these devices was given to date. Therefore, by using the newly established modelling methodology, this work will also establish a generalisable model for a fluid-inerter integrated damping (FID) device design.

CHAPTER 3

NUMERICAL CASE STUDY: TRUCK SUSPENSION DESIGN TO MINIMISE ROAD DAMAGE

3.1 Overview

Before the work on modelling methodology for fluid inerter based vibration suppression, the first piece of my PhD work is a numerical case study of truck suspension design to minimise road damage. This demonstrates the advantage of employing inerter in vehicle suspension applications. It is important since the results of this case study can be considered as a strong evidence to show the promising development of inerter devices. In addition, the results could also facilitate the modelling process of the inerter-based devices by specifying the prospective range of the working frequency and amplitude in applications, as well as the optimum network topology based on spring, damper and inerter with certain parameters.

3.2 Background

Road damage caused by heavy vehicles is a serious problem experienced worldwide. Maintenance of the UK road network during 2017/2018 cost approximately £1.2 billion [62]. Whilst this is partially attributable to ungovernable factors such as bad weather, the vertical tyre force from heavy vehicles has been identified as a significant source of road damage [63]. The static tyre force is determined by the vehicle's weight, but the dynamic tyre force depends *inter alia* on the suspension system and is one of the most critical causes of road damage [64].

The 'dynamic load coefficient' [65] is known as the first criterion used to measure dynamic tyre force. However, the effect of correlation between axles (whereby rear wheels encounter the same road profiles as the front wheels after a speed-dependent delay) on heavy vehicles has

not been taken into account by this measure. To achieve a more realistic evaluation, the 'road stress factor' [66] is defined, based on the fourth power of the dynamic tyre forces in frequency domain. Subsequently, the effect of 'spatial repeatability' [67] has been identified to describe the phenomenon of aggregate peak dynamic tyre forces on certain points along the road surface. The 95^{th} percentile aggregate fourth power force (J_{95}) was proposed to be the corresponding road damage index and has been adopted in many relevant works [68, 69].

The possibility of reducing road damage by adjusting the spring stiffness and damping rate in conventional passive truck suspensions has been investigated by Cole and Cebon [67], as well as Yang et al. [70]. More significant benefits can be obtained from active and semi-active suspensions have also been identified in a series of works [71–73]. For more commonly used suspension performance criteria, such as ride comfort and handling, many studies have been carried out on both passive suspensions [74–80] and (semi-)active suspensions [81–91]. A good summary can be found in the literature [92]. In general, the (semi-)active approach can provide more significant improvements. However, passive suspensions are still attractive in being less expensive and more reliable.

As mentioned in Section 2.3.4, inerters have been shown to be beneficial for ride comfort, handling and dynamic tyre load of road vehicles. The investigation of road damage J_{95} reduction was not yet studied. Comparing to the previous study of truck road damage reduction based on conventional passive suspensions [67], this case study aims to illustrate systematically the potential for road damage reduction offered by inerter-based suspensions. Three simplified truck models are investigated: quarter-car, pitch-plane and roll-plane models. While the correlation between road damage and vehicle speed are considered for both half-vehicle models. Besides, the typical nonlinearities due to leaf springs are further studied. The influence of incorporating leaf spring to the road damage is identified and compared with the results of linear analysis. The design of suspension systems for road vehicles (especially for trucks) is often subject to constraints such as space, weight and cost. Hence in this study, it is chosen to focus on two low-complexity inerter-based suspension layouts, which will be compared with conventional parallel spring-damper layout.

3.3 Performance criterion and candidate suspension layouts

In this section, the J_{95} road damage criterion [67] will be recalled using a quarter-car model as an example. The derivation of J_{95} for the pitch-plane and roll-plane models will be discussed in the next section after each model being explained. This performance index is adopted by the present study. Candidate suspension layouts and the optimisation approach used are then presented.

3.3.1 Road damage index calculation

Consider a typical quarter-car model with conventional parallel spring-damper suspension layout shown in Figure 3.1, where z_r, z_u and z_s represent vertical displacements of road surface, axle (unsprung mass m_u), and vehicle body (sprung mass m_s) respectively. The suspension strut consists of a spring with stiffness k_s and a damper with damping c_s. The tyre is assumed to be a linear spring with stiffness k_t, while the damping effect of the tyre is ignored in this study due to the research focus on suspension.

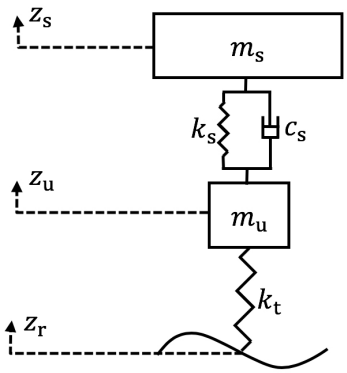

Figure 3.1: A quarter-car model with conventional parallel spring-damper suspension layout.

Based on Newton's second law and taking Laplace transforms, the equations of motion for the sprung and unsprung masses are (s denotes complex number frequency, and $\hat{}$ denotes Laplace transform):

$$m_u \hat{z}_u s^2 = k_t(\hat{z}_r - \hat{z}_u) - c_s(\hat{z}_u - \hat{z}_s)s - k_s(\hat{z}_u - \hat{z}_s) \tag{3.1}$$

$$m_s \hat{z}_s s^2 = c_s(\hat{z}_u - \hat{z}_s)s + k_s(\hat{z}_u - \hat{z}_s) \tag{3.2}$$

The first step in derivation of the road damage index (J_{95}) is the calculation of dynamic tyre force based on specified road inputs. Eq. (3.3) shows a single-sided spectrum (S_{Z_r}) introduced by Kamash and Robson [93] to describe the road surface input (z_r):

$$S_{Z_r}(\omega) = \frac{G_0 \left| \frac{\omega}{2\pi V} \right|^{-2w}}{2\pi V} \tag{3.3}$$

where ω is the angular frequency, V is the vehicle speed, w is the spectrum slope, and G_0 is the road roughness. The value of G_0 is typically between 0.03×10^{-6} to 0.5×10^{-6} $\mathrm{m}^{0.5}\mathrm{s}^{-2}$ for motorways and 0.5×10^{-6} to 30×10^{-6} $\mathrm{m}^{0.5}\mathrm{s}^{-2}$ for minor roads [93]. In this study, G_0 is chosen to be 0.5×10^{-6} $\mathrm{m}^{0.5}\mathrm{s}^{-2}$, while w is 1.25.

Based on the assumption of linear tyre stiffness, the dynamic tyre force is proportional to the tyre deflection, which is calculated by subtracting road displacement from axle displacement. To

obtain axle displacement, Newland [94] derived the direct spectral density of axle displacement (S_{Z_u}) by applying the formula between the input and output spectral density for a linear system:

$$S_{Z_u}(\omega) = H_{Z_rZ_u}(\omega)^* S_{Z_r}(\omega) H_{Z_rZ_u}(\omega)^T \tag{3.4}$$

where * denotes complex conjugate, T denotes matrix non-conjugate transpose, and $H_{Z_rZ_u}(\omega)$ is the transfer function between road input (z_r) and axle output (z_u), which can be derived by combining Eqs. (3.1) and (3.2):

$$H_{Z_rZ_u} = \frac{\hat{z}_u}{\hat{z}_r} = \frac{k_t(k_s + c_s s + m_s s^2)}{m_u m_s s^4 + (m_u + m_s)c_s s^3 + (k_t m_s + (m_u + m_s)k_s)s^2 + c_s k_t s + k_s k_t} \tag{3.5}$$

The cross-spectral densities between road input and axle output are defined as:

$$S_{Z_rZ_u}(\omega) = S_{Z_r}(\omega) H_{Z_rZ_u}(\omega)^T \tag{3.6}$$

$$S_{Z_uZ_r}(\omega) = S_{Z_rZ_u}(\omega)^* \tag{3.7}$$

Then the spectral density of the dynamic tyre force can be derived as:

$$S_F(\omega) = H_{Z_rF,Z_uF}(\omega)^* S_{Z_r,Z_u}(\omega) H_{Z_rF,Z_uF}(\omega)^T \tag{3.8}$$

where $S_{Z_r,Z_u}(\omega)$ is a matrix containing the direct and cross-spectral densities of road input and axle output:

$$S_{Z_r,Z_u}(\omega) = \begin{bmatrix} S_{Z_r}(\omega) & S_{Z_rZ_u}(\omega) \\ S_{Z_uZ_r}(\omega) & S_{Z_u}(\omega) \end{bmatrix} \tag{3.9}$$

and $H_{Z_rF,Z_uF}(\omega)$ is the frequency response transfer function between tyre deflection and dynamic tyre force, which can be expressed as:

$$H_{Z_rF,Z_uF}(\omega) = \begin{bmatrix} k_t & -k_t \end{bmatrix} \tag{3.10}$$

The aggregate fourth power tyre force S_{A^4} is defined as [94]:

$$S_{A^4}(\omega)|_{\omega>0} = 16{F_s}^6 S_F(\omega) \tag{3.11}$$

$$S_{A^4}(\omega)|_{\omega=0} = {F_s}^8 \delta(\omega) \tag{3.12}$$

where F_s is the static tyre force, and $\delta(\omega)$ is Dirac delta function.

Subsequently, the standard deviation of aggregate fourth power tyre force σ_{A^4} is derived to be equal to the square root of the area under the spectral density over the positive frequency range:

$$\sigma_{A^4} = \sqrt{\int_{\omega=0}^{\infty} S_{A^4}(\omega)|_{\omega>0}\, d\omega} \tag{3.13}$$

and the static aggregate fourth power tyre force m_{A^4} is calculated as:

$$m_{A^4} = \sqrt{\int_{\omega=0^-}^{0^+} S_{A^4}(\omega)|_{\omega=0}\, d\omega} = {F_s}^4 \tag{3.14}$$

Following the results by Cole and Cebon [67], the road damage index is defined as the 95^{th} percentile aggregate fourth-power tyre force normalised by the static component, which can be expressed as:

$$J_{95} = \frac{1.65\sigma_{A^4}}{m_{A^4}} + 1 \tag{3.15}$$

In this study, the adopted road damage index J_{95} is calculated for a given speed V, road surface profile (G_0, w), and vehicle model (mass, suspension parameter values).

3.3.2 Candidate suspension layouts

Three low-complexity linear passive suspension layouts S1, S2 and S3 are shown in Figure 3.2(a), (b) and (c), respectively representing a conventional parallel spring-damper layout, a parallel inerter-damper-spring layout and a series inerter-damper in parallel with a spring layout.

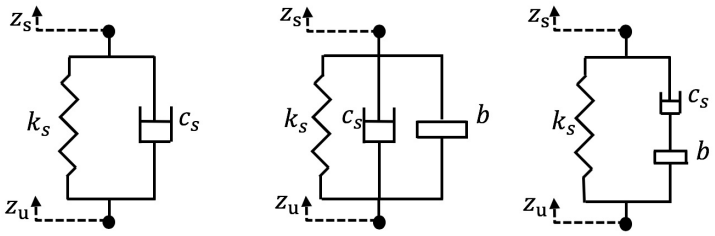

(a) S1 (b) S2 (c) S3

Figure 3.2: Candidate suspension layouts.

The admittance $Y(s)$ of each suspension layout is defined as the strut force (F) divided by the strut relative velocity (v) in the Laplace domain, given by:

- S1: $Y_1(s) = \dfrac{F}{v} = \dfrac{k_s(\hat{z}_u - \hat{z}_s) + c_s s(\hat{z}_u - \hat{z}_s)}{s(\hat{z}_u - \hat{z}_s)} = \dfrac{k_s}{s} + c_s$

- S2: $Y_2(s) = \dfrac{F}{v} = \dfrac{k_s(\hat{z}_u - \hat{z}_s) + c_s s(\hat{z}_u - \hat{z}_s) + bs^2(\hat{z}_u - \hat{z}_s)}{s(\hat{z}_u - \hat{z}_s)} = \dfrac{k_s}{s} + c_s + bs$

- S3: $Y_3(s) = \dfrac{F}{v} = \dfrac{k_s(\hat{z}_u - \hat{z}_s) + \frac{c_s s \times bs^2}{c_s s + bs^2}(\hat{z}_u - \hat{z}_s)}{s(\hat{z}_u - \hat{z}_s)} = \dfrac{k_s}{s} + \dfrac{c_s bs}{bs + c_s}$

As a common nonlinear component in heavy vehicles, it is important to test the influence of leaf springs on road damage performance. One of the most frequently used models of leaf spring was introduced in the book [95], in which an empirical equation was used to characterise the force-deflection relationship:

$$F_i = F_{ENV_i} + (F_{i-1} - F_{ENV_i}) e^{-\frac{|\delta_i - \delta_{i-1}|}{\beta}} \tag{3.16}$$

In Eq. (3.16), for $\delta_i > \delta_{i-1}$,

$$F_{ENV} = k_u \delta + F_u$$

and for $\delta_i < \delta_{i-1}$,

$$F_{ENV} = k_l \delta + F_l$$

where F_i, F_{i-1} and δ_i, δ_{i-1} are the spring force and displacement during the current and previous time steps, F_{ENV_i} is the upper and lower boundary for the envelope of the measured force-deflection curves, β is a spring parameter describing the rate of hysteresis as the force approaches the boundary of the envelope and differs for ascending and descending deflections, k_u is upper envelope stiffness, k_l is lower envelope stiffness, F_u is upper envelope friction, and F_l is lower envelope friction.

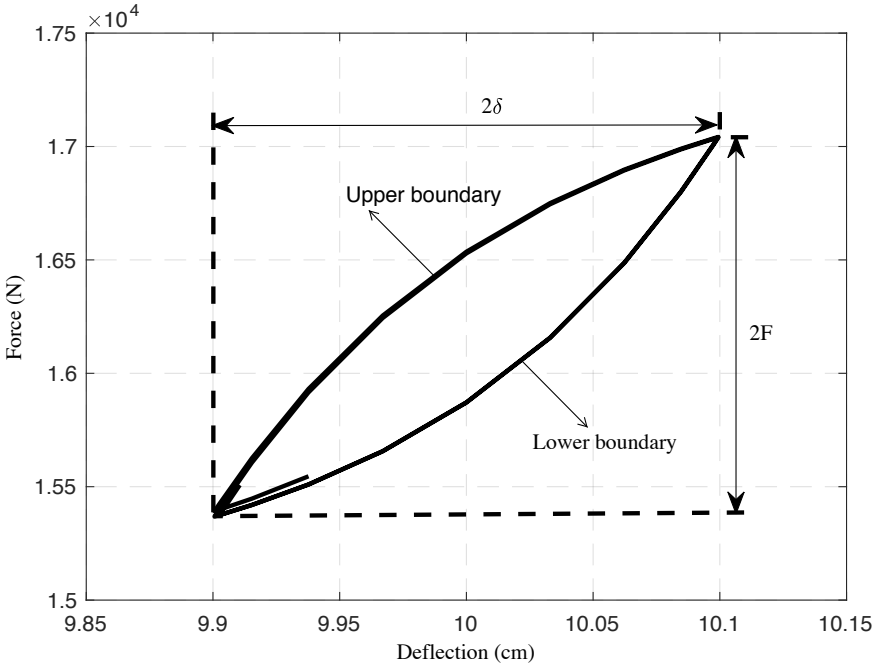

Figure 3.3: Typical force-deflection characteristics of a leaf spring.

Figure 3.3 illustrates the force-deflection characteristics of a typical leaf spring [95]. It is clear that the spring rate changes continuously during compression and extension.

3.3.3 Optimisation approach

For each vehicle model, across a wide range of stiffness values, Matlab was used to calculate the standard deviation of aggregate fourth power tyre force. For linear models this was carried out in the frequency domain as per Eq. (3.13), across a frequency range from 0.2 Hz to 30 Hz with step of 0.2 Hz and assuming a vehicle speed of 22 m/s (80 km/h), similar to the approach used by Cole and Cebon [67]. Non-linear leaf spring models were necessarily studied in the time domain, for which a time interval of 20 seconds with sample time 0.01 seconds was used. In both domains, Matlab's *fminsearch* algorithm was used to calculate the damper (c_s) and inerter (b) values which minimised the road damage value J_{95}. It is also noted that the stiffness of a monoleaf steel spring is typically 2 MN/m to support the self-weight of the truck within a reasonable suspension deflection, while the stiffness of a typical air spring is around 0.4 MN/m and can be adjustable.

3.4 Optimisation results for linear suspension layouts

3.4.1 Optimisation results for a quarter-car model

A quarter-car model with 2 degrees-of-freedom (DoF) is shown in Figure 3.4, which is used to describe the bounce motion of a heavy truck [67]. The model has sprung mass m_s of 4500 kg, unsprung mass m_u of 500 kg, and tyre stiffness k_t of 2 MN/m. Its suspension with admittance $Y(s)$ can be selected from the three candidate layouts introduced in the previous section.

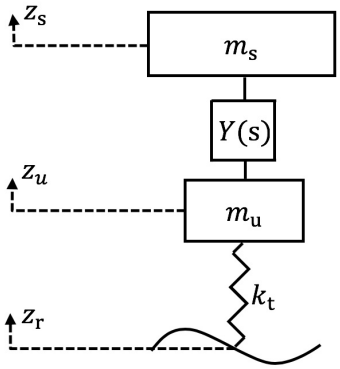

Figure 3.4: A heavy truck quarter-car model.

Based on Newton's second law and taking Laplace transforms, the equations of motion for the sprung and unsprung masses are:

$$m_u \hat{z}_u s^2 = k_t(\hat{z}_r - \hat{z}_u) - Y(s)(\hat{z}_u - \hat{z}_s)s \tag{3.17}$$

$$m_s \hat{z}_s s^2 = Y(s)(\hat{z}_u - \hat{z}_s)s \tag{3.18}$$

The transfer function $H_{Z_r Z_u}$ from $\hat{z}_r$ to $\hat{z}_u$ can be derived by combining Eqs. (3.17) and (3.18):

$$H_{Z_r Z_u} = \frac{\hat{z}_u}{\hat{z}_r} = \frac{k_t\left(Y(s)s + m_s s^2\right)}{m_u m_s s^4 + (m_u + m_s)Y(s)s^3 + k_t m_s s^2 + Y(s)k_t s} \tag{3.19}$$

The corresponding road damage is calculated based on Eq. (3.15). The optimisation results for this quarter-car model are plotted in Figure 3.5 across a wide range of stiffness for the three candidate suspension layouts. Figure 3.5(a) shows the optimised J_{95} values, while Figure 3.5(b) displays the percentage improvements of S2 and S3 compared with S1, respectively. The improvement of J_{95} increases with stiffness for both S2 and S3. In the latter case the road damage is reduced by about 12% for a stiffness of 2 MN/m, which represents the stiffness of typical leaf springs for a heavy vehicle. Figures 3.5(c) and 3.5(d) present the corresponding optimum damper and inerter values respectively. At very low stiffness values, inerters are found to be incapable of reducing road damage, hence optimal inerter values are then infinity for S3 and zero for S2, yielding similar road damage to the S1 case. It is also notable that the parallel S2 layout requires

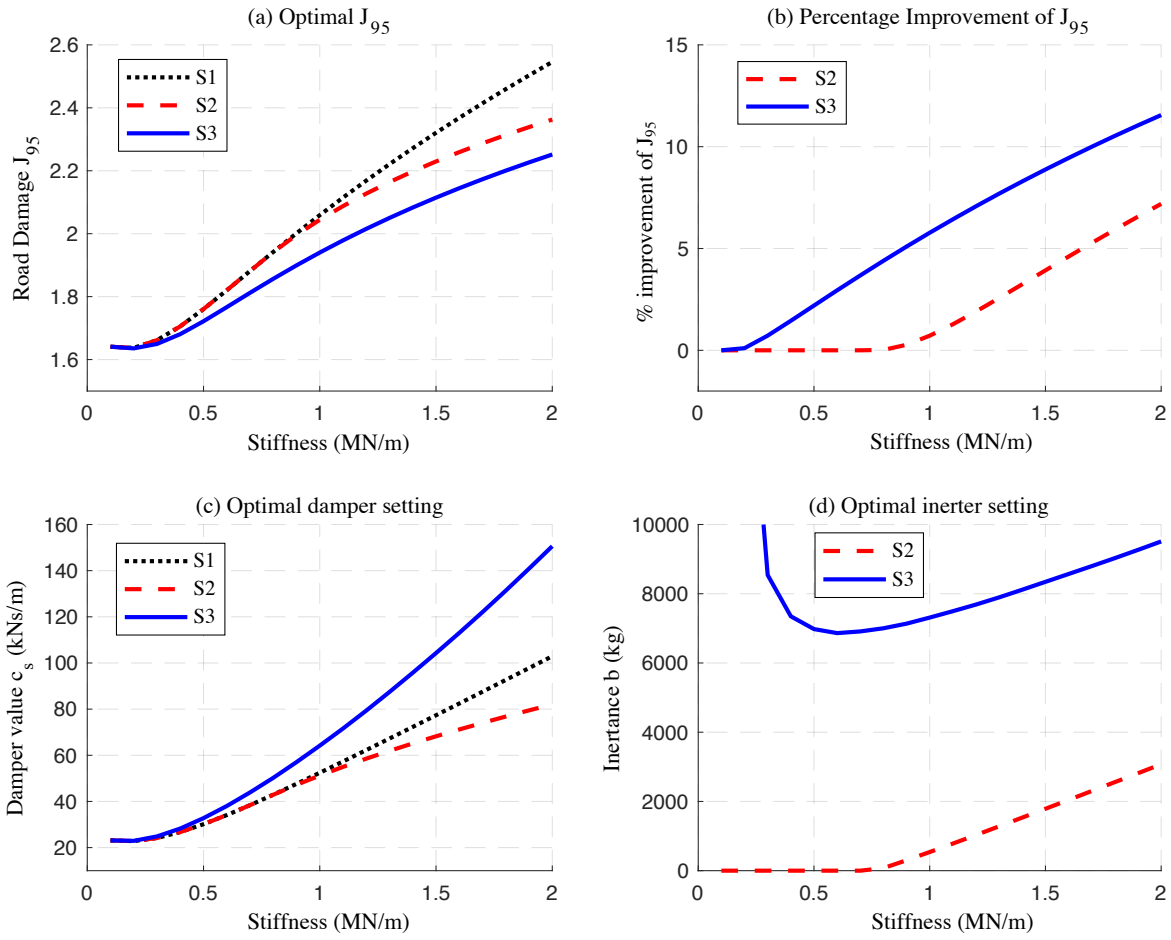

Figure 3.5: (a) The optimum road damage J_{95}, together with (b) corresponding percentile improvements, (c) optimum damper values, and (d) optimum inertance values of candidate suspension layouts for a quarter-car model.

less damping and lower inertance than the series S3 layout, which is to be expected because the displacements (and hence velocities and accelerations) across the terminals of the damper and inerter will generally be greater in the parallel case. Figures 3.5(a) and 3.5(b) show that S3 has better performance than S2 over the whole range of stiffness. But for a given loading or stiffness value, S3 needs much higher inertance, which may have practical or financial implications. It is worth pointing out that in the work by Smith and Wang [31], the r.m.s dynamic tyre load, which represents the tyre grip performance, was studied for S1-S3. Due to the close link between these two performance indices, similar trends of the optimisation results for both performance indices are expected.

3.4.2 Pitch-plane model analysis

A pitch-plane model with 4 DoF is shown in Figure 3.6 to describe both the pitch and vertical motions of a heavy truck. The parameters of this model are specified based on the same heavy truck in the previous subsection, including half-truck sprung mass $m_s = 9000\,\text{kg}$, front/rear unsprung masses $m_{u1} = m_{u2} = 500\,\text{kg}$, and front/rear tyre stiffness $k_{t1} = k_{t2} = 2\,\text{MN/m}$ (as in the work [67]). The distances between the centre of gravity of the sprung mass to both suspensions are defined to be identical: $a = 4\,\text{m}$, and the sprung mass is assumed to be uniformly distributed over its length, with ratio $r = 0.58$, such that its moment of inertia $I_s = m_s a b r^2$. The admittances of the front and rear suspensions are assumed to be the same: $Y_1(s) = Y_2(s)$, the front and rear static tyre forces F_{s1} and F_{s2} are also equal.

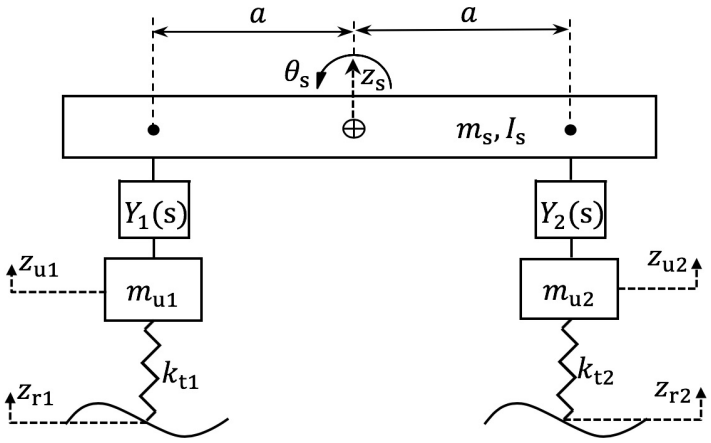

Figure 3.6: A heavy truck pitch-plane model.

Four equations of motion can be constructed as below, corresponding to pitch and vertical motions of the masses:

$$m_{u1}\hat{z}_{u1}s^2 = k_{t1}(\hat{z}_{r1} - \hat{z}_{u1}) - Y_1(s)(\hat{z}_{u1} - \hat{z}_s + a\hat{\theta}_s)s \tag{3.20}$$

$$m_{u2}\hat{z}_{u2}s^2 = k_{t2}(\hat{z}_{r2} - \hat{z}_{u2}) - Y_2(s)(\hat{z}_{u2} - \hat{z}_s - a\hat{\theta}_s)s \tag{3.21}$$

$$m_s\hat{z}_s s^2 = Y_1(s)(\hat{z}_{u1} - \hat{z}_s + a\hat{\theta}_s)s + Y_2(s)(\hat{z}_{u2} - \hat{z}_s - a\hat{\theta}_s)s \tag{3.22}$$

$$I_s\hat{\theta}_s s^2 = -aY_1(s)(\hat{z}_{u1} - \hat{z}_s + a\hat{\theta}_s)s + aY_2(s)(\hat{z}_{u2} - \hat{z}_s - a\hat{\theta}_s)s \tag{3.23}$$

In this pitch-plane model, the road inputs z_{r1} and z_{r2} represent the vertical road disturbances of the front wheel and the rear wheel, respectively. The axle outputs z_{u1} and z_{u2} denote the vertical displacements of the unsprung mass at the front and rear axles respectively. The vehicle body outputs θ_s and z_s represent the rotational and vertical displacements of the sprung mass.

To derive the value of road damage index J_{95} for this pitch-plane model, the direct spectral densities of axle displacements (S_{Z_u}) needs to be extended as there are now two road inputs and two axle outputs [94]:

$$S_{Z_u}(\omega) = H_{Z_r Z_u}(\omega)^* \left[S_{Z_r}(\omega) P(\omega)\right] H_{Z_r Z_u}(\omega)^T \tag{3.24}$$

where $H_{Z_r Z_u}(\omega)$ here is a matrix of frequency response functions, including four transfer functions between road inputs (z_{r1} and z_{r2}) and axle outputs (z_{u1} and z_{u2}) based on Eqs. (3.20) to (3.23). Matrix $P(\omega)$ represents the relations between each of the road displacement inputs, which are identical, but with a time delay between them. The matrix $P(\omega)$ is specified based on this time delay:

$$P(\omega) \doteq P_{pitch}(\omega) = \begin{bmatrix} 1 & e^{-i\omega T_{12}} \\ e^{i\omega T_{12}} & 1 \end{bmatrix} \tag{3.25}$$

where T_{12} represents the time delay between road inputs to the front and the rear axle that can be derived from the vehicle speed and the wheelbase ($2a$) of the vehicle:

$$T_{12} = \frac{2a}{V} \tag{3.26}$$

Then the matrix $S_{Z_r,Z_u}(\omega)$ in Eq. (3.8) needs to be updated to include all the terms for direct and cross-spectral densities of two road inputs and two axle outputs:

$$S_{Z_r,Z_u}(\omega) = \begin{bmatrix} S_{Z_{r1}Z_{r1}}(\omega) & S_{Z_{r1}Z_{u1}}(\omega) & S_{Z_{r1}Z_{r2}}(\omega) & S_{Z_{r1}Z_{u2}}(\omega) \\ S_{Z_{u1}Z_{r1}}(\omega) & S_{Z_{u1}Z_{u1}}(\omega) & S_{Z_{u1}Z_{r2}}(\omega) & S_{Z_{u1}Z_{u2}}(\omega) \\ S_{Z_{r2}Z_{r1}}(\omega) & S_{Z_{r2}Z_{u1}}(\omega) & S_{Z_{r2}Z_{r2}}(\omega) & S_{Z_{r2}Z_{u2}}(\omega) \\ S_{Z_{u2}Z_{r1}}(\omega) & S_{Z_{u2}Z_{u1}}(\omega) & S_{Z_{u2}Z_{r2}}(\omega) & S_{Z_{u2}Z_{u2}}(\omega) \end{bmatrix} \tag{3.27}$$

and the frequency response transfer functions ($H_{Z_rF,Z_uF}(\omega)$ in Eq. (3.8)) between tyre deflections and dynamic tyre forces are extended to:

$$H_{Z_rF,Z_uF}(\omega) = \begin{bmatrix} k_{t1} & -k_{t1} & 0 & 0 \\ 0 & 0 & k_{t2} & -k_{t2} \end{bmatrix} \tag{3.28}$$

The aggregate fourth power tyre force S_{A^4} is defined for two correlated tyre forces [94]:

$$S_{A^4}(\omega)|_{\omega>0} = \sum 16\mathbf{F_{s12}} \otimes P_{pitch}(\omega)^* S_F(\omega) \tag{3.29}$$

$$S_{A^4}(\omega)|_{\omega=0} = \left(\sum_{j=1}^{2} {F_{sj}}^4\right)^2 \delta(\omega) \tag{3.30}$$

where $\sum$ indicates the sum of all the elements of the matrix, $\otimes$ indicates element by element multiplication, F_{sj} is static tyre force on the jth tyre, and $\mathbf{F_{s12}}$ is a matrix that includes all the static tyre forces:

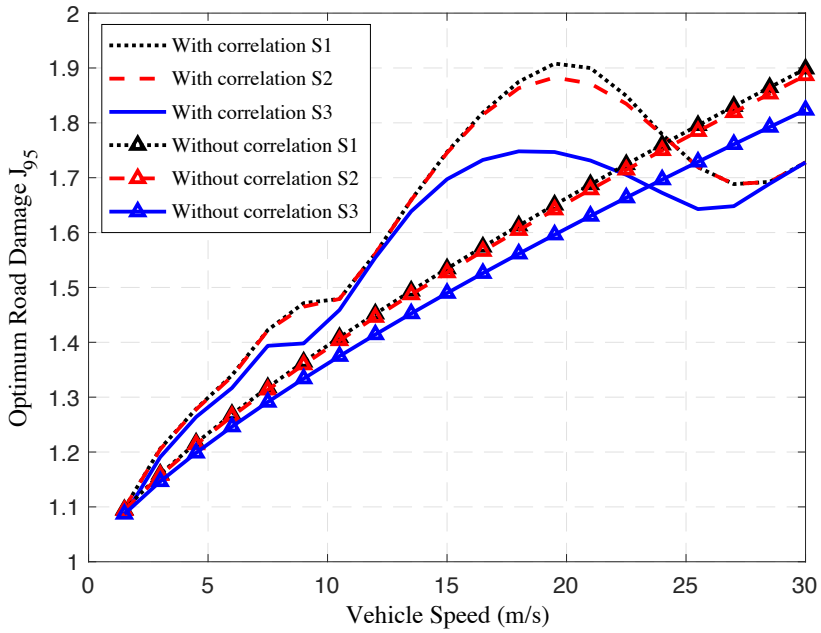

Figure 3.7: The road damage with optimum b versus vehicle speed for both inputs and outputs correlated or uncorrelated.

$$\mathbf{F_{s12}} = \begin{bmatrix} {F_{s1}}^3 & {F_{s2}}^3 \end{bmatrix} \tag{3.31}$$

Having modified the above expressions, the road damage index J_{95} is again calculated through Eq. (3.15) for the pitch-plane model. According to Eqs. (3.25) and (3.26), there will be a correlation between vehicle speed and road damage. With fixed suspension stiffness $k_{s1} = k_{s2} = 0.4$ MN/m and fixed suspension damping $c_{s1} = c_{s2} = 10$ kNs/m, the minimum road damage that can be achieved by only optimising inertance b for suspension layouts S2 and S3 are plotted in Figure 3.7 versus vehicle speed, compared with the road damage caused by conventional layout S1. The plots of road damage with correlated inputs and outputs display peaks at some speeds across the ascending curve of road damage, while the value for the case without correlation (when $P(\omega)$ is an identity matrix) grows monotonically with speed. Such differences demonstrate the effect of the interaction between the vehicle's front and rear axles on road damage, which can be explained by a wheelbase filtering effect related with the model's natural frequencies. For example, there is a pitch mode at 2.35 Hz, which equates to 18.8 m/s for a wheelbase of 8.0 m, at which speed the ratios of correlated to uncorrelated road damage are approximately local maxima for each of S1-S3. Hence, as a simple design approach for heavy vehicle manufacturers, placing the front and rear wheels in different wheel paths may effectively reduce the road damage. Meanwhile, the optimum road damage for suspension layout S3 illustrates that the achievable reduction of road damage by inerter-based suspensions varies with speed.

For brevity, the optimisation results for the pitch-plane model will be discussed together with roll-plane model in the next subsection for all three candidate suspension layouts.

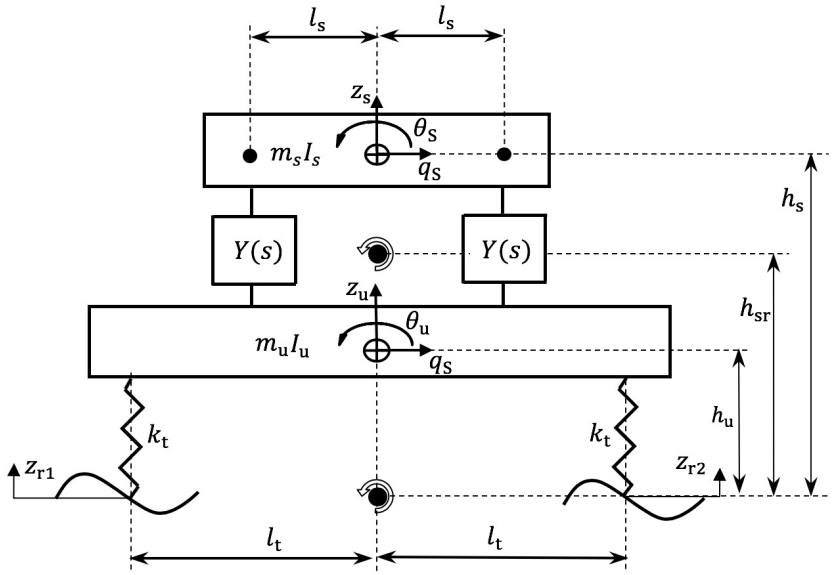

Figure 3.8: A heavy truck 4-DoF roll-plane model.

3.4.3 Roll-plane model analysis

For the roll-plane case, due to the more serious road damage caused by rigid axle structures [67], it is more persuasive to choose this axle type for investigation. In order to calculate the dynamic tyre force for road damage assessment, a 4-DoF roll-plane model of a heavy truck is depicted in Figure 3.8. The parameters of the model are selected based on a single axle of a typical heavy truck, therefore the model is symmetrical and all the parameters are identical for both sides. Similar assumptions are adopted to those in the study by Cole and Cebon [67]: pitch-plane correlation between axles and load transfer within the axles are neglected during the analysis for simplicity. The parameters of this roll-plane model are specified from the same heavy truck in the previous subsections with a typical rigid axle suspension, including half-truck sprung mass $m_s = 9000\,\text{kg}$, single axle unsprung mass $m_u = 1000\,\text{kg}$, distances between tyres and unsprung mass roll centre $l_t = 0.925\,\text{m}$, distances between suspensions and sprung mass roll centre $l_s = 0.5 l_t = 0.4625\,\text{m}$, height of sprung mass roll centre $h_s = 2\,\text{m}$, height of sprung mass centre of gravity $h_{sr} = 0.6\,\text{m}$, and tyre stiffness $k_t = 2\,\text{MN/m}$. In addition, we assume that the unsprung mass roll centre is at ground level, hence the height of unsprung mass centre of gravity $h_u = 0.5\,\text{m}$.

The vertical and angular equations of motion for both the sprung and unsprung masses are shown below:

$$m_s\hat{z}_s s^2 = Y(s)(\hat{z}_u - \hat{z}_s - l_s\hat{\theta}_s - l_s\hat{\theta}_u)s + Y(s)(\hat{z}_u - \hat{z}_s + l_s\hat{\theta}_s + l_s\hat{\theta}_u)s \tag{3.32}$$

$$\begin{aligned} m_u\hat{z}_u s^2 = \; & -Y(s)(\hat{z}_u - \hat{z}_s - l_s\hat{\theta}_s - l_s\hat{\theta}_u)s - Y(s)(\hat{z}_u - \hat{z}_s + l_s\hat{\theta}_s + l_s\hat{\theta}_u)s \\ & + k_t(\hat{z}_{r1} - \hat{z}_u + l_t\hat{\theta}_u) + k_t(\hat{z}_{r2} - \hat{z}_u - l_t\hat{\theta}_u) \end{aligned} \tag{3.33}$$

$$I_s\hat{\theta}_s s^2 = -l_s Y(s)(\hat{z}_u - \hat{z}_s - l_s\hat{\theta}_s - l_s\hat{\theta}_u)s + l_s Y(s)(\hat{z}_u - \hat{z}_s + l_s\hat{\theta}_s + l_s\hat{\theta}_u)s \tag{3.34}$$

$$\begin{aligned} I_u\hat{\theta}_u s^2 = \; & l_s Y(s)(\hat{z}_u - \hat{z}_s - l_s\hat{\theta}_s - l_s\hat{\theta}_u)s - l_s Y(s)(\hat{z}_u - \hat{z}_s + l_s\hat{\theta}_s + l_s\hat{\theta}_u)s \\ & - l_t k_t(\hat{z}_{r1} - \hat{z}_u + l_t\hat{\theta}_u) + l_t k_t(\hat{z}_{r2} - \hat{z}_u - l_t\hat{\theta}_u) \end{aligned} \tag{3.35}$$

where θ_s is sprung mass roll angle, z_s is sprung mass vertical displacement, θ_u is unsprung mass roll angle and z_u is unsprung mass vertical displacement. For consistency with the variables specified in the derivation of road damage index J_{95}, the corresponding z_{u1} and z_{u2} are expressed by combining l_t with θ_u and z_u (assuming $\sin(\theta_u) \approx \theta_u$ when θ_u is small):

$$z_{u1} = z_u - \theta_u l_t \tag{3.36}$$

$$z_{u2} = z_u + \theta_u l_t \tag{3.37}$$

Also the moments of inertia (I_s and I_u) for the sprung and unsprung masses are assumed to be:

$$I_s = m_s {l_s}^2 + m_s(h_s - h_{sr})^2 \tag{3.38}$$

$$I_u = m_s {l_t}^2 + m_s {h_u}^2 \tag{3.39}$$

The vehicle's left and right wheels are subject to road excitations on a homogeneous and isotropic random surface. Therefore, the matrix $P(\omega)$ in Eq. (3.24) representing the relationship between each of the road displacement inputs is:

$$P(\omega) \doteq P_{roll}(\omega) = \begin{bmatrix} 1 & g_n \\ g_n & 1 \end{bmatrix} \tag{3.40}$$

where the coherence function g_n between each height of the parallel profiles can be represented as [96]:

$$g_n = \left\{ \frac{2|\pi l_t n|^w}{\Gamma(w)} \right\} K_w(2\pi l_t n) \tag{3.41}$$

where n is wave number, $\Gamma(.)$ denotes the gamma function, and $K_w(.)$ denotes the modified Bessel function of order w. Additionally, due to the lack of correlation between the two road inputs, the aggregate fourth power force S_{A^4} reduces to:

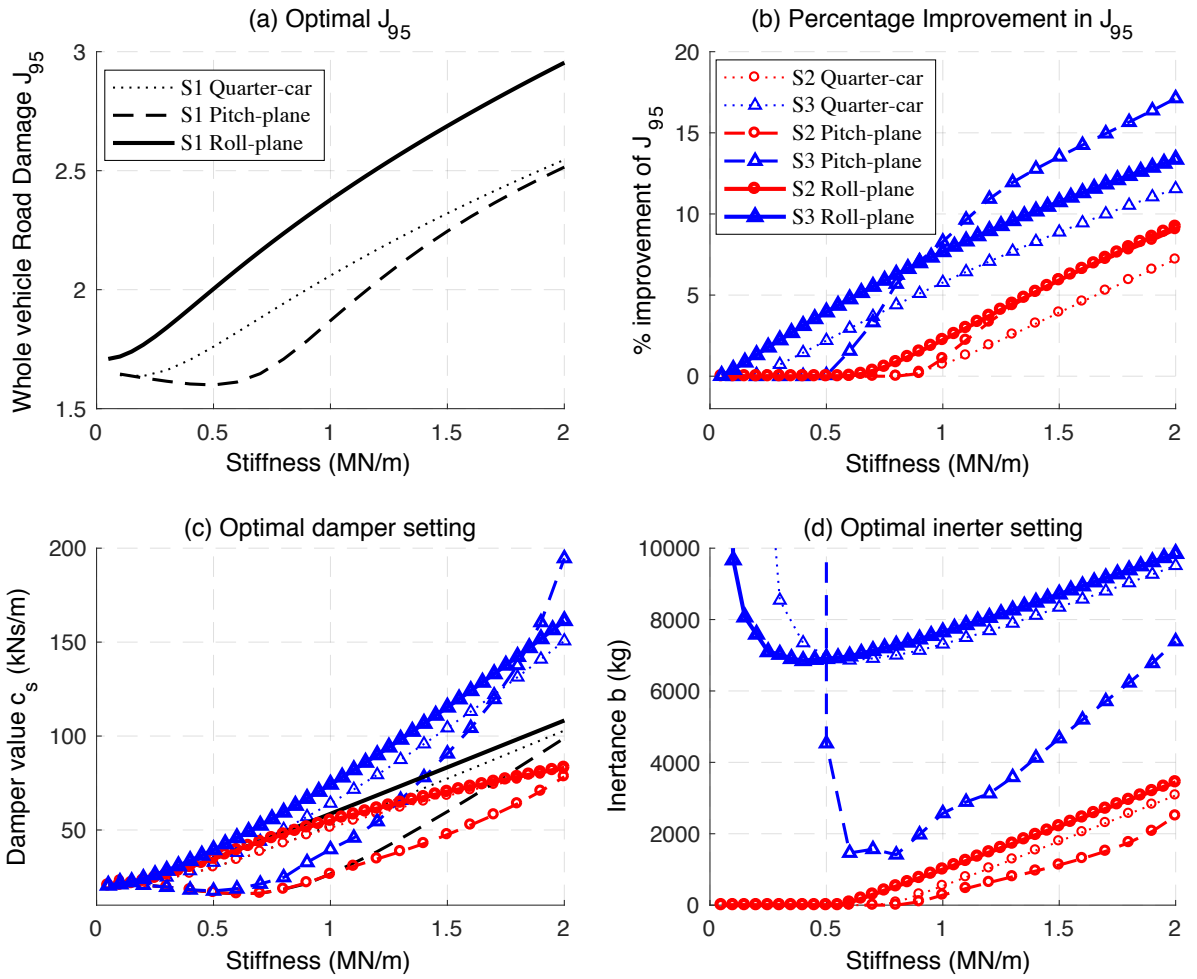

Figure 3.9: (a) Optimum road damage J_{95} of suspension layout S1 for each model. (b) comparison of percentile improvements against S1 in optimum road damage, (c) corresponding optimum damping (c) and (d) inertance values (b) of candidate suspension layouts for the quarter-car, pitch-plane and roll-plane models.

$$S_{A^4}(\omega)|_{\omega>0} = \sum 16{F_s}^6 \otimes S_F(\omega) \tag{3.42}$$

Optimisations were carried out to achieve minimum road damage following the procedure in the section of 'Optimisation approach'. For the quarter-car, pitch-plane and roll-plane models, the optimum values of road damage index J_{95} for layout S1 are demonstrated in Figure 3.9(a). The general trends of the results for both pitch-plane and roll-plane models are similar to those for the quarter-car model discussed before. However, for the pitch-plane model the road damage is reduced, which must be attributable to the effect of correlation between front and rear axles. The percentile improvements of J_{95} for layouts S2 and S3 in comparison with S1 for each vehicle model are plotted in Figure 3.9(b). It is clear that the improvements are further enhanced in

half-vehicle models, except for soft suspensions with stiffness approximately less than 0.7 MN/s for the S3 layout in the pitch-plane model. For roll-plane model, both S2 and S3 layouts can reduce road damage across a wider range of stiffness than for pitch-plane and quarter-car models. Meanwhile, greater road damage reduction is achieved by the S3 layout across the majority of the stiffness range for all three models. The corresponding values of damping and inertance for optimum J_{95} are shown in Figure 3.9(c) and 3.9(d), respectively. Figure 3.9(d) shows that generally lower inertance values are optimal for pitch-plane than for quarter-car models. The nearly infinite value of inertance for low stiffness values reveals approximately a rigid rod. Therefore S3 works similarly to S1 below stiffness of 0.5 MN/s for the pitch-plane model. In addition, in contrast to the pitch-plane model with S2 and S3 layouts, the required damping and inertance for roll-plane models are larger compared to S1 layout. The reason could be the superimposed dynamic tyre force from the interactive road inputs across the rigid axle.

3.5 Optimisation results of models with leaf spring nonlinearities

The previous investigations were carried out in the frequency domain. In order to assess the effect of nonlinear leaf springs, time domain Simulink models for the pitch-plane and the roll-plane were developed.

In the time domain, the road profile needs to be time dependent. Based on Eq. (3.3), a white noise profile is filtered by a low pass filter with transfer function (G),

$$G(s) = \frac{2\pi\sqrt{G_0 V}}{s + \omega_0} \tag{3.43}$$

where $\omega_0 = 2\pi f_0$. The filtered profile is used to simulate the road's vertical input z_0 [97],

$$\dot{z}_0(t) = -2\pi f_0 z_0(t) + 2\pi\sqrt{G_0 V}\, w(t) \tag{3.44}$$

where f_0 denotes lower boundary of frequency ($f_0 = 0.2$ Hz is chosen in this study), V is the vehicle speed ($V = 22$ m/s similar to Section 3.4), and $w(t)$ represents a random time-dependent white noise.

Using Eq. (3.16), a Simulink model was built with the deflection of the suspension as its input and the force produced by a leaf spring as its output. The random road inputs give rise to variable amplitudes of spring deflection for each cycle, but all the parameters in Eq. (3.16) are sensitive to the amplitude of deflection and the preload. The road damage was optimised for three different sets of leaf spring parameters (shown in Table 3.1) corresponding to soft, medium and relatively stiff leaf springs respectively, based on the parameters in the relevant literatures [95, 98, 99]. The optimised results for S1, S2 and S3 for each of these three leaf springs are listed in Table 3.2.

It is also worth mentioning that the fixed time step is used when run the simulation due to the values of β are chosen as constant.

Table 3.1: Three sets of parameter values for typical soft, medium and stiff leaf springs.

Parameters	**Leaf spring 1** (soft)	**Leaf spring 2** (medium)	**Leaf spring 3** (stiff)
k_u (MN/m)	0.58	1.35	2.06
k_l (MN/m)	0.47	1.14	1.77
F_u (kN)	15.8	36.5	55.4
F_l (kN)	11.5	29.0	46.0
β (mm)	2.03	1.03	0.1

Table 3.2: Optimum road damage, together with corresponding damper and inerter values for the pitch-plane and the roll-plane models based on three sets of leaf spring parameters (% improvement are given in bracket compared with S1).

Leaf spring	**Layout**	**Pitch-plane Model**			**Roll-plane Model**		
		Road Damage J_{95}	Damping c_s (kNs/m)	Inertance b (kg)	Road Damage J_{95}	Damping c_s (kNs/m)	Inertance b (kg)
1	S1	1.66	28.5	N/A	1.71	41.4	N/A
	S2	1.66 (0%)	28.5	0	1.71 (0%)	41.4	0
	S3	1.66 (0%)	27.7	16622	1.71 (0%)	40.7	52000
2	S1	1.93	41.2	N/A	1.83	44.2	N/A
	S2	1.93 (0%)	41.2	0	1.83 (0%)	44.1	0
	S3	1.78 (7.7%)	45.8	3888	1.80 (2%)	51.1	10705
3	S1	2.54	79.3	N/A	2.30	80.8	N/A
	S2	2.10 (17.3%)	46.7	1303	2.08 (9.6%)	41.0	3437
	S3	2.05 (19.3%)	111.3	5354	2.02 (12.2%)	101.1	8248

The general trends of road damage are similar to those from the frequency-domain analysis for pitch-plane and roll-plane models with linear springs: at low values of stiffness (leaf spring 1), layouts S2 and S3 do not provide any benefit over S1, but at intermediate and high stiffness (leaf springs 2 and 3), layout S3 in particular reduces road damage by up to 19.3% for the pitch-plane model and 12.2% for the roll-plane model. It is also worth mentioning that smaller damping is required for a given reduction in road damage since the damping effect of leaf springs contributes to the total damping force. There are some other uncertainties that may affect the results, such as the amplitude sensitivity of the leaf spring parameters, which means the current optimised suspension parameters will vary when the amplitude of road input changes. Furthermore, one example is shown in Fig. 3.10 to show the effect of nonlinear leaf spring 2 to the dynamic tyre force for the pitch-plane model, compared with a linear spring with the stiffness assumed to be mean value of the leaf spring 2 as 1.25 MN/m. The red and blue curves represent the dynamic tyre force produced with leaf spring and linear spring, respectively. As the curves are largely

overlapped for both the suspension layout S1 and S3, there is no apparent influence caused by the nonlinearities of leaf spring with regards to the aggregated dynamic tyre forces.

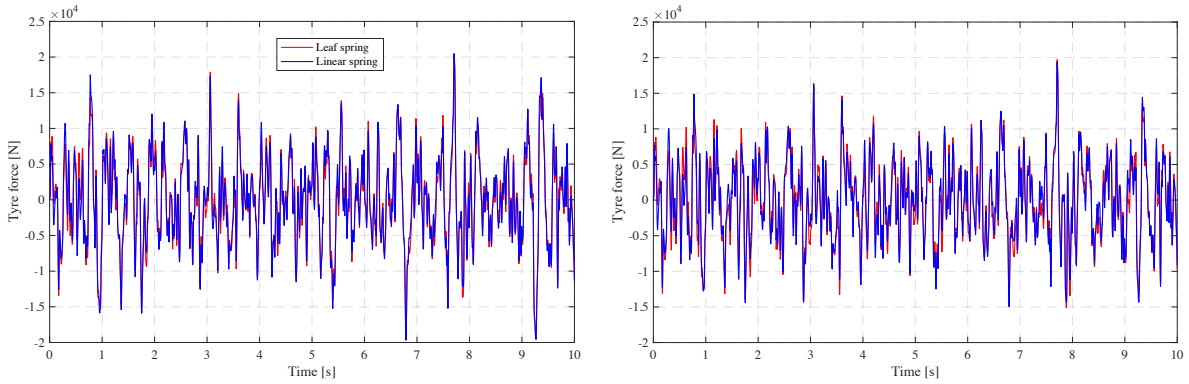

(a) S1 (b) S3

Figure 3.10: Pitch-plane dynamic tyre forces with leaf spring and linear spring for suspension layouts (a) S1 and (b) S3.

In terms of the investigation of the leaf spring in both pitch-plane and roll-plane models, the road damage improvements are not strongly affected by this nonlinear factor, especially the benefit obtained for the pitch-plane model, which is even bigger than the linear model for very stiff suspension.

3.6 Summary

This study demonstrates that road damage can be significantly reduced by incorporating inerters into the suspension systems of heavy trucks. Matlab's *fminsearch* algorithm was used to determine the values of suspension elements (i.e. spring, damper and inerter), which minimise the J_{95} road damage index. The reduction in road damage increases with the stiffness of the suspension system. For the quarter-car model, with stiff suspension systems (as used by heavy trucks), the inerter-damper series configuration (S3) and inerter-damper parallel configuration (S2) are predicted to deliver more than 11% and 7% improvement respectively. For pitch-plane models these values can reach 17% and 9%, and for the roll-plane models 13% and 9% are achievable. Similar levels of improvement have also been shown to arise when the leaf-spring nonlinearities are incorporated into inerter-based suspensions. Therefore, it has been shown that there are promising benefits for reduction in road damage by incorporating the inerter element into truck suspension systems.

In summary, this case study provide confidence for the development of the inerter-based vibration suppression devices, based on the verified benefits obtained by employing the inerter. Furthermore, as the results show, the inerter-damper series configuration (S3) always provides better improvement, compared with the parallel configuration (S2), which exactly inspires and

motivates the idea of a FID device with series connected valve damping, which will be discussed in later chapters.

CHAPTER 4

NETWORK REPRESENTATIONS OF FLUID-BASED INERTER AND FLUID-INERTER INTEGRATED DAMPING DEVICE

4.1 Overview

This chapter first modifies an analogy between the mechanical and hydraulic networks. This is useful to the modelling of fluid-based vibration suppression devices, such as the conventional hydraulic damper and the fluid-based inerter. Then the working principle of fluid-based inerters is explained. Analysis of the possible flow paths in the fluid-based inerter is used to form the hydraulic network of the device. By applying the network synthesis method [100], an equivalent mechanical network can be obtained. Following the same procedure, the linear lumped parameter models of the fluid-inerter integrated damping (FID) device are also derived.

4.2 Analogy between mechanical and hydraulic networks

For modelling of the fluid-based devices, it is important to have the analogy between the mechanical and hydraulic networks, which could be helpful to facilitate the better understanding of the dynamic behaviour of the devices. With the mass element being replaced by the newly introduced inerter, the analogy between the mechanical and electrical networks has been completed [2]. It is inspired by this modification that the existing analogy between the mechanical and hydraulic networks could be similarly updated.

4.2.1 Hydraulic network analysis

Consider a through-rod cylinder that consists of two chambers and a symmetric piston, both chambers are fully filled of homogeneously distributed compressible fluid, and they are connected

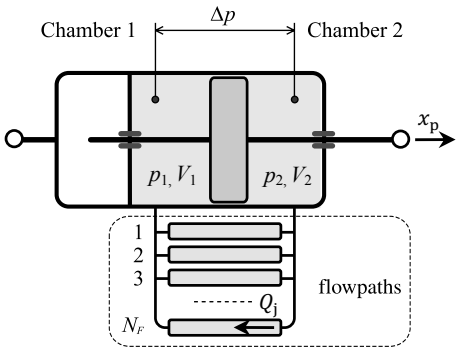

Figure 4.1: A cylinder with piston and two chambers filled of fluid, and connected by various flow paths [101].

by various flow paths, as shown in Fig. 4.1. The bulk modulus (B) of the fluid is assumed to be constant and defined by [102],

$$B = V_1 \frac{\delta p_1}{\delta V_1} = -V_2 \frac{\delta p_2}{\delta V_2}, \tag{4.1}$$

where V_1 and V_2 are the volume of the fluid in each chamber, δV_1 and δV_2 are the corresponding changes of fluid volume, δp_1 and δp_2 are the corresponding pressure changes, which can be converted to the form:

$$\dot{p}_1 = \frac{B}{V_1}\dot{V}, \quad \dot{p}_2 = -\frac{B}{V_2}\dot{V}, \tag{4.2}$$

where $\dot{V}$ denotes the total volumetric flow rate between the cylinder chambers, including the fluid compressibility induced flow and the flow in/out the chambers. While p_1 and p_2 are the absolute pressure of the fluid in each chamber, the pressure difference between two chambers is $\Delta p = p_1 - p_2$, and the time derivative is:

$$\Delta\dot{p} = \dot{p}_1 - \dot{p}_2. \tag{4.3}$$

Applying Eq.(4.2) for each cylinder chamber and combine them with Eq. (4.3), the single-state model of this cylinder then can be derived as in [103], with assumed isothermal condition:

$$\Delta\dot{p} = B\left(\frac{1}{V_1(x_p)} + \frac{1}{V_2(x_p)}\right)\left[A_p\dot{x}_p - \sum_{j=1}^{N_F} Q_j(\Delta p)\right]. \tag{4.4}$$

where x_p and $\dot{x}_p$ are the piston displacement and velocity, $V_1(x_p)$ and $V_2(x_p)$ are the variable volumes of each chamber regard to x_p, A_p is the effective area of the piston, Q_j is the flow rate

of the jth path, and N_F is the number of flow paths. Therefore, the volumetric flow rate caused by the piston moving is $Q_p = A_p \dot{x}_p$, and $Q_N = \sum_{j=1}^{N_F} Q_j(\Delta p)$ is the total flow rate thought the flow paths. Further assumptions can be made to identify the characteristics of fluid compressibility and other flow paths:

- **Assumption 1:** $N_F = 0$
  Assuming no physical flow path connecting the two cylinder chambers, namely $Q_N = 0$, the flow rate caused by the piston is fully contributed by the fluid compressibility as $Q_p = Q_B$, then the pressure difference caused by fluid compressibility can be expressed by:

$$\Delta \dot{p} = B\left(\frac{1}{V_1} + \frac{1}{V_2}\right) Q_B. \tag{4.5}$$

- **Assumption 2:** $B = \infty$
  Due to the small mass of fluid in the external flow paths, assuming the incompressible fluid flow through the paths, $Q_N = Q_p = A_p \dot{x}_p$ is obtained according to Eq.(4.4). Since the flow rate through the paths can be specified by the static characteristics $Q_N = q\Delta p$ [102], in the inverse form,

$$\Delta p = q^{-1} Q_N. \tag{4.6}$$

  where q is the coefficient regard to the characteristics of hydraulic resistances (R) or hydraulic inertance (I), such as the pressure loss due to the orifice or the pressure difference required for the acceleration of flow. If negligible piston inertia and seal friction are assumed, the cylinder terminal force (F_p) and velocity (Δv_p) can be estimated by,

$$F_p = A_p \Delta p = A_p q^{-1} Q_N, \tag{4.7}$$

$$\Delta v_p = \frac{Q_N}{A_p} = \frac{q\Delta p}{A_p}. \tag{4.8}$$

The relationship $Q_p = Q_N = \sum_{j=1}^{N_F} Q_j$ reveals the parallel connection of the flow paths, which is consistent with the Kirchhoff's first law, while series connected flow restrictors possess the relationship among the pressure difference across: $\Delta p = \sum_{i=1}^{N_F} \Delta p_i$ according to Kirchhoff's second law, where N_F is the number of connected elements.

4.2.2 Force-Pressure analogy

In an earlier study, Schonfeld presented an analogy between mechanical and hydraulic systems [104], with the correspondence illustrated as below:

Mechanical		**Hydraulic**
Force (F)	$\Longleftrightarrow$	Pressure difference (ΔP)
Velocity difference (Δv)	$\Longleftrightarrow$	Flow rate (Q)
Stiffness (k)	$\Longleftrightarrow$	Compliance (C)
Damping (c)	$\Longleftrightarrow$	Resistance (R)
Inertia (m)	$\Longleftrightarrow$	Inertance (I)

where the mechanical stiffness (k) indicate the amount of elastic force to resist the deformation of the object, with the unit of N/m; the mechanical damping (c) is usually considered to be viscous drag, which is defined as the proportional relationship between the applied force and the relative velocity based on the property of the intermediate (e.g. the damping oil) that works against the motion, with the unit of Ns/m; and the mechanical inertance (m) is represented by the nature of the object to keep its state of relative rest or constant uniform motion, usually regarded as mass of the object, with the unit of kg.

On the other side, the hydraulic compliance (C) is due to the compressibility of fluid, which is defined as the volumetric change of fluid per unit of pressure difference, with the unit of m^2/N; the hydraulic resistance (R) is described as the pressure loss per unit of flow rate, caused by the friction in the tube, or the flow restrictions presented in the device, such as the tube inlet/outlet or the valves, with the unit of Ns/m^5; and the hydraulic inertance (I) is stated as the pressure difference needed for the acceleration/deceleration of the fluid flow, with the unit of kg/m^4.

In this work, with the introduction of inerter element, some adjustment need to be specified towards both the mechanical and hydraulic inertance accordingly. While the mechanical inertance (b) replace the original inertia (m) to provide the amplified inertial effect, the hydraulic inertance is further explained by the mass of fluid flow through the external channel, which is also phrased as inertial track by Flower [105].

Consequently, having the mass element to be replaced by inerter, the updated analogy between the mechanical and hydraulic network is shown in Fig. 4.2, where the mechanical inertance and damping are equivalent to the hydraulic inertance and resistance, while the mechanical stiffness has an inverse relationship to the hydraulic compliance. This analogy will be used for the modelling of fluid-based vibration suppression systems. Regard to each element, the defining relationship between the applied force and relative velocity, as well as the relationship between the flow rate and the pressure difference are demonstrated, together with the corresponding admittance. For hydraulic network, the admittance is defined as the pressure difference over

the flow rate. It is also worth mentioning that, in this analogy, the symbol used for mechanical inerter '⊣⊢' is consistent with [2], while the symbols used for hydraulic resistance '⫴', hydraulic inertance '⊣∿⊢' and hydraulic compliance '⊣⊓⊢' are consistent with those defined in [104].

Mechanical		Hydraulic	
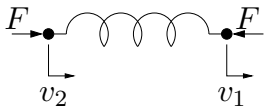 $\frac{dF}{dt} = k(v_2 - v_1)$	$Y(s) = \frac{k}{s}$ stiffness	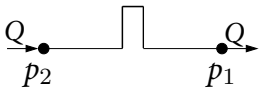 $\frac{d(p_2-p_1)}{dt} = \frac{1}{C}Q$	$Y(s) = \frac{1}{Cs}$ compliance
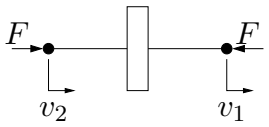 $F = b\frac{d(v_2-v_1)}{dt}$	$Y(s) = bs$ inertance	 $(p_2 - p_1) = I\frac{dQ}{dt}$	$Y(s) = Is$ inertance
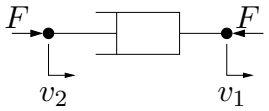 $F = c(v_2 - v_1)$	$Y(s) = c$ damping	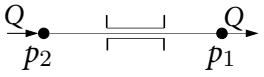 $(p_2 - p_1) = RQ$	$Y(s) = R$ resistance

Figure 4.2: The analogy between the mechanical and hydraulic networks, where F is the applied force on the element.

The typical coupling mechanism between the mechanical and hydraulic system is the piston moving axially inside the cylinder, which works as a mechanical-hydraulic converter to transform the admittance between the networks. Consider a hydraulic resistance between the two chambers of the cylinder shown in Fig. 4.1, the pressure difference across the piston is: $\Delta p = RQ$ according to Fig. 4.2, then substitute Eqs. (4.7) and (4.8) to get $F_p = {A_p}^2 R\Delta v_p$, therefore the equivalent mechanical damping is:

$$c = {A_p}^2 R. \tag{4.9}$$

Applying the same approach, the equivalent mechanical inertance and stiffness are derived:

$$b = {A_p}^2 I, \tag{4.10}$$

$$k = \frac{{A_p}^2}{C}. \tag{4.11}$$

Based on Eqs. (4.7) and (4.8), the mechanical through variable F_p is proportional to the hydraulic cross variable Δp and similarly, the mechanical cross variable Δv_p is corresponding to the hydraulic through variable Q_N. Furthermore, with the identified links between the hydraulic and equivalent mechanical elements in Eq. (4.9)-(4.11), their series and parallel topological connections can be similarly translated between each network. For example, assuming negligible seals friction, piston rod inertia and fluid elasticity, consider an external tube connecting the two chambers of the cylinder as shown in Fig. 4.3(a), when the piston moves with an acceleration, the hydraulic resistance (R) caused by the friction loss in the tube and the hydraulic inertance (I) because of the accelerated mass of fluid flowing through, are presented in series connection. This is because that while the same flow rate (Q) flowing through these two elements, the pressure difference Δp between two cylinder chambers is produced by the accumulated pressure drops due to the hydraulic resistance and inertance: $\Delta p = (R + Is)Q$, then substitute Eqs. (4.7) and (4.8) to get: $F_p = (R + Is)A_p A^2 \Delta v_p$, further transform the hydraulic elements to the equivalent mechanical elements according to Eqs. (4.9) and (4.10) to obtain: $F_p = (c + bs)\Delta v_p$. It is obvious the mechanical damping and inertance element are sharing the same velocity, in turn the parallel connection between them can be deduced as shown in Fig. 4.3(b).

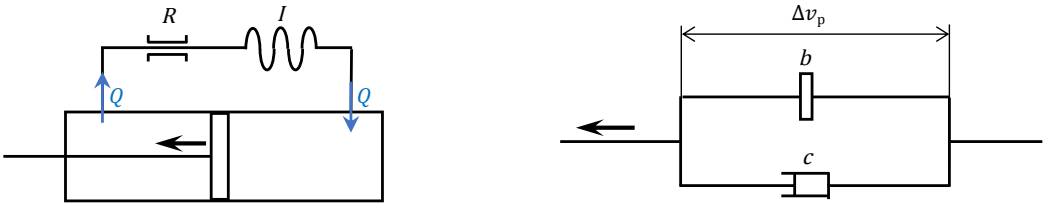

(a) (b)

Figure 4.3: The transformation from (a) hydraulic series connection to (b) mechanical parallel connection by a piston mechanism.

On the contrary, consider a given mechanical system consists of two dampers due to the valve on piston and the friction loss through the external tube, connected in series as shown in Fig. 4.4(a), the force through them have the equal values: $\frac{F_p}{c_1} + \frac{F_p}{c_2} = \Delta v_p$. Substitute Eqs. (4.7) and (4.8) to get: $\frac{\Delta p {A_p}^2}{c_1} + \frac{\Delta p {A_p}^2}{c_2} = Q$, then transform the mechanical damping to equivalent hydraulic resistance according to Eq. (4.9): $\frac{\Delta p}{R_1} + \frac{\Delta p}{R_2} = Q$. It can be seen that the two resistance produce the same pressure difference due to the equal force applied to the piston (Eq. (4.7)), and the total flow rate through the two chambers are obtained by adding up the two branch flow rate through each resistance with corresponding piston velocity across (Eq. (4.8)). Therefore the parallel connection between them is deduced as shown in Fig. 4.4(b).

As the two cases illustrated, it can be seen that, when a hydraulic network has the equivalent mechanical network, the series/parallel coupling of elements in one network is equivalent to

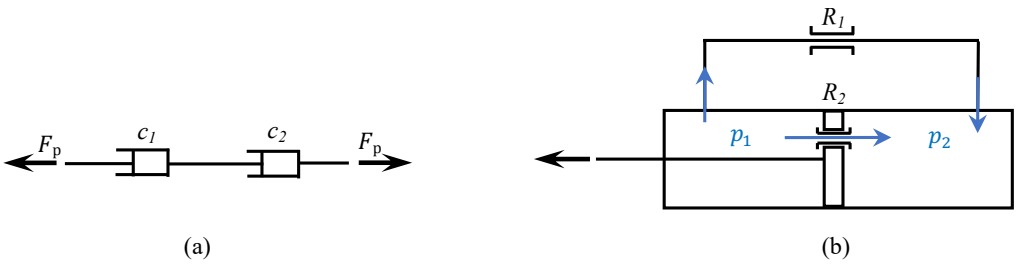

Figure 4.4: The transformation from (a) mechanical series connection to (b) hydraulic parallel connection by a piston mechanism.

the parallel/series coupling in the other network. This is consistent with the conclusion derived in [104], where the author stated that the equivalent mechanical and hydraulic systems are always dual to each other, and the series/parallel connections are required to switch between two networks as well.

The modified force-pressure analogy will be adopted for later construction of the hydraulic and the equivalent mechanical networks in this work. Also, the mechanical elements will be obtained based on the corresponding hydraulic counterparts by applying this analogy.

4.3 Network representation of a fluid-based inerter design

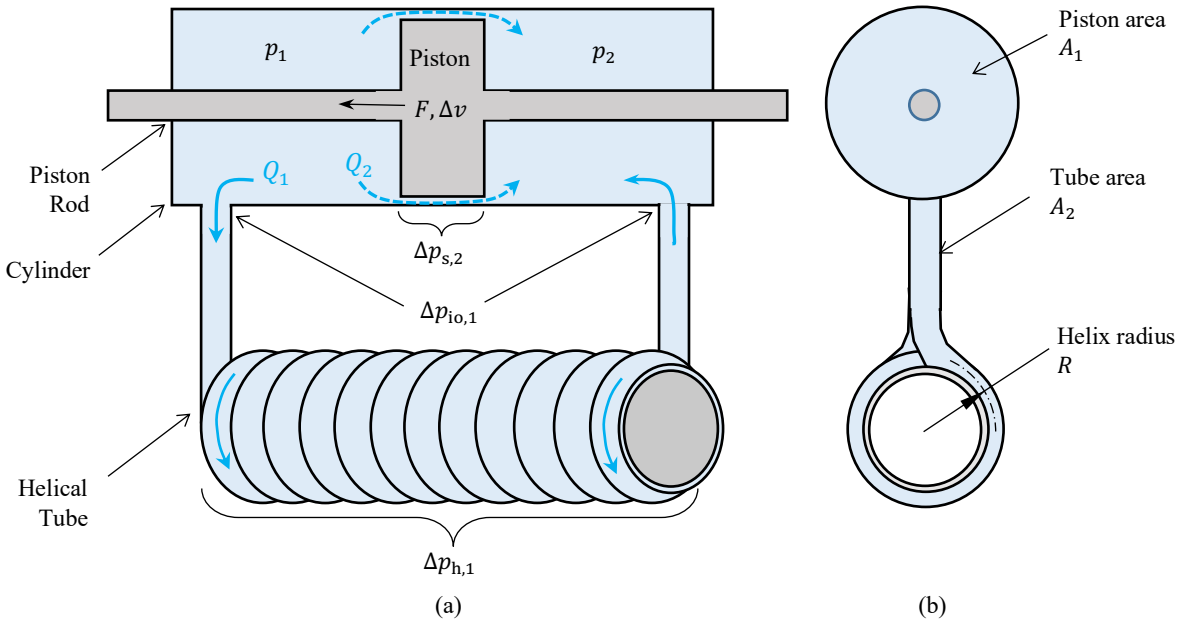

Figure 4.5: Schematic of a helical-tube fluid inerter from (a) the elevation and (b) the end view (the induced flow Q_3 is not shown).

Fluid-based inerter uses the acceleration of the mass of fluid flowing through an external channel to produce axial inertance. The schematic plot of a helical-tube fluid inerter is shown in Fig. 4.5(a) as a typical design example. When the piston rod moves with velocity Δv relative to the cylinder under a force F towards the left, the working fluid flows through the external channel (as a helical tube in this example) with volume flow rate Q_1. The pressure inside each cylinder chamber is assumed to be homogeneously distributed, p_1 is the absolute pressure in the left chamber and p_2 is the absolute pressure in the right chamber. Typically, for these conditions, it can be assumed $p_1 > p_2$ when the rod is moving to the left. The pressure difference ($\Delta p = p_1 - p_2$) between two chambers is caused by the pressure drop across the inlet/outlet of the helical tube ($\Delta p_{io,1}$) and the pressure drop through the helical tube channel ($\Delta p_{h,1}$). Meanwhile, from the left to right, any hypothetical gap between the piston and the cylinder wall can provide an alternative route for the working fluid to flow with volume flow rate Q_2. This flow leads to a pressure drop $\Delta p_{s,2}$, where $\Delta p_{s,2} = \Delta p$. Apart from these physical flows, an induced flow corresponding to the compressibility effects of the fluid might also exist. Assuming no fluid flow through the external channel when piston moves a small distance towards the left, an pressure difference between the cylinder chambers $\Delta p_{c,3}$ is produced by the compression of fluid in the left chamber with equivalent volume flow rate Q_3. The fluid volume in the external channel is negligible due to its relatively small size. Note that Q_3 is not included in Fig. 4.5(a) because it does not correspond to a specific physical path. Furthermore, the mechanical properties, such as the friction due to the seals, are neglected for the derivations of the hydraulic networks in this chapter. The mass of the piston is generally neglected due to its relatively low inertia.

A fluid-based inerter produces effects such as damping, stiffness and inertance. Consider the flow paths discussed above, the main branch with flow rate Q_1 is through the external channel. This flow produces hydraulic inertance because of the mass of the fluid flowing through, and the hydraulic resistance due to the friction loss through the channel, as well as the flow restrictions at the inlet and outlet. Another considered flow branch represents the flow between the piston and the cylinder walls with flow rate Q_2. Furthermore, the compressibility effects of the fluid is modelled as an additional flow path between the terminals of the hydraulic system. The corresponding flow rate (Q_3) between the working volumes is expressed based on Eq. (4.5) [103]:

$$Q_3 = C_{c,3}\Delta\dot{p}, \tag{4.12}$$

where $C_{c,3}$ is used to represent the effective hydraulic compliance [106], and $C_{c,3} = \frac{V}{4B}$ when the volume of each cylinder chamber are both assumed to be half of the total chamber volume V.

In order to establish the linear lumped parameter models in both the hydraulic and mechanical domains, the relations between flow rates and pressure drops in the fluid-based inerter are assumed to be linear at this stage. The variables $R_{io,1}$, $R_{h,1}$ and $R_{s,2}$ are defined as the hydraulic resistances due to the inlet/outlet of the cylinder, the external channel and the leakage across the piston, respectively. The hydraulic inertance of the mass flowing through the external channel

is defined as $I_{h,1}$ [106]. These parameters are dependent on the fluid properties and prototype dimensions, which will be either specified or identified in Chapter 6. Based on the schematic shown in Fig. 4.5(a) and the considered flow branches, the hydraulic network of a fluid-based inerter is constructed as shown in Fig. 4.6.

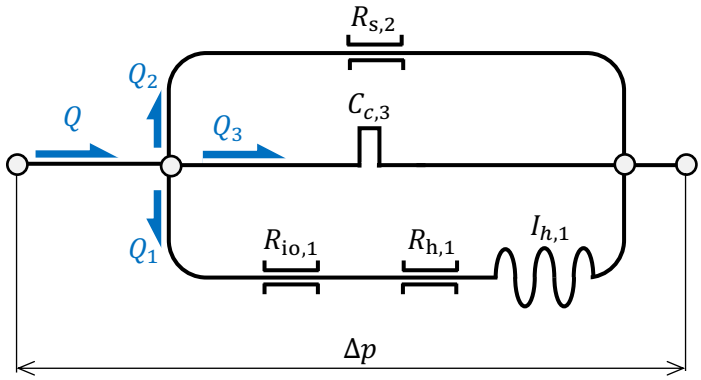

Figure 4.6: The hydraulic network of a fluid-based inerter characterising the relation between the total flow rate Q and pressure difference Δp.

According to Kirchhoff's first law, the total flow rate (Q) consists of individual flow rates through each branch:

$$Q = Q_1 + Q_2 + Q_3. \tag{4.13}$$

Based on the relationships for each hydraulic element shown in Fig. 4.2, the pressure difference between the cylinder's two chambers (Δp) can then be written as branch flow rates (Q_1 and Q_2) related:

$$\Delta p = R_{h,1}Q_1 + R_{io,1}Q_1 + I_{h,1}\dot{Q}_1 = R_{s,2}Q_2. \tag{4.14}$$

In the Laplace domain and under zero initial condition, substituting Eq. (4.12) and Eq. (4.14) into Eq. (4.13), the relation between the total flow rate Q and pressure difference Δp can be derived:

$$\hat{Q} = \left({R_{s,2}}^{-1} + (R_{h,1} + R_{io,1} + I_{h,1}s)^{-1} + C_{c,3}s\right)\Delta\hat{p}. \tag{4.15}$$

where s represents the complex variable and '$\wedge$' denotes the Laplace transform of the variables. The terminal behaviour of an inerter device is usually characterised by the relation between the force through the device (F_H) due to the hydraulic elements (abbreviated in the present study as 'hydraulic force') and the relative terminal velocity (Δv). These variables have following relations with the hydraulic ones,

$$F_H = A_1 \Delta p, \tag{4.16}$$

$$\Delta v = \frac{Q}{A_1}, \tag{4.17}$$

where A_1 is the effective piston area. Substituting Laplace transforms of Eq. (4.16) and Eq. (4.17) into Eq. (4.15), the following equation is obtained,

$$\begin{aligned} \frac{\hat{F}_H}{\Delta \hat{v}} &= \frac{{A_1}^2}{{R_{s,2}}^{-1} + \left(R_{h,1} + R_{io,1} + I_{h,1}s\right)^{-1} + C_{c,3}s} \\ &= \frac{1}{\left(R_{s,2}{A_1}^2\right)^{-1} + \left(R_{h,1}{A_1}^2 + R_{io,1}{A_1}^2 + I_{h,1}{A_1}^2 s\right)^{-1} + C_{c,3}{A_1}^{-2}s} \end{aligned} \tag{4.18}$$

Notice that Eq. (4.18) now describes the terminal force-velocity behaviour of the device. If relevant network synthesis techniques (e.g. [100, 107]) are applied to Eq. (4.18) , the solution is not unique, which means multiple networks can be obtained. However, in order to link every mechanical component directly with the corresponding hydraulic component in Fig. 4.6, each hydraulic variable is transferred to its mechanical counterpart. In this way, the equivalent mechanical network is drawn, as shown in Fig. 4.7 with the corresponding admittance:

$$\frac{\hat{F}_H}{\Delta \hat{v}} = \frac{1}{{c_{s,2}}^{-1} + \left(c_{h,1} + c_{io,1} + b_{h,1}s\right)^{-1} + {k_{c,3}}^{-1}s}, \tag{4.19}$$

where the mechanical inertance $b_{h,1} = I_{h,1}{A_1}^2$, mechanical stiffness $k_{c,3} = {A_1}^2/C_{c,3}$, and mechanical damping $c_{io,1}$, $c_{h,1}$, $c_{s,2}$ is equal to $R_{io,1}A_1^2$, $R_{h,1}A_1^2$ and $R_{s,2}A_1^2$, respectively. The links are consistent with Eqs. (4.9), (4.10) and (4.11) that are identified based on force-pressure analogy. It is worth pointing out that, following this procedure, the topology of the hydraulic network (Fig. 4.6) will always be the dual to the equivalent mechanical network (Fig. 4.7). This is because the mechanical through variable F_H [10] is proportional to the hydraulic cross variable Δp and similarly, the mechanical cross variable Δv is corresponding to the hydraulic through variable Q, see Eq. (4.16) and Eq. (4.17).

Additionally, in Fig. 4.7, v_1 and v_4 are the velocities of each device terminals, where the relative terminal velocity $\Delta v = v_4 - v_1$; and v_2, v_3 represent internal velocities of the equivalent mechanical network. Variables $\Delta v_{h,1}$, $\Delta v_{b,1}$ and $\Delta v_{io,1}$ are introduced to represent the relative terminal velocities of $c_{h,1}$, $b_{h,1}$ and $c_{io,1}$ in Fig. 4.7. Since these elements share the same terminals, $\Delta v_{h,1} = \Delta v_{b,1} = \Delta v_{io,1} = v_3 - v_2$. The advantage of the proposed procedure is that each flow rate through $R_{s,2}$, $C_{c,3}$, $R_{io,1}$, $R_{h,1}$ and $I_{h,1}$ in the hydraulic network relates to the relative velocity across $c_{s,2}$, $k_{c,3}$, $c_{io,1}$, $c_{h,1}$ and $b_{h,1}$ in the mechanical network, respectively, with the following equations,

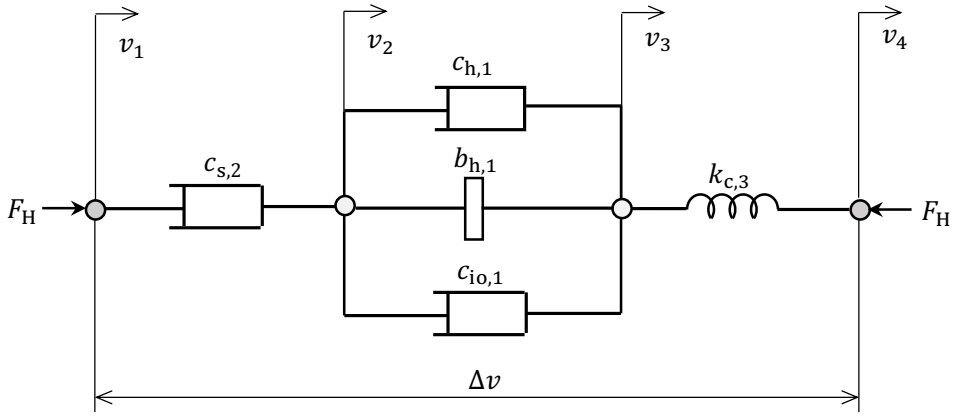

Figure 4.7: The equivalent mechanical network of a fluid-based inerter characterising the relation between the hydraulic force F_H and relative terminal velocity Δv.

$$\Delta v_{h,1} = \Delta v_{b,1} = \Delta v_{io,1} = v_3 - v_2 = \frac{Q_1}{A_1}, \tag{4.20}$$

$$\Delta v_{s,2} = v_2 - v_1 = \frac{Q_2}{A_1}, \tag{4.21}$$

$$\Delta v_{c,3} = v_4 - v_3 = \frac{Q_3}{A_1}. \tag{4.22}$$

Also, each relative pressure drop across $R_{s,2}$, $C_{c,3}$, $R_{io,1}$, $R_{h,1}$ and $I_{h,1}$ in the hydraulic network relates to the force through $c_{s,2}$, $k_{c,3}$, $c_{io,1}$, $c_{h,1}$ and $b_{h,1}$ in the mechanical network, in the similar way.

4.4 Network representation of a fluid-inerter integrated damping (FID) device

In a typical hydraulic damper, there is usually a valve or a few valves in the piston (called piston valve in this work), which are used as a flow restriction feature to provide hydraulic resistance when the piston moves relative to the cylinder. This hydraulic resistance results in a damping force across the device terminals. The FID device is a combination of the hydraulic damper and the fluid-based inerter, which allows the damping and inertance effects to be combined in a single device.

Based on the fluid-based inerter in Section 4.3, in order to incorporate the property of the hydraulic damper, a new flow path through the piston valves is introduced as shown in Fig. 4.8, which results in an additional flow path with flow rate Q_4 shown in Fig. 4.9. In the corresponding hydraulic network in Fig. 4.9, the hydraulic resistance $R_{v,4}$ is present because of the pressure loss across the flow restrictions at the valves. It corresponds to the damping effect $c_{v,4}$ in the equivalent

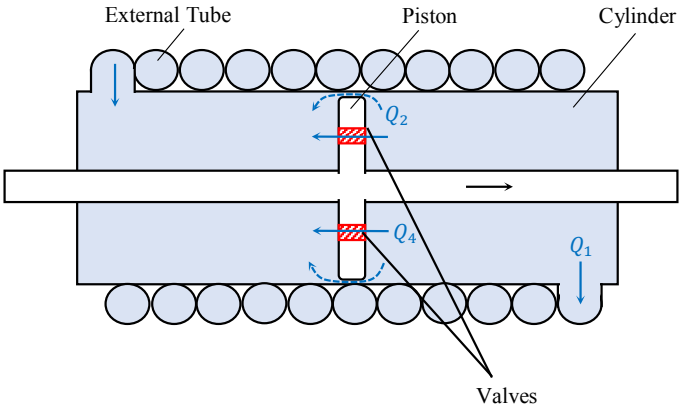

Figure 4.8: The schematic diagrams for a FID device.

mechanical network. The remaining part of this subsection focuses on establishing the equivalent mechanical network (Fig. 4.10) for the FID device. The same approach for the establishment of Fig. 4.7 as the one used in Section 4.3 will be applied. Hence the procedure is only described briefly here. It is worth mentioning that when the linear assumptions on hydraulic elements do not hold, the stated relations between hydraulic and mechanical element values do not hold either. However, the defined network transformation relations between hydraulic variables (flow rate and pressure difference) and mechanical variables (force and velocity difference) still hold. This point will be discussed in details below.

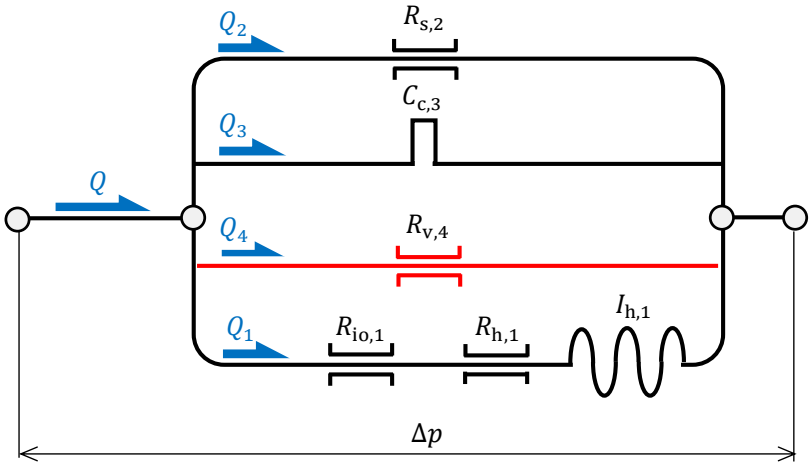

Figure 4.9: The corresponding hydraulic network of the FID device in Fig. 4.8.

In order to reveal the topological connection of different elements in mechanical domain for the FID device shown in Fig. 4.8, the relations between the flow rates and pressure drops are assumed to be linear at this stage. Therefore, as the corresponding hydraulic network shown in Fig. 4.9, the relationships between the pressure difference Δp and branch flow rates can be

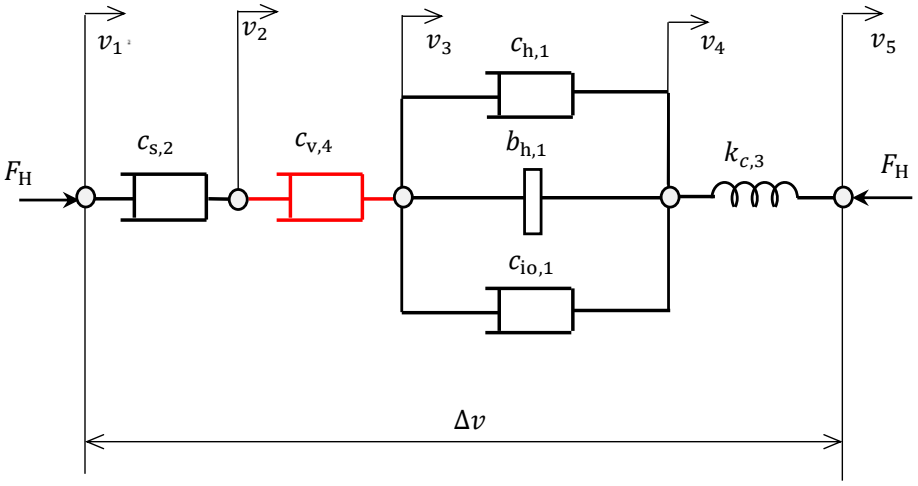

Figure 4.10: The equivalent mechanical network of the FID device in Fig. 4.8.

written based on the relationships for each hydraulic element shown in Fig. 4.2,

$$\Delta p = R_{h,1}Q_1 + R_{io,1}Q_1 + I_{h,1}\dot{Q}_1 = R_{s,2}Q_2 = \frac{1}{C_{c,3}}\int Q_3 \delta t = R_{v,4}Q_4. \tag{4.23}$$

Since the total flow rate $Q = Q_1 + Q_2 + Q_3 + Q_4$, with assumption of zero initial condition, the relation between Q and Δp can then be written in the Laplace domain as:

$$\hat{Q} = \left(\left(R_{h,1} + R_{io,1} + I_{h,1}s \right)^{-1} + {R_{s,2}}^{-1} + C_{c,3}s + {R_{v,4}}^{-1} \right) \Delta \hat{p}, \tag{4.24}$$

Subsequently, the admittance function that characterises the terminal force-velocity behaviour, can be derived by substituting Eqs. (4.16) and (4.17) into Eq. (4.24),

$$\begin{aligned} \frac{\hat{F}_H}{\Delta \hat{v}} &= \frac{{A_1}^2}{(R_{h,1} + R_{io,1} + I_{h,1}s)^{-1} + {R_{s,2}}^{-1} + C_{c,3}s + {R_{v,4}}^{-1}} \\ &= \frac{1}{(R_{h,1}{A_1}^2 + R_{io,1}{A_1}^2 + I_{h,1}{A_1}^2 s)^{-1} + (R_{s,2}{A_1}^2)^{-1} + C_{c,3}{A_1}^{-2}s + (R_{v,4}{A_1}^2)^{-1}}. \end{aligned} \tag{4.25}$$

As before, multiple mechanical realisations can be obtained to realise the admittance function Eq. (4.25) by applying different network synthesis procedures, e.g. [100]. The equivalent mechanical network shown in Fig. 4.10 is chosen because of the direct relationship between the mechanical elements and the hydraulic elements in Fig. 4.9, which is similar to the network synthesis in Fig. 4.7. Correspondingly, Eq. (4.25) can be rearranged as:

$$\frac{\hat{F}_H}{\Delta\hat{v}} = \frac{1}{(c_{h,1}+c_{io,1}+b_{h,1}s)^{-1}+{c_{s,2}}^{-1}+{k_{c,3}}^{-1}s+{c_{v,4}}^{-1}}, \tag{4.26}$$

where $c_{v,4}$ is the piston valve damping due to the hydraulic resistance $R_{v,4}$. Based on Eqs. (4.9), (4.10) and (4.11), it can also be defined that the inertance $b_{h,1} = I_{h,1}{A_1}^2$, stiffness $k_{c,3} = {A_1}^2/C_{c,3}$, damping $c_{io,1}$, $c_{h,1}$, $c_{s,2}$,$c_{v,4}$ equal $R_{io,1}A_1^2$, $R_{h,1}A_1^2$, $R_{s,2}A_1^2$ and $R_{v,4}A_1^2$, respectively. Similar to the fluid-based inerter, the equivalent mechanical network of such device is always in dual to the hydraulic network [108]. It is worth mentioning that when the linear assumption of hydraulic properties does not hold, these component transformation relationships will not hold.

Apart from the apparent advantage of relating each hydraulic element with the corresponding mechanical element, another important benefit of using this network synthesis approach to obtain the mechanical network is that according to the duality between the hydraulic and derived mechanical networks, each flow rate variable through (and each pressure drop variable across) the hydraulic elements in Fig. 4.9 is linked with the relative velocity variable across (and each force variable through) the corresponding mechanical elements in Fig. 4.10. For example, the relative velocity ($\Delta v_{b,1}$, $\Delta v_{h,1}$ and $\Delta v_{io,1}$) across the inerter ($b_{h,1}$), external tube damper ($c_{h,1}$) and inlet/outlet damper ($c_{io,1}$):

$$\Delta v_{b,1} = \Delta v_{h,1} = \Delta v_{io,1} = v_4 - v_3 = \frac{Q_1}{A_1}; \tag{4.27}$$

the relative velocity ($\Delta v_{s,2}$) across the leakage damper ($c_{s,2}$):

$$\Delta v_{s,2} = v_2 - v_1 = \frac{Q_2}{A_1}; \tag{4.28}$$

the relative velocity ($\Delta v_{c,3}$) across the fluid spring ($k_{c,3}$):

$$\Delta v_{c,3} = v_5 - v_4 = \frac{Q_3}{A_1}; \tag{4.29}$$

the relative velocity ($\Delta v_{v,4}$) across the piston valve damper ($c_{v,4}$):

$$\Delta v_{v,4} = v_3 - v_2 = \frac{Q_4}{A_1}. \tag{4.30}$$

Similarly, each force ($F_{hI,1}$, $F_{hR,1}$, $F_{io,1}$, $F_{s,2}$, $F_{c,3}$ and $F_{v,4}$) through the mechanical elements equals the piston area (A_1) times the corresponding pressure drop ($\Delta p_{hI,1}$, $\Delta p_{hR,1}$, $\Delta p_{io,1}$, $\Delta p_{s,2}$, $\Delta p_{c,3}$ and $\Delta p_{v,4}$) across the hydraulic elements ($b_{h,1}$, $c_{h,1}$, $c_{io,1}$, $c_{s,2}$, $k_{c,3}$ and $c_{v,4}$). It worth noting that even when the linear assumptions of hydraulic elements do not hold, the network relations of Eqs. (4.27) - (4.30) are still valid. This is because the topological connections of the device do not change, and are correctly reflected by both the hydraulic and mechanical networks.

4.5 Summary

For the modelling of fluid-based vibration suppression devices, the analogy between the mechanical and hydraulic systems is modified by replacing the mass element by inerter. The single-state pressure difference model for an ideal damper is introduced with two sets of assumptions: the compressible fluid in the chamber without the branch flow paths and the incompressible fluid in the flow paths, which are used to identify the pressure-flow rate relationships, as well as the corresponding piston force and velocity. Meanwhile, the transformation of admittance and series-parallel coupling between the two networks are also discussed with two examples. The conclusion indicates that if the hydraulic network has an equivalent mechanical network, the hydraulic series connection will be translated to mechanical parallel connection, and vise versa.

Subsequently, followed the working principle of fluid-based inerters being explained, the hydraulic networks of the fluid-based inerter and FID device are obtained by analysing flow distributions. With the help of the network synthesis approach and the updated force-pressure analogy, the equivalent mechanical networks are also derived, with each hydraulic element directly linked with the mechanical counterpart. Besides, due to the hydraulic through variable is linked with the mechanical cross variable, and vise versa, the hydraulic and derived mechanical networks are dual to each other. Both the derived hydraulic and mechanical networks are essential for the prototypes design and models development in the following chapters.

CHAPTER 5

PROTOTYPES AND TEST RIG DEVELOPMENT

5.1 Overview

Based on the schematics and corresponding networks of the fluid-based inerter devices, this chapter introduces a few prototypes of the conceptual designs. The design parameters of the helical-tube fluid inerter are first analysed and identified, then the prototypes are developed together with the customised test rig for experimental testing. Meanwhile, the prototypes of the alternative designs are also presented and discussed. Furthermore, the modification of the helical-tube fluid inerter prototype is carried out to realise the FID device, and the corresponding test rig is updated as well. Finally, the measuring instruments in the test rig are calibrated to prepare for the experimental testings.

5.2 Helical-tube fluid inerter

While there are various of fluid-based inerter designs, the helical-tube arrangement is the most common design among them. A prototype of the helical-tube fluid inerter is needed for model development of fluid-based inerter with specialised test rig. In order to build the prototype with better representative inertance effect, the design parameters need to be scientifically selected. Therefore, the corresponding conditions/restrictions are presented and analysed. Accordingly, the prototype and test rig are built for experimental testing.

5.2.1 Design parameter identification

According to the schematic plot in Fig. 5.1, a helical-tube fluid inerter mainly consists of the cylinder, external tube and working fluid. While the performance of the device is directly linked

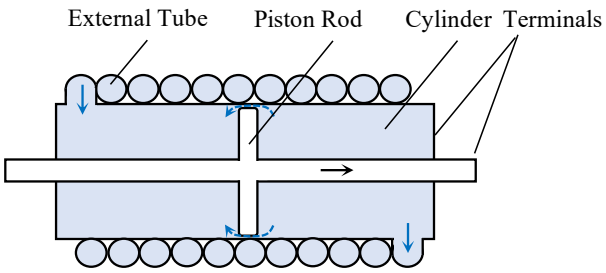

Figure 5.1: Schematic of a helical-tube fluid inerter.

with the dimensions of each part and the properties of the fluid, the selections of parts and fluid must be based on the expected performance of the prototypes. Along with the introduction of inerter, Smith [2] also raised a few conditions for the practically useful inerter to be realised:

1. The device should have a comparatively large inertance to mass ratio.
2. No terminal of the device needs to be connected to the mechanical ground.
3. The stroke of the device should be finite and linear, the dimension of the device should be reasonable as well.
4. The device should be capable of working in any orientation or motion.

In terms of the condition 1, the target inertance of the prototype is set to be at least 200 kg, which is approximately the mean value of the previous studied inertance [4]. Such inertance is much larger then the mass of device that is usually below 5 kg. Regarding to the condition 2, a through-rod cylinder is chosen to keep the constant chamber volume in the cylinder during the moving of piston rod, while the cylinder body and piston rod are treated as two terminals of the device. The chosen cylinder has bore size $d_1 = 40$ mm, rod diameter $d_0 = 16$ mm, stroke $L_s = 200$ mm and chamber length $L = 217$ mm, which all satisfies the condition 3. Moreover, the seal structure of the cylinder ensures the device can function adequately in any orientation as required by condition 4.

Another important design consideration is the break frequency (f_b), which means the frequency at which the dynamic behaviour of the device changes from a damping dominated response to an inertance dominated response. Based on the results in [4], the main parasitic damping is in parallel with the inertance. Therefore the admittance of the ideal fluid inerter in the Laplace domain can be written as:

$$\frac{F}{\Delta v} = bs + c', \tag{5.1}$$

where the c' is the linearised parasitic damping coefficient at a certain frequency. In the frequency domain, the admittance is expressed as:

$$G(j\omega) = \frac{F(j\omega)}{\Delta v(j\omega)} = j\omega b + c', \tag{5.2}$$

where ω is the frequency in rad/s. Then the gain and phase of the linearised fluid inerter are derived as:

$$|G(j\omega)| = \sqrt{\omega^2 b^2 + c'^2}, \tag{5.3}$$

$$arg\,(G(j\omega)) = arctan\left(\frac{\omega b}{c'}\right), \tag{5.4}$$

Since the phase for ideal damping is 0° and for inerter is 90°, the break frequency (f_b) in Hz can be chosen as the frequency when phase angle $arg\,(G(j\omega))$=45°. From this,

$$f_b = \frac{c'}{2\pi b}. \tag{5.5}$$

Based on the formulae derived in [4], the inertance (b), parasitic damping force (F_c) and corresponding break frequency (f_b) can be calculated:

$$b = \rho l\ \frac{{A_1}^2}{A_2}, \tag{5.6}$$

$$F_c = 0.03426\frac{2\rho l A_1}{\sqrt{D_h R}}\left(\frac{A_1}{A_2}\right)^2 \Delta v^2 + 17.54\frac{2\mu l A_1}{{D_h}^2}\left(\frac{A_1}{A_2}\right)\Delta v, \tag{5.7}$$

$$f_b = \frac{F_c}{2\pi b \Delta v}. \tag{5.8}$$

where ρ is the density of the fluid, l is the total length of the external tube, $D_h = d_2$ (when tube is full of fluid) is the tube hydraulic diameter, R is the tube helix radius (based on the chosen tube coil with outer diameter of 8 mm), Δv is the relative terminal velocity, $A_1 = \pi(d_1/2)^2 - \pi(d_0/2)^2$ is the effective piston area, and $A_2 = \pi(d_2/2)^2$ is the tube cross-sectional area (for the definitions of d_0, d_1 and d_2 refer to Table 5.1).

Table 5.1: The estimated parasitic damping, inertance and break frequency for helical-tube fluid inerter with various tube inner diameters.

	Descriptions	**Tube 1**	**Tube 2**	**Tube 3**
Tubes	Tube inner diameter d_2 [mm]	4	6	8
	Tube helix radius R* [mm]	40.5	41.5	42.5
	No. of tube turns N(total length l [m])	10(2.36)	22(5.18)	39(9.19)
	Tube thickness t [mm]	1	1	1
Cylinder	Cylinder diameter d_1 [mm]		40	
	Rod diameter d_0 [mm]		16	
Fluid	Fluid density ρ [kg/m^3]		1000	
	Dynamic viscosity μ [Pa s]		0.001	
Device Properties	Parasitic damping force F_c [N]	178.4	62.7	30.5
	Inertance b [kg]	208.9	204.3	203.7
	Break frequency f_b [Hz]	3.4	1.2	0.6

*R is measured based on the bend radius of helical tube coil in Table 5.2

In order to enlarge the inerance-dominated frequency range, namely to lower the break frequency, three available helical tubes with inner diameters (d_2) of 4 mm, 6 mm and 8 mm are taken into consideration at a moderate velocity $\Delta v = 0.04$ m/s (amplitude of 0.01 m and frequency of 1 Hz). In this work, water is chosen as the working fluid due to its low compressibility and cleanliness. Therefore, to meet the target inertance ($b \geqslant 200$ kg), the corresponding break frequency f_b are calculated for each tube option based on the properties of the fluid and the dimension of the parts, as shown in Table 5.1. Although the break frequency is as low as possible to maximise the inerter active range, the geometrical restriction of the device rejects the choice of tube 3 ($d_2 = 8$ mm) because the total length of the tube winding ($d_2 \times N = 0.39$ m) is beyond the length of the cylinder (0.247 m). Consequently, the tube with inner diameter of 6 mm (with specifications shown in Table. 5.2) is chosen for the prototype of helical-tube fluid inerter, which could potentially provide 204.3 kg inertance with the break frequency of 1.2 Hz.

Table 5.2: Specifications of the parts for building of the helical-tube fluid inerter prototype.

Parts	**Specifications**
Cylinder	CAMOZZI Series 60 60M6L040A0200, double-acting, through-rod, bore $d_1 = 40$ mm, rod diameter $d_0 = 16$ mm, stroke $L_s = 200$ mm and chamber length $L = 217$ mm
External tube	CAMOZZI BS5409 flexible nylon recoil TRNR-1005, outer diameter $d_{2out} = 10$ mm, inner diameter $d_2 = 8$ mm, total length $l = 5.59$ m
Tube coil core	Perspex tube with outer diameter $d_{out} = 75$ mm, and length $l = 0.247$ m
Ball valve	CAMOZZI Type 3600 3-way L-port ball valve

5.2.2 Prototype and test rig development

With the chosen cylinder and external tube, the prototype of a helical-tube fluid inerter is built for the purpose of testing, as shown in Fig. 5.2. It uses the independent helical tube coil, which is easy to replace the helical tubes with various diameters and bend radii for comprehensive test requirements. The additional ball valves (with specifications shown in Table. 5.2) can partially isolate the cylinder chambers and helical tube channel, which enables fluid filling and helical tube replacement. Also, the two pressure gauges are designed to precisely record the working fluid pressures at the inlet and outlet of the helical tube. In Chapter 6, all the theoretical and experimental results are based on this prototype, and its design parameters are listed in Table 5.3. It is noted that the temperature of fluid is kept approximately at 30°C according to the average measured temperature of the cylinder shell during the tests. Additionally, it is worth mentioning that the whole process of the prototype assembly is carried out under the water, the reason of using this method is trying to minimise the amount of unexpected air trapped inside the prototype, which might significantly influence the properties of the device, especially the effective fluid stiffness. This effect due to the presence of air will be discussed in later chapters.

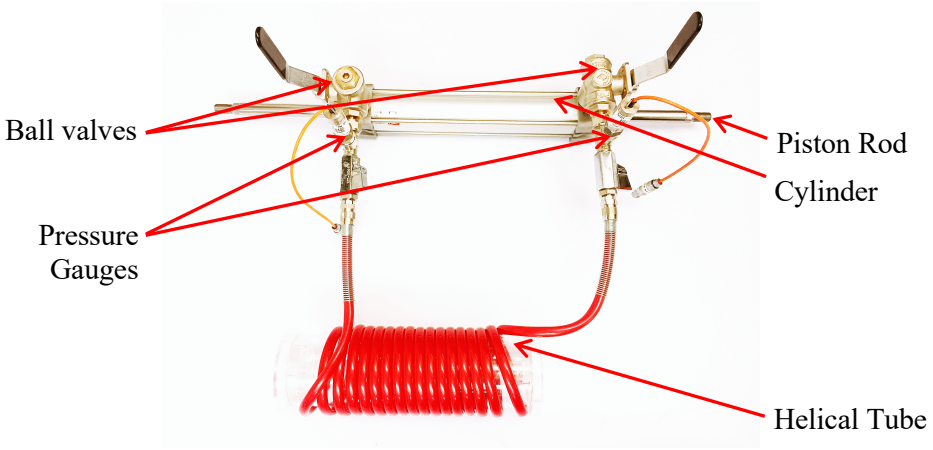

Figure 5.2: The helical-tube fluid inerter prototype built at the University of Bristol.

As shown in Fig. 5.3, the prototype of the helical-tube fluid inerter is placed in the customised test rig in the Automatic control and testing laboratory (ACTLab). Displacement-controlled excitations are generated by a hydraulic actuator, which is connected to the rod of the prototype. During the tests, the strut displacement across the prototype terminals is recorded by a Linear Variable Differential Transformer (LVDT), which is placed in parallel with the inerter device. This configuration minimises the recorded backlash effects from the joints between the actuator and the prototype terminal. The strut force of the prototype is collected using a load cell, which is located between the actuator and inerter piston rod. The two pressure gauges are placed at both ends of the helical tube to monitor the pressure changes in the helical tube during the tests. The specifications of the equipped instruments are listed in Table 5.4.

Table 5.3: Design parameters of the helical-tube fluid inerter prototype.

Description	**Value**
Piston area $A_1{}^*$ (m^2)	1.1×10^{-3}
Tube area $A_2{}^*$ (m^2)	2.8×10^{-5}
Helix radius R^* (m)	0.0415
Helical tube length l (m)	5.59
Cylinder chamber length L (m)	0.217
Tube hydraulic diameter D_h (m)	0.006
Working fluid density ρ at 30 °C ($kg \cdot m^{-3}$)	995.6
Working fluid viscosity μ at 30 °C ($Pa \cdot s$)	7.98×10^{-4}

*refer to Fig. 4.5(b)

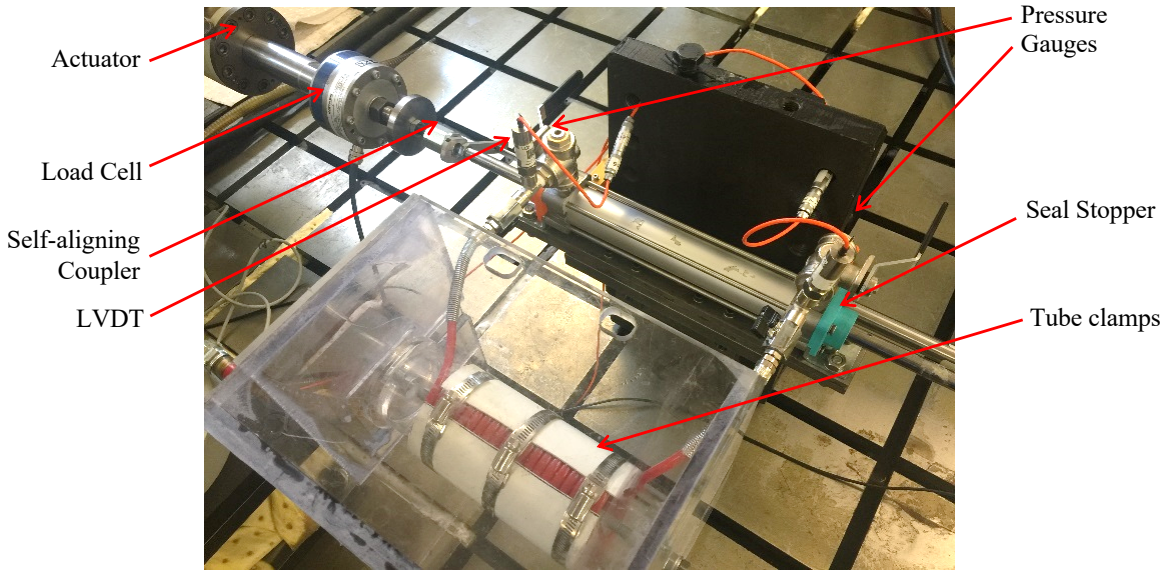

Figure 5.3: The test rig for the helical-tube fluid inerter.

Furthermore, in order to adjust the misalignment at the connection between the actuator and prototype, a self aligning coupler is employed to improve the alignment. A sets of tube clamps are used to tighten up the helical tube coil to avoid the oscillation of tube during the tests, especially with high flow rate through the tube. It is also worth mentioning that since the seals on both ends of the cylinder can not withstand large strut force, two seal stoppers are tailored to mechanically reinforce the seals against large pressure produced inside the cylinder chamber.

This test rig, including the equipped prototype, will be used for the model development of fluid-based inerter in Chapter 6.

Table 5.4: Specifications of the instruments used in the test rig of the helical-tube fluid inerter prototype.

Instruments	**Specifications**
Actuator	INSTRON PL25 kN Hydropuls linear hydraulic actuator, stroke: 240 mm
Load cell	INSTRON 43629, dynamic rating: ±25 kN
LVDT	RDP DCTH6000C, range: ±150 mm
Pressure gauge	Druck PDCR 822, operating range: 15 bar

5.3 Alternative designs of fluid-based inerter

In this section, two alternative designs of fluid-based inerter are presented and discussed. Firstly, a compact prototype of the fluid-based inerter is made with concentric tube arrangement, which not only could be used for better demonstration of the inerter mechanism, but also reveal the potential of such device being applied in industrial area. Secondly, a meander-tube fluid inerter is introduced and theoretically studied towards its distinct damping property. It is worth mentioning that both prototypes will not be used for experimental testing in this work due to the device or facility restrictions.

5.3.1 Compact helical-tube design

The prototype presented in this subsection was modified based on the one built in 4th year group project [109].

For better demonstration of the practical helical-tube design, a compact helical-tube fluid inerter is built with the external tube wrapping around the cylinder concentrically. As the prototype shown in Fig. 5.4, this symmetrical design further enhances the robust performance of the device to function in any orientation as required by condition 4 in Section 5.2.1. The parameters of the prototype are listed in Table 5.5, it can be seen that the inertance to mass ratio is large enough for the device to behave as an effective inerter. It is also noted that this prototype will not be tested in this work due to the difficulties for mounting the device to the test rig, and the lack of flexibility for switching tubes to meet different test requirements.

Table 5.5: Parameters of the compact helical-tube fluid inerter prototype.

Description	**Value**
Piston diameter d_1 (mm)	25
Rod diameter d_0 (mm)	10
Tube inner diameter d_2 (mm)	6
Helical tube length l (m)	6.86
Inertance b (kg)	41.3
Inertance-mass ratio	40

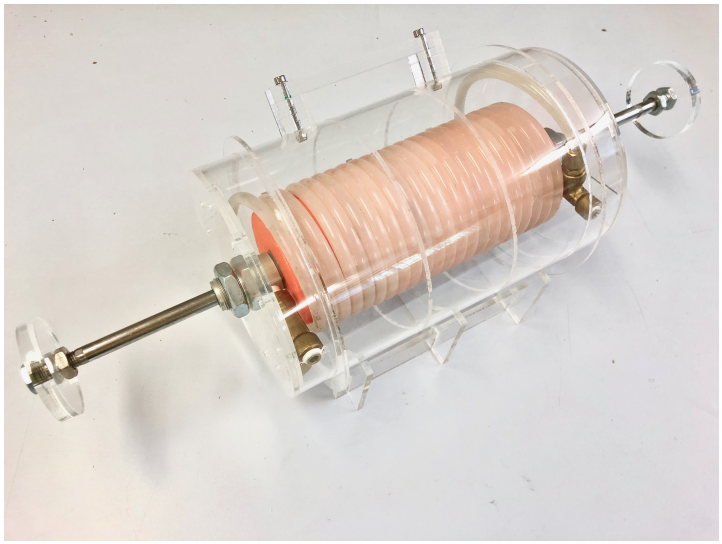

Figure 5.4: The compact helical-tube fluid inerter prototype built at the University of Bristol.

Moreover, the dimension and structure of such prototype show the potential of incorporating inerter into the existing hydraulic damper, such as the two examples of conceptual realisations demonstrated in Fig 5.5 for complete suspensions with (a) a mono-tube damper and (b) a twin-tube damper, where the gas is used to compensate the volume change in damper chamber when piston moves, and the extendable channel is used to connect the damper chamber and the external channel. According to the schematics, the external tube channel could be conveniently implemented to connect the two chambers of damper without influence the original stroke or altering the overall dimension too much. This is important for the industry applications because only the vibration suppression device with similar dimensions could directly replace the existing one, such as the vehicle suspension strut. Besides, as shown in Fig 5.5(c), the equivalent network represents the series connection between the damping and inertance based on the conventional spring-damper in parallel layout, such as the strut shown in Fig. 3.2(c). The influence of adding inertance effect into the damper device will be studied in Chapter 7 using the prototype introduced in Section 5.4.

5.3.2 Meander-tube design

A new design of fluid-based inerter is proposed in this work with the aim of achieving different damping characteristics, compared with the helical-tube fluid inerter. The meander-tube fluid arrangement, as shown in Fig. 5.6(b), is designed to achieve reduced curved length for a given length and diameter of tube, while providing similar inertance. To verify the potential reduction of damping for meander-tube design, the theoretical damping of both design with equal tube length are calculated and compared to each other.

Assume the total length of tube (l) same as the helical-tube design, Fig. 5.6(a), and the

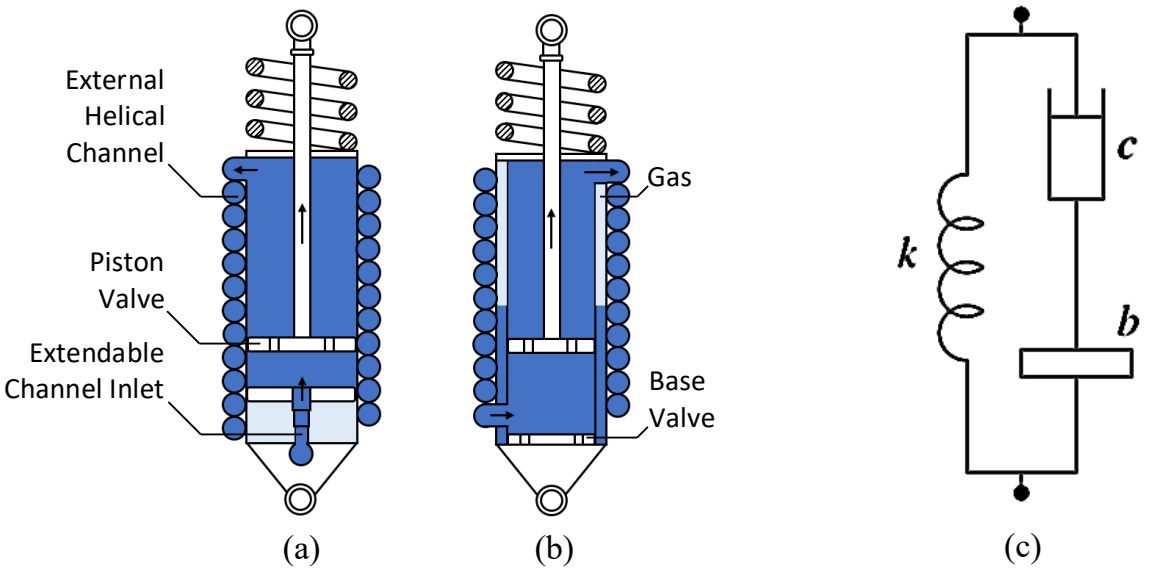

Figure 5.5: Inertial effect combined in the full suspensions with (a) a mono-tube damper, (b) a twin-tube damper, and (c) their equivalent circuit

adjacent straight tube parts are tightly compacted to each other. Therefore the bend radius of each U-bend for meander-tube design is assumed to be equal to the outer radius of tube, which is approximately $d_2/2+t$. The total length of the meander tube is $l = N_u l_u + N_s l_s$, where N_u is the number of U-bends and N_s is the number of straight tubes, l_u is the length of each U-bend and l_s is the length of each straight tube. Other parameters are selected based on the prototype specifications in Table 5.3.

Figure 5.6: Conceptual visualisation of (a) Helical tube arrangement and (b) Meander-tube arrangement.

The theoretical tube damping force (F_h) produced by the helical-tube design is calculated by $F_h = c'\Delta v$, where c' is same as Eq. (5.7). With the assumption of incompressible and laminar flow, applying the Hagen-Poieuille formula [110] for calculation of straight tube damping, the theoretical damping force (F_m) through the meander-tube channel is derived by adding the

U-bend tube damping (same as the formula for helical tube) and straight tube damping:

$$F_h = 0.03426\frac{2\rho A_1 l}{\sqrt{D_h R}}\left(\frac{A_1}{A_2}\right)^2\Delta v^2 + 17.54\frac{2\mu l A_1}{{D_h}^2}\left(\frac{A_1}{A_2}\right)\Delta v, \tag{5.9}$$

$$F_m = N_u\left[0.03426\frac{2\rho A_1 l_u}{\sqrt{D_h(\frac{d_2}{2}+t)}}\left(\frac{A_1}{A_2}\right)^2\Delta v^2 + 17.54\frac{2\mu l_u A_1}{{D_h}^2}\left(\frac{A_1}{A_2}\right)\Delta v\right] + N_s 8\pi\mu l_s\left(\frac{A_1}{A_2}\right)^2\Delta v, \tag{5.10}$$

The results of both theoretical tube damping forces for helical-tube arrangement and meander-tube arrangement are plotted in Fig. 5.7. Based on these simplified calculations, it is shown that the meander-tube design gives lower damping over the selected velocity range. Based on this result, it can be seen that with the similar dimension of device and same working fluid, the meander-tube fluid inerter has potential to achieve similar inertial effect with lower parasitic damping, compared to nominal helical-tube design.

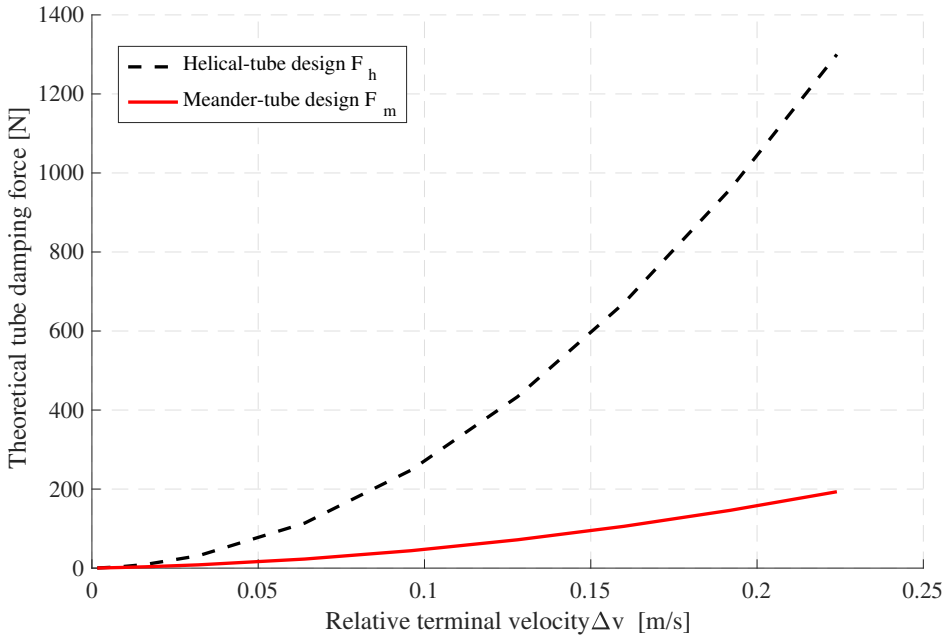

Figure 5.7: Theoretical tube damping of helical-tube and meander-tube fluid inerters.

Subsequently, the prototype of a meander-tube fluid inerter is built by the author, as shown in Fig. 5.8. However, due to the difficulties to make the U-bend tube with extremely small bend radius ($d_2/2+t$), as assumed before, the prototype can only be made with the parameters listed in Table 5.6 instead. While this tube arrangement enlarges the overall dimension of the device, the choice of tube with smaller cross-sectional area significantly increases the parasitic damping in the tube. According to the theoretical calculation of the tube damping force produced by the prototype with parameters in Table. 5.6, the peak terminal force could reach up to 6.03 kN at

velocity of 0.2 m/s, which is far beyond the safety load limit of the test rig at 4.5 kN. Therefore, the test of the meander-tube fluid inerter prototype will not be carried out in this work due to the test rig restriction.

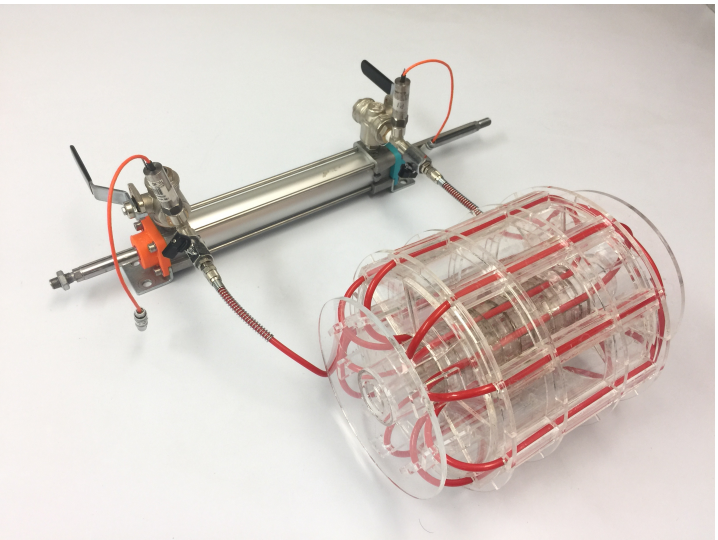

Figure 5.8: The meander-tube fluid inerter prototype built at the University of Bristol.

Table 5.6: Parameters of the meander-tube fluid inerter prototype.

Description	**Value**
Piston diameter d_1 (mm)	40
Rod diameter d_0 (mm)	16
Tube inner diameter d_2 (mm)	4
Tube bend radius R (m)	0.06
Helical tube length $l_u N_u$ (m)	2.86
Straight tube length $l_s N_s$ (m)	2.89
Inertance b (kg)	493

Both of the two presented designs in this Section 5.3 will be considered for future research as continuous work of fluid-based inerter.

5.4 Fluid-inerter integrated damping (FID) device

A prototype of the FID device is needed to investigate the influence of adding the valve damping effect into the fluid-based inerter, which can be also used to facilitate the future design of any damper device incorporating the inertance effects.

In order to obtain a generalisable model of the FID device, it is necessary to evaluate the model validity and the device properties for different parameter values. Based on the helical-tube fluid inerter prototype built in Section 5.2.2, to emulate the additional flow path through the

piston valves in Fig. 4.8, a bypass channel with a needle valve shown in Fig. 5.9(a) is adopted in parallel with the helical tube channel, to enable convenient adjustment of the valve opening. It is worth mentioning that although the FID prototype will be built based on the structure and specifications of the helical-tube fluid inerter prototype in the previous section, all the parts used (e.g. cylinder, valves, tube) are completely new and independent to the previously used ones. Therefore, the overlapped device properties (e.g. leakage damping and friction) still need to be tested individually due to the quality variation of the manufactured parts.

As before, during the tests, the strut displacement (x) is recorded by the LVDT mounted in parallel with the cylinder, and the strut force (F) is measured by the load cell which is connected between the piston rod and actuator. In addition, two pressure gauges are placed at the two intersections between the valve branch and helical tube branch. The measuring instruments are the same as those used in Section 5.2.2 with specifications shown in Table 5.4. A schematic diagram for this design is shown in Fig. 5.9(b). The ball valves 1 and 2 at the inlet and outlet of the cylinder are used to isolate the cylinder chambers from the needle valve and helical tube channels. With this setup, the cylinder properties, such as the leakage damping, can be tested separately from the external flow paths. They also allow different helical tube coil tests with various dimensions, without the need to refill the entire system. Two additional ball valves 3 and 4 are used at both ends of the helical tube channel, which can be closed when the needle valve needs to be tested separately. For clarity of other components, the ball valves are not marked in Fig. 5.9(a). The parameters of this prototype are listed in Table 5.7. Since some of the parameters will be changeable, their corresponding values will be discussed in Chapter 7. It is also worth mentioning that although the cylinder used in this FID prototype has the same parameters with the one used in Section 5.2.2, the friction due to the seals and the leakage across the piston still need to be identified since individual cylinder might has distinct properties.

Table 5.7: Parameters of the FID prototype.

Description	**Value**
Piston area $A_1{}^*$ (m^2)	1.1×10^{-3}
Tube area $A_2{}^*$ (m^2)	$(D_h/2)^2\pi$
Helix diameter D^* (m)	0.075 – 0.11 (refer to Table 7.2)
External tube length l (m)	3.88 – 11.96 (refer to Table 7.2)
Tube hydraulic diameter D_h (mm)	4 – 8 (refer to Table 7.2)
Working fluid density ρ at 30 °C ($kg \cdot m^{-3}$)	995.6
Working fluid viscosity μ at 30 °C ($Pa \cdot s$)	7.98×10^{-4}

*shown in Fig. 5.9(c)

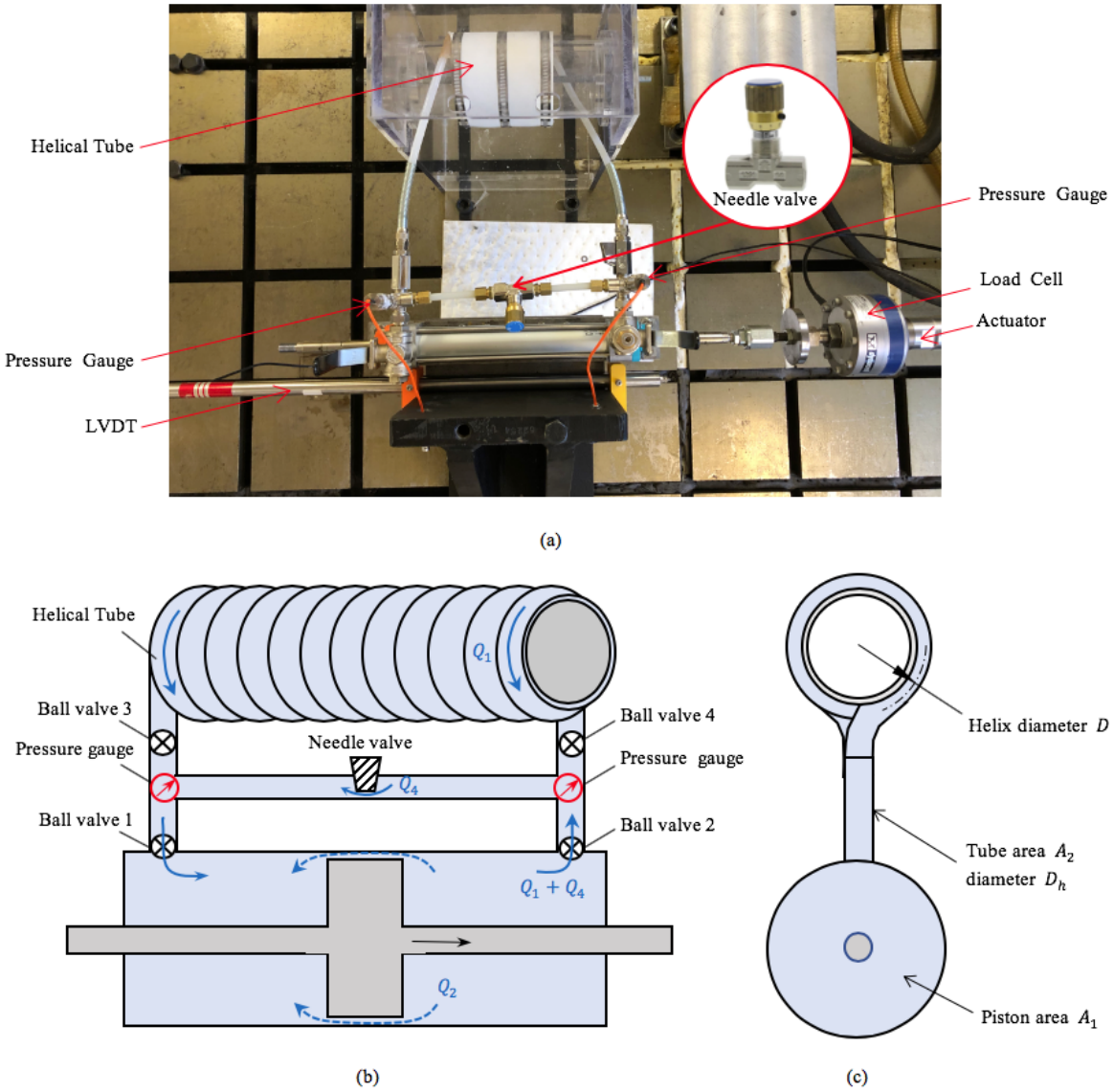

Figure 5.9: The FID test rig (a) with adopted needle valve setup (shown in a red circle inset), and corresponding schematic diagram with (b) the elevation and (c) the end view of the device.

5.5 Calibrations

The calibration of the measurement instruments are the basic guarantee of the accurate data collection during the experimental tests. While some of them can be restored from the calibration settings, others need to be manually calibrated.

5.5.1 Load cell

The load cell used in the test rig has stored was calibrated by the engineers from INSTRON. Before each test, the RS LabSite-modulogic software is used to restore the calibration settings to

ensure the accurate recording of the load values in the tests.

5.5.2 LVDT

The Linear Variable Differential Transformer (LVDT) is used to record the displacements of the prototype moving rod. The voltage bandwidth of ±10 V is set for calibration of the LVDT with the displacement range of ±150 mm. According to the reference micrometer (measurement), the displacement (x) of LVDT is incrementally increased from -150 mm to 150 mm with increment of 10 mm, and the corresponding ouput voltage (V) was recorded. The results are plotted as the red circles in Fig. 5.10 and the best-fit linear relationship was obtained as $V = -0.065x + 0.1$, based on the collected data. In order to verify the calibrated result, the calibration is repeated reversely to decrease the displacement from 150 mm to -150 mm with the same increment, and the recorded voltage are plotted by the blue crosses. It can be seen from Fig, 5.10, the calibrated relationship is satisfactory for both directions without observation of any obvious backlash effect.

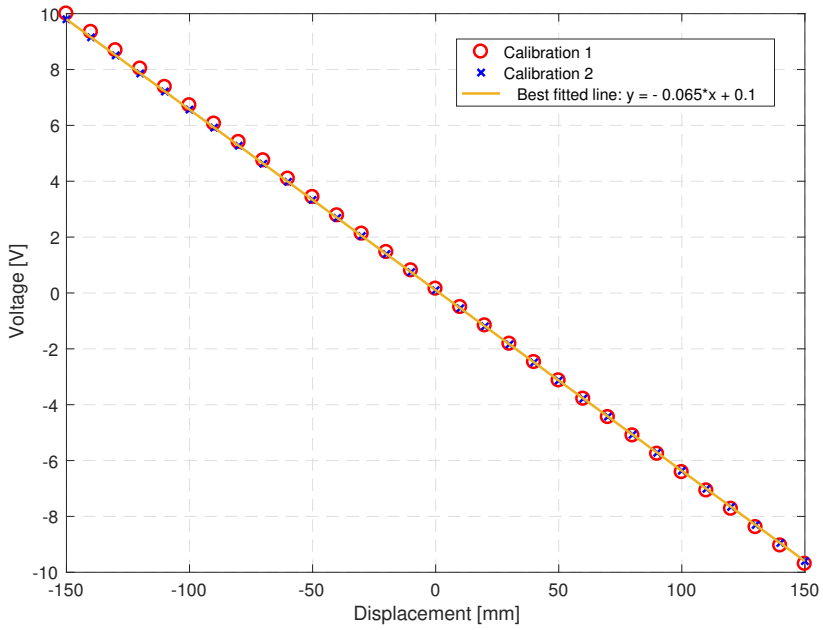

Figure 5.10: The calibration curve for LVDT.

5.5.3 Pressure Gauge

The two pressure gauges are used to measure the pressure difference across the external tube. Following the specification of the transducer, the linear relationship is set between the voltage signal of 0 to 10 V and pressure of 0 to 15 Bar (with minor graduation of 0.001 Bar). To validate this relationship and the accuracy, the pressure gauge is inserted into a water tank as shown in

Fig. 5.11. The corresponding pressure p at various heights of water h are recorded and plotted in Fig. 5.12 for both transducers. It is also worth mentioning that since only the instantaneous pressure difference Δp across the flow branch is needed during the tests, the transducers were not calibrated to show the absolute pressure values, and the initial pressure is always set to 0 Bar before the test. According to the formula of $p = \rho g h$, the relationship between the recorded pressure and the height of water should be linear as demonstrated by the two best-fit lines based on the collected data. Furthermore, the differences Δp between the recorded pressures at two heights of water (h = 135 and 185 mm for pressure gauge 1, h = 54 and 135 mm for pressure gauge 2) are compared with the calculated actual pressure differences as shown in Table 5.8. The results validate the accuracy of the pressure gauges.

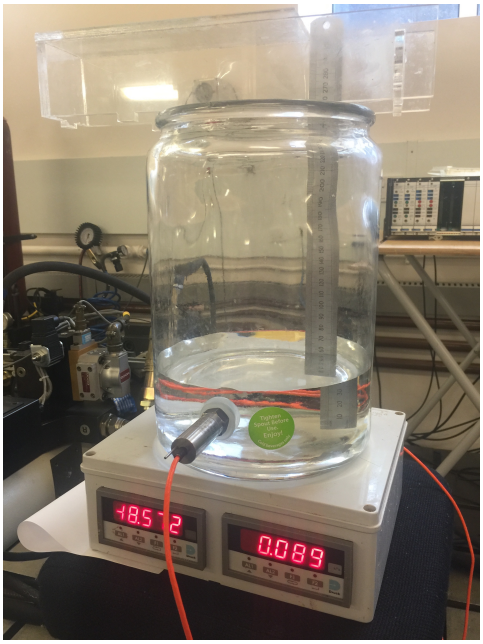

Figure 5.11: The setup for calibration of the pressure gauge.

Table 5.8: The calibration results of the pressure difference correspond to the height difference of water.

	Pressure Gauges 1	**Pressure Gauges 2**
Recorded pressure difference Δp (Bar)	0.005	0.007
Actual pressure difference Δp (Bar)	0.005	0.007

5.6 Summary

A prototype and test rig of a helical-tube fluid inerter are developed with systematically selected design parameters, which will be used for experimental testing to develop the model of fluid-based

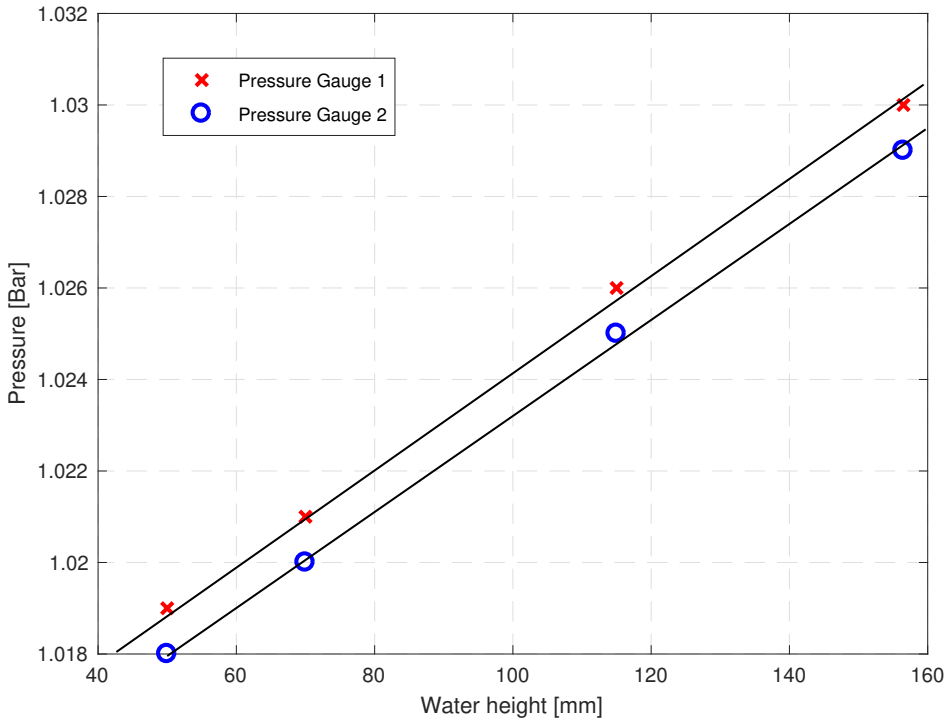

Figure 5.12: The calibration of the pressure gauges.

inerter in Chapter 6. For demonstration of the practical design, an alternative prototype of the helical-tube fluid inerter is built in small scale. The conceptual designs of incorporating such device into the the existing damper are also discussed. In the meantime, an new design with meander tube arrangement is theoretically studied with respect to the parasitic damping, and the corresponding prototype is made for future tests. Subsequently, the FID device is realised by modifying the helical-tube fluid inerter prototype by adding an additional flow path with adjustable needle valve, which will be used for model development of FID device in Chapter 7. Finally, to prepare for the experimental testing, the measuring instruments in the test rig are calibrated through respective approaches (e.g. micrometer-based calibration exercise) based on their own settings.

CHAPTER 6

FLUID-BASED INERTER MODEL DEVELOPMENT

6.1 Overview

In this chapter, based on the fluid-based inerter model constructed in Section 4.3, the friction, stiffness and various damping effects are identified for the helical-tube fluid inerter prototype built in Section 5.2.2, by static and dynamic testing. Then the dynamic response of the established full model at different amplitudes and frequencies are compared with the corresponding experimental testing data for model verification. The remaining discrepancies for the modelling and verification are also analysed.

6.2 Friction and damping effects identification

In this section, the friction and damping effects of the fluid inerter prototype are experimentally tested and then identified. Constant velocity tests are carried out to produce the steady-state responses. Each test uses a triangular wave of displacement to excite the free end of the prototype, producing constant strut velocities in both directions. Note that the transient responses can also be used for parameter identification, and there could be unsteady flows occurs during the transient stage, such as the oscillating flow in the tube [111–114] when changing of flow direction frequently. In this work, it is decided to focus on the steady-state response with the purpose to separate the damping effects identification from the inertial and stiffness effects for steady flow.

Assuming a constant velocity Δv_c and applying the final value theorem [115] to Eq. (4.19), the steady-state response can be described as:

$$\begin{aligned}\lim_{t\to\infty} F(t) &= \lim_{s\to 0} s\hat{F}(s) \\ &= \lim_{s\to 0} s \times \frac{1}{{c_{s,2}}^{-1} + \left(c_{h,1} + c_{io,1} + bs\right)^{-1} + k_{c,3}^{-1} s} \times \frac{\Delta\hat{v}_c}{s} \\ &= \frac{1}{{c_{s,2}}^{-1} + \left(c_{h,1} + c_{io,1}\right)^{-1}} \times \Delta\hat{v}_c.\end{aligned} \tag{6.1}$$

Note that Eq. (6.1) shows that the stiffness and inertance terms will not affect the steady-state response. Using relevant network synthesis techniques, such as those introduced in [100], the network shown in Fig. 6.1 (excluding the friction term) can be obtained. Since the friction effects are mainly caused by the contact between the piston rod and cylinder seals, the additional friction term is considered in parallel with all other damping terms. The symbol ' ↗ ' included in Fig. 6.1 represents the possible nonlinearities in each damping term.

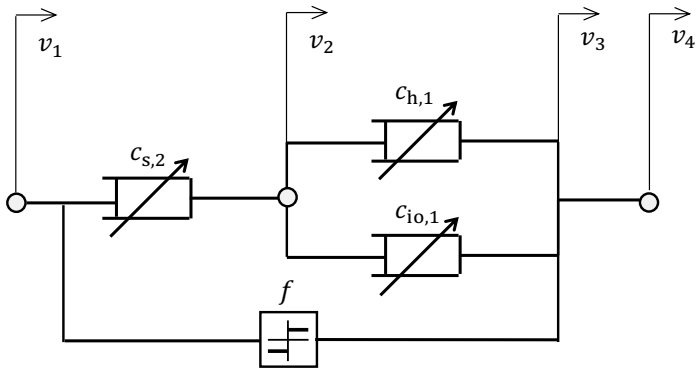

Figure 6.1: The equivalent mechanical network of a typical helical-tube fluid inerter during steady-state response, with a friction term included.

6.2.1 Friction and hydraulic force testing

An amplitude of 40 mm is chosen for the constant velocity tests, and the tests are carried out at strut velocities from 1.6×10^{-5} m/s to 0.224 m/s. The upper limit of the tested velocities is set by the maximum allowed force (4.5 kN) that can be applied to the strut terminal. During the tests, three sets of experimental data are collected. These include the strut displacements (x) by the LVDT, the strut forces (F) by the load cell, and the internal pressures at each end of the helical tube (p_1, p_2) by the pressure gauges, as illustrated in Fig. 4.5(a).

To identify the steady-state strut force at each tested velocity, the method of Least Absolute Residuals (LAR) [116] is used to fit a curve that minimises the sum of the absolute residuals, rather than the squares of the residuals. In this way, any extreme values in the transient response have less influence on the identified results. For example, in Fig. 6.2, the experimental strut force at strut velocity of 0.096 m/s has been fitted by a square wave with an amplitude of 0.296 kN,

which is used as the identified value of the steady-state strut force at this tested velocity. The oscillations shown in Fig. 6.2 is due to the stiffness and inertance effects after each change of moving direction. It is also worth mentioning that there is an initial load offset -0.0366 kN, which has been removed during post-processing of the load cell readings. At extremely low velocity, the damping forces can be ignored as they are usually proportional to the (square of) flow velocities, the friction dominates the response. Therefore, the steady-state strut force at velocity equals 1.6×10^{-5} m/s is used to identify the friction force f, which equals approximately 45 N. It is assumed that the friction of the tested prototype is constant during all the tests of this prototype.

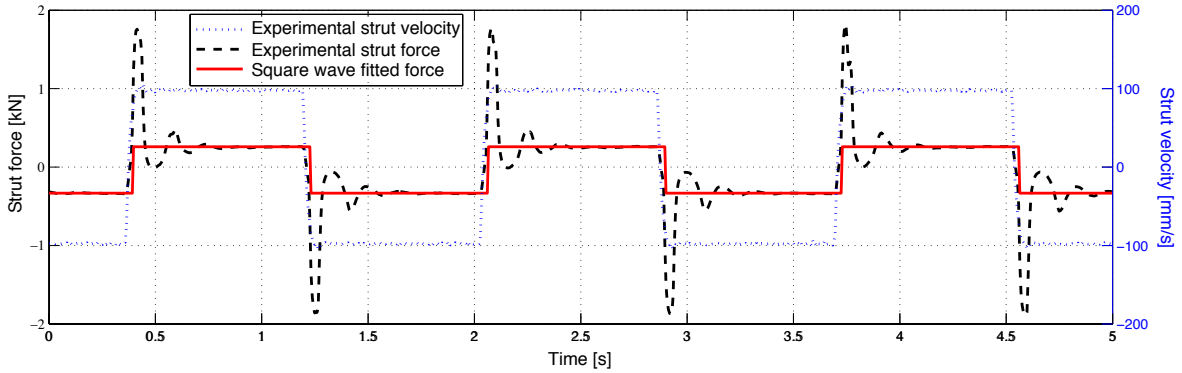

Figure 6.2: Square wave fitting to a triangular wave test at the constant strut velocity of 0.096 m/s.

The difference between the two readings of the pressure gauges represents the pressure drop across the helical tube ($\Delta p_{h,1}$), which is equal to the sum of pressure drops caused by the hydraulic resistance ($\Delta p_{hR,1}$) and the hydraulic inertance ($\Delta p_{hI,1}$). One example is shown in Fig. 6.3, at a strut velocity of 0.096 m/s, where the steady-state pressure drop is identified to be approximately 210,000 Pa. For the steady-state response, it can be assumed that $\Delta p_{hR,1} = 210,000$ Pa since the pressure drop is purely caused by the hydraulic resistance. The initial values of the pressure gauges, which correspond to atmospheric pressure, are set to 0 Pa. As a result, the pressure gauges during the experiments record both positive and negative values of the pressures.

The results of the damping tests at each tested strut velocity (Δv) are summarised in Fig. 6.4, with the red curve representing the hydraulic force (F_H) introduced in Section 4.3 (Fig. 4.7) and the blue curve standing for the helical tube damping force due to the hydraulic resistance across the helical tube ($F_{hR,1}$). The hydraulic force is calculated by subtracting the friction (f) from the strut force (F) recorded by the load cell. The helical tube damping force is derived from the formula $F_{hR,1} = A_1 \Delta p_{hR,1}$, where $\Delta p_{hR,1}$ is the pressure drop across the pressure sensors. It can be seen that the nonlinear damping properties are characterised by rapid damping force increase with the strut velocity. Furthermore, the hydraulic force F_H is shown to be dominated by the helical tube damping as evidenced by the very small difference between these two lines. The observed discrepancy between these two values can be explained by the presence of tube inlet/outlet damping and potential leakage damping across the piston, both of which will be

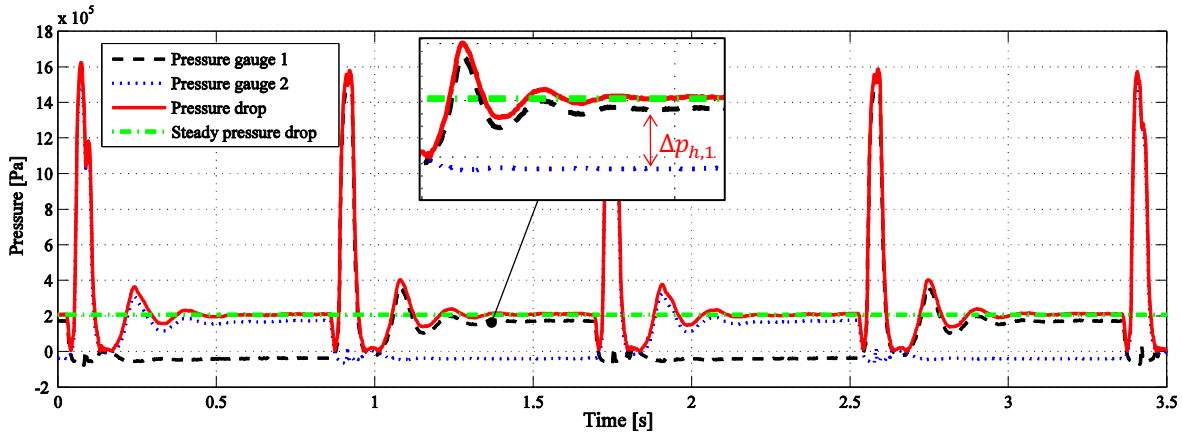

Figure 6.3: The pressure drop across the helical tube at a strut velocity of 0.096 m/s.

discussed in detail in the remaining part of this section.

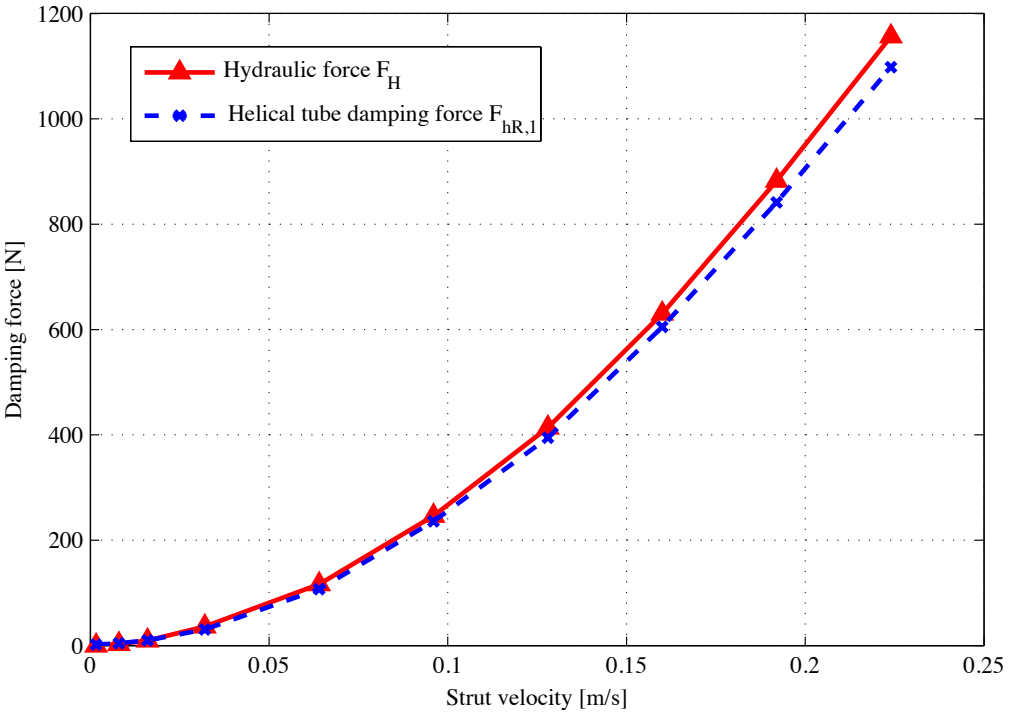

Figure 6.4: Experimental hydraulic force and helical tube damping force versus strut velocity.

6.2.2 Piston leakage damping identification

The damping caused by the potential flow leakage between the piston and the cylinder wall could influence the flow distribution inside the inerter. To accurately predict this damping effect, the

hydraulic resistance due to the flow restriction of piston leakage ($R_{s,2}$) needs to be identified.

In order to test the leakage damping effect independently, both valves at the inlet/outlet of the cylinder are closed during the test. This ensures that the flow between the two cylinder chambers can only pass through the leakage gap across the piston. The hydraulic network for this scenario can be constructed as shown in Fig. 6.5 (a). Compared with Fig. 4.6, the flow paths with the flow rate of Q_2 passes through the potential leakage gap and Q_1 does not exist due to the blocked helical tube. In the meantime, Q_3 still exists, because of the presence of the compressibility of the fluid in the cylinder chamber. Following similar procedure discussed in Section 4.3, the equivalent mechanical network can be obtained, as shown in Fig. 6.5 (b).

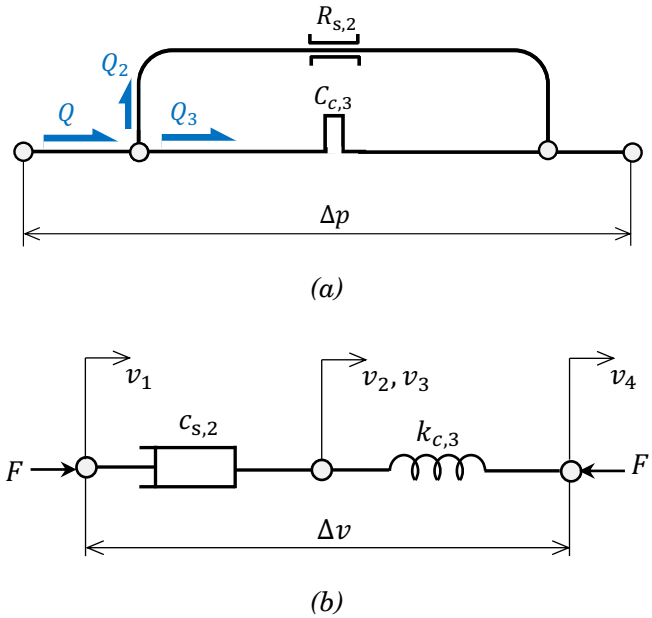

Figure 6.5: A fluid-based inerter's (a) hydraulic network, and (b) equivalent mechanical network, with both valves at the inlet/outlet of the cylinder closed.

Since small leakage gap will lead to large leakage damping force ($F_{s,2}$), the lowest strut velocity of 1.6×10^{-5} m/s is applied to carry out the constant strut velocity test. The recorded strut force is shown as the black curve in Fig. 6.6. Note that the strut force in the plot includes the extra friction term, which can be seen from the small strut force when the strut displacement equals zero. It can be observed that the strut force continuously increases until the safety load limit (4.5 kN) is triggered, which leads to the sudden switch off of the actuator and load cell before the strut displacement reaches 6 mm.

If the leakage damping force dominates the strut force, the initial transient response would be followed by a steady response. However, in Fig. 6.6, no such trend is observed, which means that the effect of leakage damping is very limited. Given the fact that all the tests of this prototype are carried out within the same safety load limit, it is assumed there is no leakage damping, namely $R_{s,2} = c_{s,2} = \infty$, for the rest of this chapter.

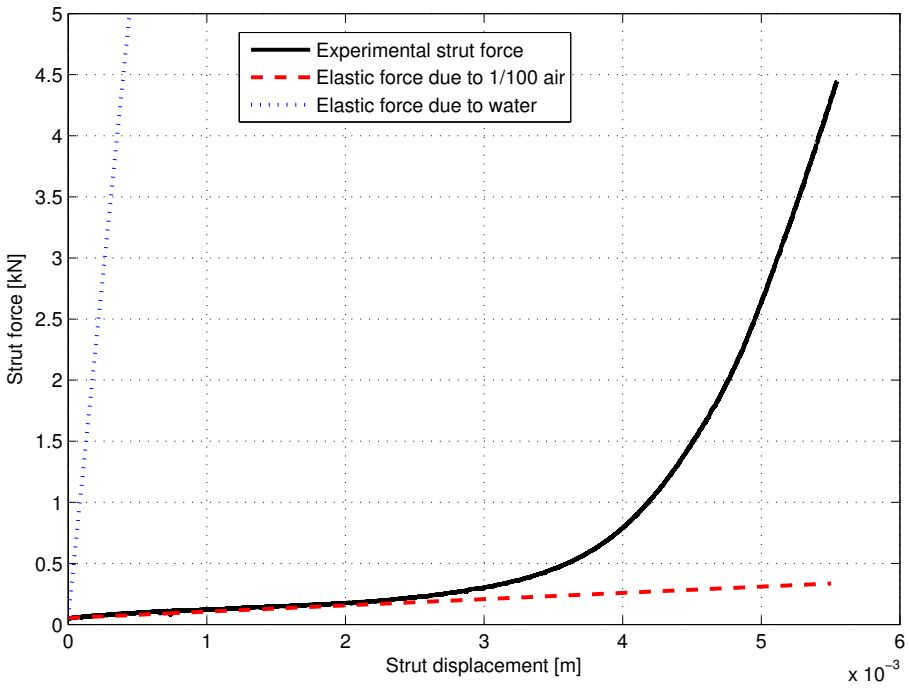

Figure 6.6: The triangular wave test with constant velocity 1.6×10^{-5} m/s.

Furthermore, according to the steep increase of the strut force versus displacement curve in Fig. 6.6, it can be seen that the elastic force dominates the strut force, thus the corresponding pressure difference between the two cylinder chambers (Δp) is equal to the pressure drop ($\Delta p_{c,3}$) caused by the fluid compressibility. Consider the bulk modulus defined in [102],

$$B = V_1 \frac{\Delta p_1}{\Delta V} = V_2 \frac{-\Delta p_2}{-\Delta V}, \tag{6.2}$$

where B is the bulk modulus of fluid, ΔV is the change in volume, Δp_1 (-Δp_2) are the pressure changes in the left (right) cylinder chamber, and V_1 (V_2) are the volume of fluid in the left (right) cylinder chamber. The total volume of the cylinder chamber is denoted as V, which equals $V_1 + V_2$. Assuming the piston is placed in the centre position of the cylinder chamber, then $V_1 = V_2 = V/2$. Using Eq. (6.2) and $\Delta V = A_1 \Delta x$ (where Δx is the strut displacement), the elastic force due to the hydraulic compliance can then be expressed as:

$$F_{c,3} = A_1 \Delta p = A_1(\Delta p_1 + \Delta p_2) = B \frac{4{A_1}^2}{V} \Delta x = k_{c,3} \Delta x_{c,3}, \tag{6.3}$$

where the relative displacement across the fluid spring ($\Delta x_{c,3}$) is equal to the strut displacement (Δx) due to the strut force is dominated by elastic force. Hence, the fluid stiffness ($k_{c,3}$) is shown to be proportional to the bulk modulus of fluid (B),

$$k_{c,3} = \frac{4{A_1}^2}{V}B. \tag{6.4}$$

The nominal bulk modulus of water $B_w = 2.2 \times 10^9\,\mathrm{N/m^2}$, and the value for air $B_a = 1.01 \times 10^5\,\mathrm{N/m^2}$. Compared with the experimental result, using Eq. (6.3), the corresponding elastic forces are plotted in Fig. 6.6 when the cylinder is full of water (blue dotted line), and when air occupies 1/100 of the cylinder chamber volume (red dashed line). The bulk modulus of the later case is calculated following the example from [102, p. 17]:

$$\frac{1}{B_e} = \frac{1}{B_w} + \frac{V_a}{V}\frac{1}{B_a}. \tag{6.5}$$

where B_e is the effective bulk modulus and V_a is the volume of air. The strut displacement required to completely compress the air can be estimated by $V_a/A_1 = L/100 = 2.17 \times 10^{-3}$ m, where $L = 217$ mm is the chamber length as shown in Table 5.2. As it can be observed in Fig. 6.6, this estimated strut displacement has good agreement with the turning point displacement of the strut force. The consistency between the experimental strut force and the elastic force for the 1/100 air occupation case during the initial 2 mm of the strut displacement gives the evidence of the presence of air inside the cylinder.

6.2.3 Helical tube damping verification

From Fig. 6.4, it can be seen that the damping due to the hydraulic resistance inside the helical tube is the dominant damping effect. Its nonlinearities need to be investigated for an accurate theoretical modelling. Firstly, to determine whether the flow is laminar or turbulent, Reynolds number (Re) of the flow in the helical tube is calculated using the formula [117]:

$$Re = \frac{\rho D_h}{\mu}u = \frac{\rho D_h}{\mu}\frac{Q_1}{A_2}, \tag{6.6}$$

where u is the mean flow velocity in the tube (thus $Q_1 = A_2 u$) and other variables have been defined in Table 5.3. According to the dimensions of the helical tube specified in Table 5.3, the curvature ratio λ of the helical tube is:

$$\lambda = \frac{D_h}{2R} = 0.072. \tag{6.7}$$

The critical Reynolds number (Re_c), which represents the approximate boundary between the laminar and turbulent flow for $\lambda < 0.1$ is given by [118]:

$$Re_c = 2100(1 + 12\lambda^{0.5}) = 8875. \tag{6.8}$$

After substituting $Re_c = 8875$ into Eq. (6.6), the boundary for laminar flow to become turbulent is at the flow rate of 4.19×10^{-5} m^3/s, which corresponds to strut velocity of 0.038 m/s (assuming with no leakage flow). The tested flow rates in the helical tube are in the range from 1.7×10^{-6} m^3/s to 2.3×10^{-4} m^3/s. Therefore, most of the tested cases generate turbulent flow in the helical tube, the model based on the turbulent flow condition is required to fit the experimental results. Various empirical models based on experimental data were developed to characterise the pressure drop due to the hydraulic resistance across helical-coiled tubes ($\Delta p_{hR,1}$). Most of these studies are based on the correlation between the Fanning friction factor (f_c) and Reynolds number, which is determined for specific fluid properties and tube characteristics. Assuming the tube is long enough to ignore the end effect, and using the notation introduced in Table 5.3, the equation for the pressure drop ($\Delta p'_{hR,1}$) due to hydraulic resistance of the uniform flow in circular tubes can be written as [117]:

$$\Delta p'_{hR,1} = f_c \frac{2\rho l}{D_h} \left(\frac{Q_1}{A_2} \right)^2. \tag{6.9}$$

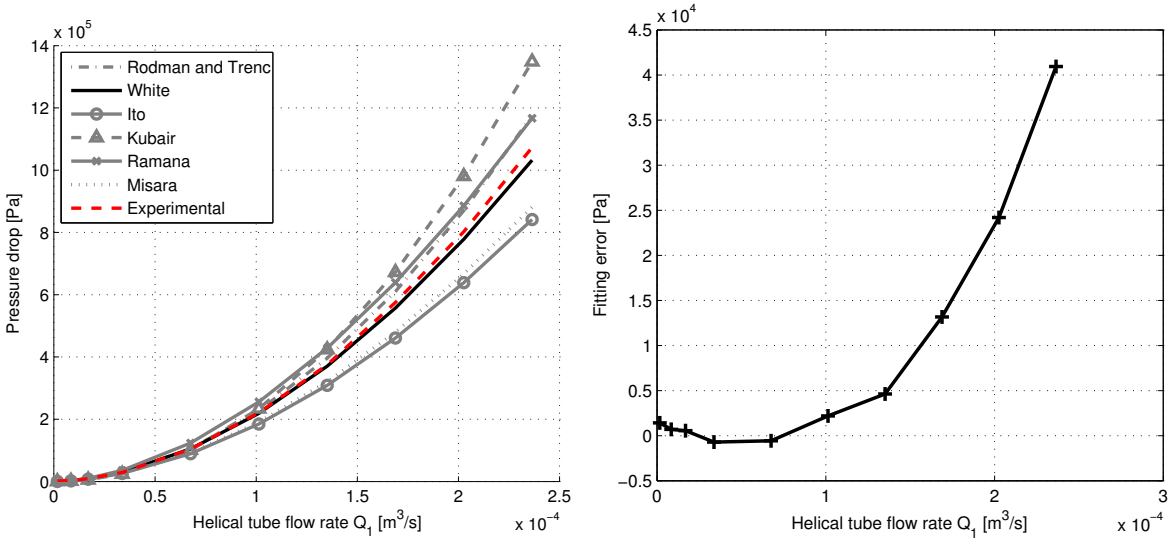

(a) *(b)*

Figure 6.7: (a) Comparison of the theoretical and experimental helical tube pressure drop versus flow rate, and (b) the fitting error between the chosen model (White) and the experimental data.

The Fanning friction factor is calculated based on [119, 120], where 6 different models are available for the tested flow with the certain Reynolds number and curvature ratio. To select the most appropriate model for this study, the theoretical pressure drop across the helical tube ($\Delta p'_{hR,1}$) is calculated for each model using Eq. (6.9). The predicted pressure drops versus helical tube flow rate Q_1 (which equals to the total flow rate Q when no leakage is assumed) are plotted in Fig. 6.7 (a). These pressures are compared with the experimentally recorded $\Delta p_{hR,1}$ (red dashed

line). It can be observed that different levels of discrepancies exist between the models and experiment. These discrepancies could originate from different test conditions such as dimension or material of the tubes used for the experiments to derive the corresponding f_c. Among all of the formula, the model introduced by White [121] matches the measured experimental results the best. This is denoted by the solid line in Fig. 6.7 (a) with the corresponding values of the fitting error shown in Fig. 6.7 (b). Therefore, this model of the Fanning friction factor is used here for theoretical modelling of the helical tube pressure drop due to hydraulic resistance. The model can be expressed as:

$$f_c = 0.08Re^{-1/4} + 0.012\sqrt{\frac{D_h}{2R}}. \tag{6.10}$$

Based on the assumed linear relation between the pressure drop and the flow rate through the helical tube $\Delta p_{hR,1} = R_{h,1}Q_1$, the hydraulic resistance $R_{h,1}$ is identified from Eq. (6.9), to be a Q_1-dependent coefficient,

$$R_{h,1}(Q_1) = f_c \frac{2\rho l}{D_h {A_2}^2} Q_1. \tag{6.11}$$

It is noted that the White's model could be inaccurate to fit the dynamic response since the test velocity will not be constant.

Apart from the main helical part of the tube, the pressure drop caused by the flow restrictions at the inlet and outlet of the tube ($\Delta p_{io,1}$) also needs to be considered. One commonly used empirical formula for the inlet/outlet pressure drop [122] is:

$$\Delta p_{io,1} = \Delta p_{in} + \Delta p_{out} = 0.5\frac{\rho u^2}{2} + \frac{\rho u^2}{2} = 0.75\rho\left(\frac{Q_1}{A_2}\right)^2. \tag{6.12}$$

Therefore, based on the linear relationship between the pressure and flow assumed in Section 4.3, the hydraulic resistance due to the inlet/outlet of the tube is expressed as a Q_1-dependent coefficient:

$$R_{io,1}(Q_1) = \frac{\Delta p_{io,1}}{Q_1} = \frac{0.75\rho}{{A_2}^2} Q_1. \tag{6.13}$$

For the following construction of the model in the mechanical domain, the equivalent mechanical damping coefficients $c_{h,1}$ and $c_{io,1}$ are derived using Eq. (6.11), Eq. (6.13), Eq. (4.20) and their respective relation with $R_{h,1}$ and $R_{io,1}$ defined in Section 4.3:

$$c_{h,1} = R_{h,1}{A_1}^2 = f_c \frac{2\rho l A_1}{D_h}\left(\frac{A_1}{A_2}\right)^2 \Delta v_{h,1}, \tag{6.14}$$

$$c_{io,1} = R_{io,1}{A_1}^2 = 0.75\rho A_1\left(\frac{A_1}{A_2}\right)^2 \Delta v_{io,1}. \tag{6.15}$$

These two equations will be used to represent the properties of damping in the theoretical model of the helical-tube fluid inerter prototype. It is also worth mentioning that although Eqs. (6.11), (6.13), (6.14) and (6.15) are in linear forms to keep consistent with the linear assumption made in Section 4.3, the relationships between flow rate (Q_1,)/velocities ($\Delta v_{h,1}, \Delta v_{io,1}$) with hydraulic resistance ($R_{h,1}, R_{io,1}$)/mechanical damping ($c_{h,1}, c_{io,1}$) are in fact nonlinear.

6.3 Dynamic model identification

In this section, two models for the helical-tube fluid inerter prototype are established. The inertance is calculated based on the physical properties of the device, and the fluid stiffness is identified based on the comparison between the theoretical models and experimental testing results. Analysis of the remaining discrepancies is also provided.

6.3.1 Full theoretical models of the prototype

Based on the equivalent mechanical network in Fig. 4.7, the refined mechanical network of the prototype is shown in Fig. 6.8. This network includes the additional friction element due to the seals, the value of which has been identified to be 45 N in Section 6.2.1. The tube inlet/outlet damping ($c_{io,1}$) is represented as a velocity dependent term, using the nonlinear property described in Eq. (6.15). The leakage damping element ($c_{s,2}$) is treated as infinity based on the analysis in Section 6.2.2. The nonlinear helical tube damping ($c_{h,1}$) can be represented by either theoretical formula or experimental data set. Thereby, two models are established using the network shown in Fig. 6.8:

- **Model 1** uses the theoretical formula Eq. (6.14) for $c_{h,1}$ to calculate the damping force $F_{hR,1} = c_{h,1}\Delta v_{h,1}$. This type of model is able to reveal the influence of individual parameters of the damping force. It is also able to accommodate parameter values' changes within a certain range.

- **Model 2** uses a lookup table of the experimental data shown in Fig. 6.4 to find the value of $F_{hR,1}$ (the strut velocity in Fig. 6.4 is equivalent to the relative velocity across the helical tube damping ($\Delta v_{h,1} = v_3 - v_2$) in Fig. 6.8 due to the fact that $c_{s,2}$ from Fig. 4.7 can be treated as infinity). This model is expected to be more accurate because it includes properties that might not be captured by the theoretical formulas, such as Eq. (6.14).

To complete the model, only the inertance and fluid stiffness need to be identified. The inertance can be calculated here theoretically by using Eq. (5.6), which is based on the principle of

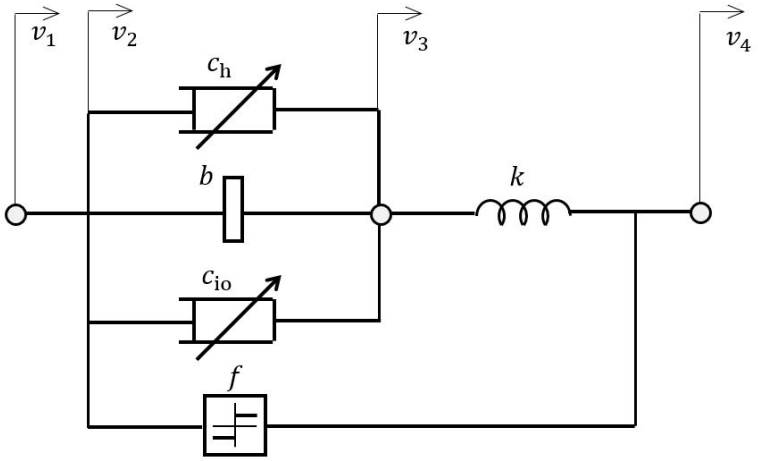

Figure 6.8: The refined mechanical network of the helical-tube fluid inerter prototype.

energy conservation with appropriate assumptions [4]. However, this work intends to investigate the connection between mechanical terminal behaviour (force and velocity) and the hydraulic variables. Therefore, the inertance is alternatively calculated based on Newton's second law. Under this law, the flow conditions in the tube can be characterised by the following equation:

$$m\dot{u} = F_{hI,1} \tag{6.16}$$

where $m = A_2 l \rho$ is the mass of fluid in the helical tube, and u is the flow velocity introduced in Section 6.2.3. Considering that $\Delta p_{hI,1}$ is the pressure drop corresponding to hydraulic inertance, the hydraulic force $F_{hI,1} = \Delta p_{hI,1} A_2$. Then Eq. (6.16) can be written as:

$$(A_2 l \rho)\frac{\dot{Q}_1}{A_2} = \Delta p_{hI,1} A_2. \tag{6.17}$$

Noting that $\Delta p_{hI,1} = I_{h,1}\dot{Q}_1$ ([106]), it can be seen from Eq. (6.17), that $I_{h,1} = l\rho/A_2$, which is consistent with previous works [104, 123]. Similar to [4], assuming the inertance of the fluid inside the cylinder chamber is negligible due to the relatively small flow velocity and ignoring the influence of the temperature and unexpected air inside the tube, following the transformation from the hydraulic inertance to the mechanical inertance described in Section 4.3, the parameter b can be expressed as:

$$b = I_{h,1} {A_1}^2 = \frac{l\rho}{A_2} {A_1}^2. \tag{6.18}$$

This value can be calculated for the prototype specifications in Table 5.3. From this, the mechanical inertance is 219 kg, which will be used for both Model 1 and Model 2.

In summary, the refined network in Fig. 6.8, Eq. (6.14) and Eq. (6.10) are used to model the helical tube damping ($c_{h,1}$) [121] for Model 1 (Model 2 uses the experimental data in Fig. 6.4), Eq. (6.15) is adopted to represent the tube inlet/outlet damping ($c_{io,1}$) [122], and the inertance is calculated by Eq. (6.18). The friction equals 45 N based on experimental testing introduced in Section 6.2. The fluid stiffness $k_{c,3}$ will be identified in Section 6.3.2.

6.3.2 Fluid stiffness identification

With the calculated inertance value, the fluid stiffness ($k_{c,3}$) is the only unknown parameter in the theoretical model. Similar to [4], its value is identified using the experimental data obtained from dynamic tests with sinusoidal excitations. Two Simulink [124] models are constructed corresponding to Model 1 and Model 2 as shown in Appendix A.1. To increase the accuracy of identification, the tests are carried out over a wide frequency range. However, the upper limits of the tested frequencies for each amplitude are restricted by the maximum allowed force that can be applied to the cylinder (4.5 kN). The test ranges are shown in Table 6.1. Amplitudes of 5 mm, 10 mm and 20 mm are chosen according to the potential strut strokes in most relevant applications. The frequency range covers from 0.2 Hz up to 7 Hz. The experiment with the amplitude of 1 mm is more focused on higher frequency behaviour, for which the frequencies from 1 Hz to 13 Hz are tested. The selected frequency and amplitude range of experiment tests are of interest to the vibration suppression problems in many dynamic systems, such as road vehicles [31], multi-storey buildings [23], and railway vehicles [17].

Table 6.1: Test range of amplitudes and frequencies.

Amplitude (mm)	1	5	10	20
Frequency (Hz)	1-13	0.2-7	0.2-4	0.2-2
Peak strut velocity (m/s)	0.004-0.052	0.004-0.14	0.008-0.16	0.016-0.16

With experimental data of strut displacement (Δx) and force (F), various nonparametric methods (e.g. those listed in [125]) can be adopted to identify the dynamic properties. The correlation method [126, p. 143] is chosen in this work to identify the transfer function from the relative terminal velocity Δv to the strut force F at each tested frequency. This method assumes the system to be linear at each frequency point. The detailed derivation of this method is given in Appendix A.2. Based on the magnitude and phase of the network's dynamic responses across the tested frequency range, a metric J is introduced to quantify the percentage discrepancy between the experimental and theoretical results [127]:

$$J = \sum_{i=1}^{n_f} \frac{\left|Y(k_{c,3}, j\omega_i) - E(j\omega_i)\right|}{n_f \left|E(j\omega_i)\right|}, \tag{6.19}$$

where n_f is the number of frequency points (n_f= 11, 11, 8 and 6 for amplitude 1, 5, 10 and 20 mm), $E(j\omega_i)$ is the experimental admittance function and $Y(k_{c,3}, j\omega_i)$ is the theoretically calculated admittance function based on either Model 1 or Model 2 (introduced in Section 6.3.1). The values of J for both models with each excitation amplitude are plotted in Fig. 6.9 as a function of the fluid stiffness $k_{c,3}$.

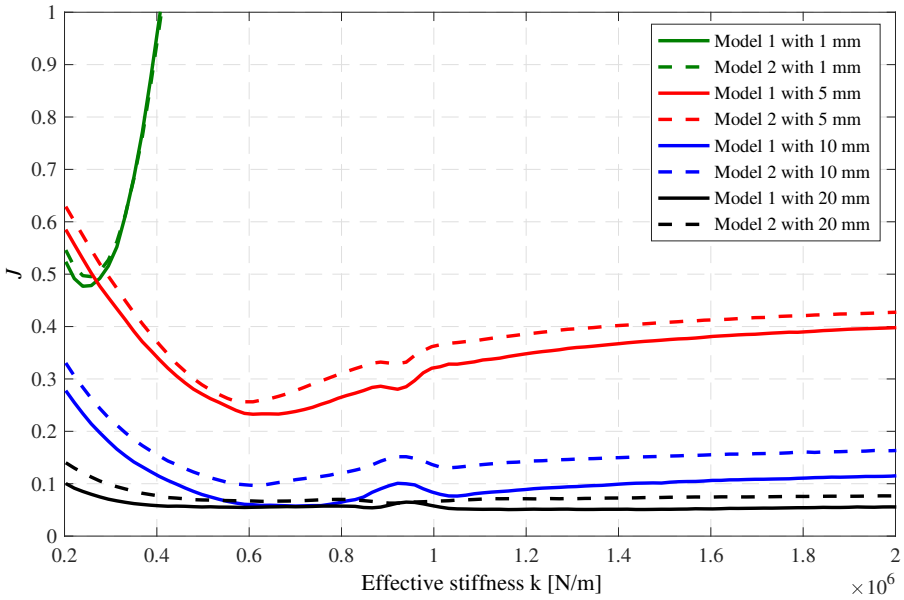

Figure 6.9: The J value versus the fluid stiffness $k_{c,3}$ with amplitude 1 mm, 5 mm, 10 mm and 20 mm for Model 1 and Model 2.

The identified $k_{c,3}$ values for Model 1 and Model 2 are determined based on the minimum values of J for each amplitude with the optimisation approach given in Appendix A.3, and the optimum $k_{c,3}$ are listed in Table 6.2. The identified fluid stiffness lies in the range of 0.24 – 1.31 MN/m. It can be seen that there is a significant difference between these values and the theoretical stiffness of the used fluid (approximate 40 MN/m for water at 30 °C). Similar observations are indicated in [4]. This discrepancy can be explained by the flexibility of the prototype's joints and the presence of air in the cylinder [102, 128]. The bulk modulus is highly sensitive to the pressure and the volume of the unexpected air in a certain volume of fluid [129], which could significantly reduce the fluid stiffness $k_{c,3}$. One example in [102, p. 17] indicates that only 1% of the trapped air could cause 75% reduction of the original bulk modulus of the fluid.

It is also noted from Fig. 6.9 and Table 6.2 that the values of the identified fluid stiffness grow with the testing amplitude. This phenomenon can be explained as follows. From Eq. (6.4), it can be seen that $k_{c,3}$ and B has a linear relation. It has been shown that higher pressures lead to bigger bulk modulus for liquid-gas mixture [102, 130]. Based on Table 6.1, it can be seen that larger amplitude tests typically experience higher strut velocities, which corresponds to high

pressures in the cylinder. Similar trend can be also observed from Fig. 6.6, where the gradient of the strut force versus displacement curve increases with the strut displacement.

Table 6.2: Identified values of fluid stiffness for Model 1 and Model 2.

Amplitude (mm)		1	5	10	20
Identified fluid stiffness (MN/m)	Model 1	0.24	0.64	0.70	1.31
	Model 2	0.25	0.60	0.62	0.92

In Table 6.2, the differences between identified $k_{c,3}$ values for the same amplitude between Model 1 and Model 2 can be traced back to the fitting error of the chosen model (White [121]), as shown in Fig. 6.7(b). Furthermore, the J value corresponding to the identified $k_{c,3}$ with amplitude 1 mm is much bigger than that with amplitude 5 mm, 10 mm and 20 mm, which could be caused by the inaccuracy of the friction model. The reason is that the smaller the testing amplitude is, the larger proportion of the total strut force the friction will occupy. Another possible reason is the presence of the unmodelled physics such as backlash in the prototype, which again will be more dominant with smaller amplitude tests. In addition, for higher stiffness, where J seems fairly insensitive to stiffness. This could be caused by the stiffness-sensitive resonant region of the dynamic results being beyond the feasible range of testing.

6.3.3 Verification of the theoretical models

With the identified value of fluid stiffness for each model and amplitude, the comparison between simulation results and the experimental data is displayed in Fig. 6.10. The transfer functions are shown as the Bode magnitude/phase plots of strut force over velocity. It can be seen that both models can accurately represent the properties of the tested prototype across the full range of frequencies. In Figs. 6.10 (a) - (c), over the frequency range of $1-7$ Hz, the gradient of approximately 20 dB/decade for the magnitude demonstrates the inertance dominated property. The evidence is also given by the peak values of the corresponding phase of approximately 20 to 30 degrees located between 2 Hz and 3 Hz, since the positive value of phase cannot be achieved by neither the damping (phase = 0 degree) nor the stiffness (phase = -90 degree). Although the phase of the ideal inerter should be 90 degrees, the reductions in phase could be caused by the presence of the damping and elastic effects. For frequencies below 1 Hz, the friction dominated performance leads to the increase in the magnitude of the transfer function with decreasing frequency. This is caused by the decrease in the strut velocity while the friction dominated force is approximately constant for given direction of piston motion. For higher frequency region (e.g. above 6 Hz for the 1 mm amplitude case), the compliance of the prototype dominates the performance, which gives rise to the decreasing magnitude. The worse quality of fitting between the experimental data and both theoretical models above 4 Hz in Fig. 6.10(d) is linked with the relatively inaccurate identification of the fluid stiffness with the amplitude of 1 mm, shown in Fig. 6.9. In addition,

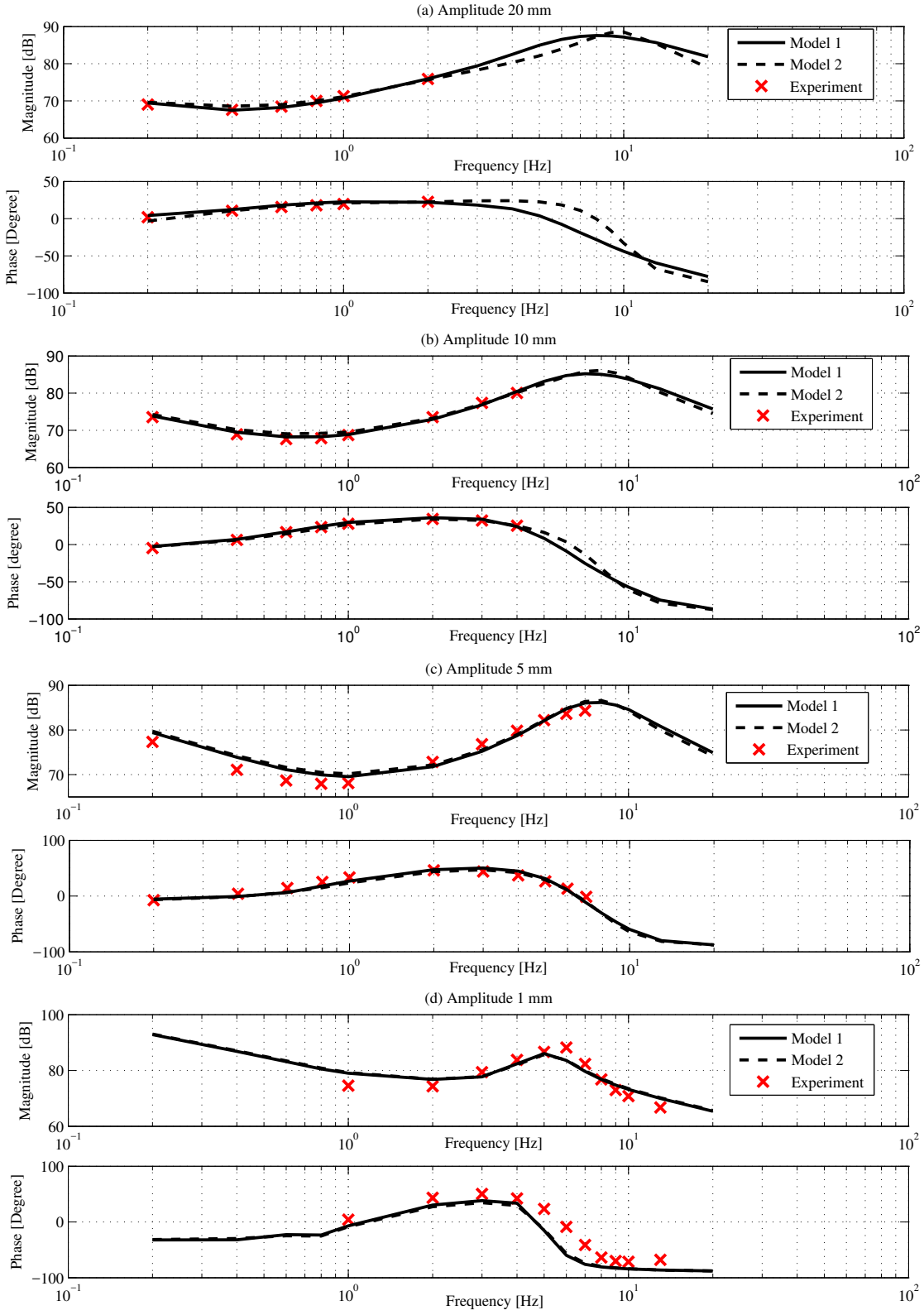

Figure 6.10: Experimental data and model simulated results of the admittance function from strut force to velocity with identified values of fluid stiffness from dynamic tests for amplitude (a) 20 mm, (b) 10 mm, (c) 5 mm, and (d) 1 mm.

the discrepancies for 1 mm could also be caused by the oscillating flow [111–114] appears when rapidly changing of flow direction. Due to the restriction of the maximum allowed forces on the cylinder, there are no experimental data available for the stiffness dominated region in Figs. 6.10(a) and (b). As a result, it can also be observed in Fig. 6.9 that J is less sensitive to the fluid stiffness change for larger amplitude, especially for the 10 mm and 20 mm cases. As a consequence, for larger amplitudes, the identification of the fluid stiffness $k_{c,3}$ based on the experimental data might be less representative. In addition, it is worth mentioning that, due to the property of hydraulic actuator, the actual amplitudes are usually slightly smaller than the demand amplitudes. To ensure the accuracy of results, the actual amplitudes are adopted in the Simulink models to keep consistent with the experimental data.

With the values of inertance and fluid stiffness determined, two theoretical models are established for the tested helical-tube fluid inerter. Both models are verified by comparing the simulation results to the experimental data, which show that the performance of tested prototype is well represented by the models across a wide frequency range. It can be seen from the results that qualitatively the frequency of $1-7$ Hz is the inertance dominated range for a fluid-based inerter while the friction dominated behaviour appears below 1 Hz and the stiffness dominated behaviour is presented above 7 Hz. For the frequencies tested, the amplitudes between $5-20$ mm are the most representative range for the device behaviour of fluid-based inerter while the less accurate model identification is found to be at the amplitude 1 mm. It can also be seen from Fig. 6.10 that good agreement between Model 1 and Model 2 are achieved in general, apart from the frequencies above 3 Hz for the 20 mm case. This can be explained by the larger fitting errors with higher flow rates, as shown in Fig. 6.7(b).

For this study, the external tube of tested prototype is made of nylon to enable modular experimental setup. However, the metal tube can be used in practical applications for more robust performance. The identified model is still applicable for fluid inerter with metal tube since the properties are independent to the material of external tube.

6.4 Summary

Following a systematic procedure, the model for each property of the helical-tube fluid inerter is identified by carrying out a series of experimental tests and model simulations. The friction and various damping effects are first identified via triangular wave tests at a wide range of strut velocities. According to the individual cylinder test result, negligible damping is assumed for piston leakage. While the friction is estimated to be 45N based on the low velocity test, the damping due to the helical tube is measured by the pressure drop across the tube. The White's formula is selected to model the nonlinear helical tube damping as it provide the best match with the experimental data. Meanwhile, the inlet/outlet damping is also calculated using an empirical formula.

Subsequently, the fluid stiffness is identified by comparing the simulated and experimental responses of the dynamic tests for each tested amplitude. The accuracy of the refined full model of the prototype is verified by the good agreement between the simulation results and the experimental data over the wide range of frequencies. Additionally, the remaining discrepancies are thoroughly analysed. Unmodelled factors, such as the backlash and coupler stiffness will be considered for the model development of the FID devices in Chapter 7.

CHAPTER 7

FLUID-INERTER INTEGRATED DAMPING (FID) DEVICE MODEL DEVELOPMENT

7.1 Overview

While the model of a specific helical-tube fluid inerter prototype is obtained in previous chapter, the generalisable model of the FID device is established in this chapter through the parameter identification of each property and validation of the simulated model. On the basis of the prototype built in Section 5.4, the network of the FID device is first improved by considering the needle valve damping and additional mechanical properties of the prototype. Then, a series of experimental tests are designed for the model identification for each property, with specialised test configurations and corresponding networks. Accordingly, the damping properties are identified by the constant velocity tests, and the coupler stiffness and friction are obtained based on the experimental analysis. Meanwhile, the influence of the parameter changes for the needle valve damping and external tube damping are comprehensively studied. Besides, the other dynamic properties (e.g. fluid stiffness and coupler backlash) are identified through the comparison between the simulated and experimental results of the dynamic tests. Finally, the established generalisable model of FID device is verified by testing and simulation with two other prototype parameter settings.

7.2 Model improvement

According to the prototype built in Section 5.4, the corresponding hydraulic network is shown in Fig. 7.1(a), in which the adjustable hydraulic resistance ($R_{v,4}$) represents the flow restriction through the needle valve. The flow branches with flow rates Q_1 and Q_4 both pass through the

cylinder inlet/outlet, which is different to the conceptual network in Fig. 4.9. In line with the adopted notation, the original hydraulic resistance $R_{io,1}$ becomes $R_{io,1+4}$ and it represents the changed flow distribution compared to Fig. 4.9. According to Eqs. (4.27) and (4.30), the relative velocity across the inlet/outlet damper ($\Delta v_{io,1+4}$) has the following relation:

$$\Delta v_{io,1+4} = v_4 - v_2 = \frac{Q_1 + Q_4}{A_1}. \tag{7.1}$$

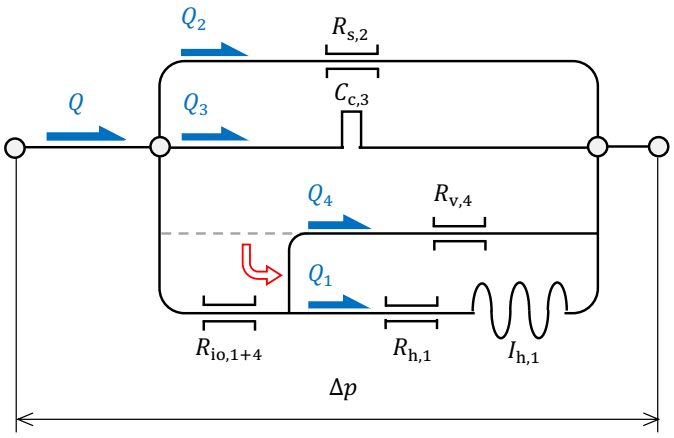

(a)

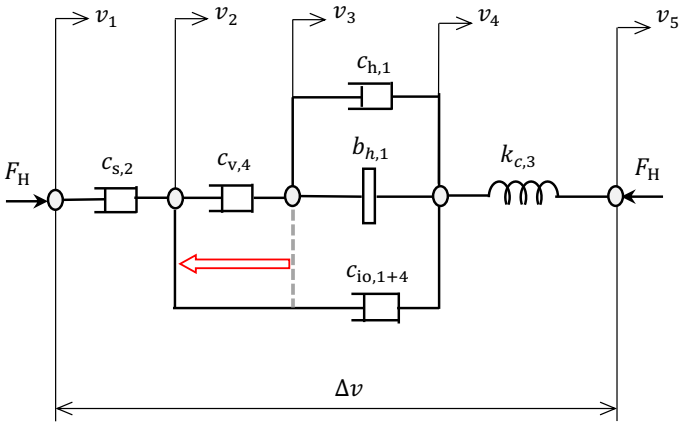

(b)

Figure 7.1: The prototype of the FID device (a) the corresponding hydraulic network, and (b) the equivalent mechanical network (the dashed line show the conceptual networks connectivity from Fig. 4.9 and 4.10).

The corresponding admittance function can be derived on the basis of Eq. (4.25) and the flow distribution shown in Fig. 5.9(b):

$$\frac{\hat{F}_H}{\Delta\hat{v}} = \frac{1}{(R_{s,2}{A_1}^2)^{-1} + C_{c,3}{A_1}^{-2}s + \left\{R_{io,1+4}{A_1}^2 + \left[(R_{v,4}{A_1}^2)^{-1} + \left(R_{h,1}{A_1}^2 + I_{h,1}{A_1}^2 s\right)^{-1}\right]^{-1}\right\}^{-1}}. \tag{7.2}$$

Using the same reasoning as in Section 4.4, the equivalent mechanical network is constructed as shown in Fig. 7.1(b), where one terminal of the cylinder inlet/out damping ($c_{io,1+4}$) is modified to match the new flow distribution. The corresponding admittance function is

$$\frac{\hat{F}_H}{\Delta\hat{v}} = \frac{1}{{c_{s,2}}^{-1} + {k_{c,3}}^{-1}s + \left\{c_{io,1+4} + \left[{c_{v,4}}^{-1} + \left(c_{h,1} + b_{h,1}s\right)^{-1}\right]^{-1}\right\}^{-1}} \tag{7.3}$$

where the element ($c_{v,4}$) is used to represent the adjustable damping though the needle valve instead of the piston valve in Fig. 4.10.

Based on previous study [4], the inlet/outlet damping is usually much less dominant than other damping effects in the fluid-based inerter. If this effect is neglected in both cases, the network of this prototype with the needle valve in Fig. 7.1(b) will be identical to the conceptual network with the piston valves in Fig. 4.10. Consequently, Eq. (7.3) equals to Eq. (4.26). This assumption will be experimentally verified later in Section 7.4.

Apart from device terminal properties caused by hydraulic elements, the FID device also possesses properties caused directly by mechanical elements, the friction (f), coupler stiffness (k_s) and the backlash (p), as highlighted in blue in Fig. 7.2. These elements do not have their counterparts in the hydraulic network (Fig. 7.1(a)). The friction (f) is produced by the relative motion between the piston rod and the cylinder seals. Here, Coulomb friction is used to model this effect, similar to Section 6.2. The coupler stiffness (k_s) represents the elasticity of the metal coupler between the actuator and the cylinder rod. The backlash (p) indicates the manufacturing clearance in the self-aligning rod coupler. The properties k_s and p have not been modelled for the fluid-based inerter in Chapter 6, but are found necessary to be included based on analysis of the time domain response in Section 7.4.1 and Section 7.4.4. Based on the actual prototype implementation, the friction (f) is modelled in parallel with the hydraulic properties, while the coupler stiffness (k_s) and backlash (p) are both in series with all the other properties, as shown in Fig. 7.2.

7.3 Modelling approach for an accurate and generalisable model

This section provides a brief high-level summary of the modelling approach for an accurate and generalisable model, where all elements in Fig. 7.2 are properly characterised.

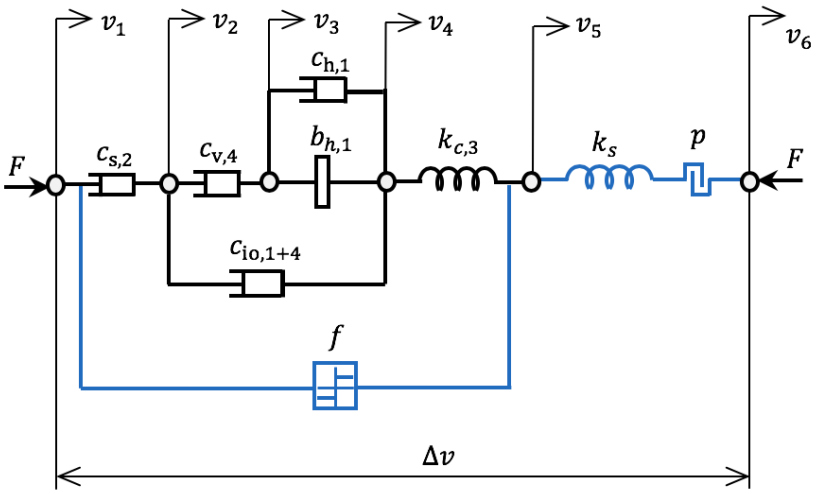

Figure 7.2: The full mechanical network characterising the terminal behaviour of the FID test rig assembly (with additional mechanical elements included in blue).

7.3.1 Identification methodology

Similar to the approach taken for the fluid-based inerter in Chapter 6, experimental tests are designed in this subsection for the property identification of the elements in Fig. 7.2. Different valve close/open status settings allow the elements to be studies separately to achieve more accurate results. In Table 7.1, the valves opening status, input excitation and observed responses are described for each test. The effective schematic diagram, corresponding hydraulic network and effective mechanical network for each prototype test configuration are plotted in Fig. 7.3. Similar to Fig. 6.1, the new symbol ' ↗ ' represents hydraulic and mechanical elements for which the nonlinear properties are quantitatively identified. Take Test I as an example, when ball valves 1 and 2 are closed, both the needle valve branch and the helical tube branch are blocked. Hence the effective schematic diagram shown in Fig. 7.3(I.a) can be obtained. Since there exists only Q_2 and Q_3, hydraulic network should be the one shown in Fig. 7.3(I.b). For the effective mechanical network shown in Fig. 7.3(I.c), apart from the potential piston leakage damping ($c_{s,2}$), the hydraulic force (F_H) could also be influenced by the fluid stiffness ($k_{c,3}$); and the strut force (F) could further be affected by the friction (f), coupler stiffness (k_s), and the backlash (p). The corresponding networks for other tests are derived following the same way. Based on the final value theorem [115], the dynamic elements, namely the stiffness ($k_{c,3}$) and inertance ($b_{h,1}$), will not influence the steady-state response during the triangular wave (constant velocity) tests (Tests I - III) after transient responses vanish. Therefore, the triangular wave period must be selected properly, and then each damping property can be studied individually. It is noted that Tests I, II and IV include both the strut force (F) and hydraulic force (F_H) in their effective mechanical networks, while Test III only has the hydraulic force (F_H). The reason is because only the pressure gauge recordings ($\Delta p_{hR,1}$) are used for Test III. It is also worth mentioning that

neither Test III nor IV has $c_{io,1+4}$ in their effective mechanical network as this source of damping is determined to be negligible earlier in Test II.

Table 7.1: Valve status*, input excitation and observed responses for the designed experimental tests.

Test	**Property**	**Ball valve 1&2**	**Ball valve 3&4**	**Needle valve**	**Input excitation Δx**	**Observed response**
I	$c_{s,2}$, k_s	Closed	–	–	Triangular wave	Transient+Steady-state
II	f, $c_{v,4}$, $c_{io,1+4}$	Open	Closed	Varying	Triangular wave	Steady-state
III	$c_{h,1}$	Open	Open	Closed	Triangular wave	Steady-state
IV	$k_{c,3}$, p	Open	Open	Closed	Sinusoidal wave	Steady-state

*The position of ball valves refer to Fig. 5.9(b)

The properties of $c_{h,1}$ has been investigated in Section 6.2.3 with formula chosen from [121]. The other empirical formula [131] will also be adopted in the model after their respective accuracy is assessed against different design parameter settings. The property of the inertance $b_{h,1}$ in Fig. 7.2 is modelled using Eq. (6.18), which represents the simplest low frequency lumped parameter model of the inertial effects in narrow liquid conduits. This model assumes that the liquid in the conduit is incompressible, inviscid and that it moves as a rigid mass under the effect of the accelerating pressure differential observed between the two liquid chambers. The properties of other elements in Fig. 7.2 are identified by the tests described in Table 7.1. Based on experimental results detailed in Section 7.4, it will be concluded that the $c_{io,1+4}$ and $c_{s,2}$ terms are negligible.

7.3.2 Variation of key design parameters

Furthermore, in order to establish the generalisable model for the FID devices, the effect of the changes in the design parameters and their influence on the main properties need to be identified, and verified with existing formulas. The needle valve damping $c_{v,4}$ is altered by changing the valve opening sizes. The external tube damping $c_{h,1}$ is affected by the changes in the tube length, tube diameter and helix diameter. These 4 design parameters are chosen because they are adjustable or simply changeable, and each of them will be investigated individually across the chosen range to cover the design configurations that are most likely to be used. The specific choices of parameter ranges serve as an example, which can be altered according to needs.

7.3.2.1 Needle valve parameter

For the needle valve, each valve setting creates the specific flow conditions with the corresponding flow coefficient (K_v) that characterises the flow rate versus the pressure drop relationships for the valve. The needle valve damping ($c_{v,4}$) is expressed with the help of the valve flow coefficient (K_v). Typically, flow valves have predetermined flow coefficients (K_v) from their manufacturers with an unit of $\mathrm{m}^3/\mathrm{hr}/\sqrt{\mathrm{bar}}$. Such coefficient is not available for the needle valve used in this prototype.

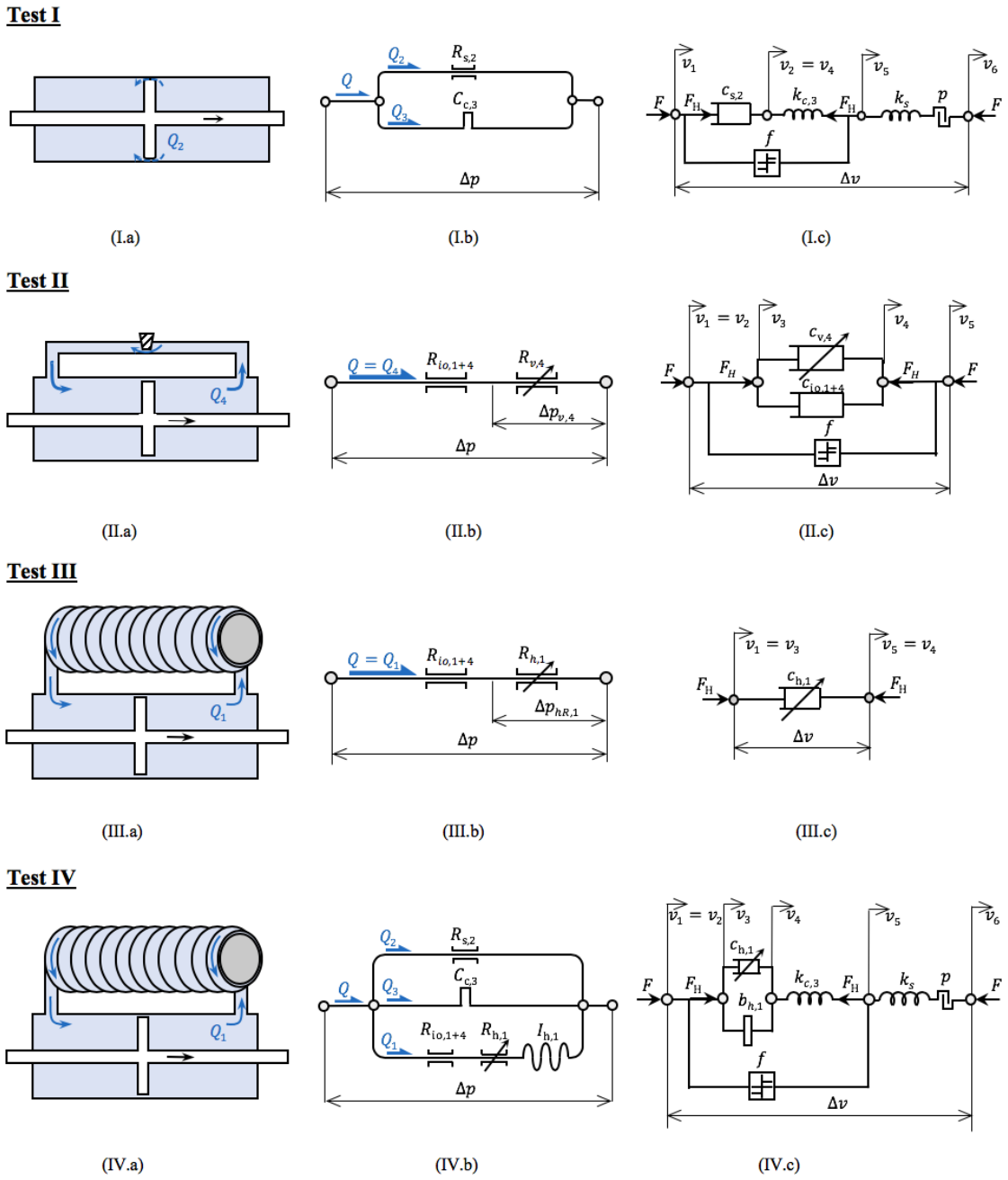

Figure 7.3: The test configurations with their corresponding: (a) schematic diagrams, (b) hydraulic network, and (c) effective mechanical network of the prototype for each test.

Therefore, in order to accurately model the needle valve damping, the experimentally determined empirical relationship will be established between the controlled valve opening and the damping coefficient $c_{v,4}$ (or flow coefficient $K_{v,4}$). The opening size of the needle valve used in the prototype is quantified by the valve opening level (n_a) marked on its control knob, which corresponds to the valve lift (h). Since the opening level can be adjusted from fully closed ($n_a = -1$) to fully open

($n_a = 5$), the experimental testing of the needle valve damping will be carried while varying the opening levels from 0 to 5 with an increment of 1, which is corresponding to the valve lift h from 0.765 mm to 4.59 mm. The range of $n_a < 0$ ($h < 0.765$ mm) is not studied. The identified empirical formula of the needle valve damping will further be verified by comparison with untested opening levels.

7.3.2.2 External tube parameters

The pressure drop ($\Delta p_{hR,1}$) across the external tube channel can be expressed by the Eq. (6.9) of the corresponding flow rate (Q_1), which was discussed in Section 6.2.3 on the basis of the surface friction loss for the single-phase fluid flow through the tube. The selected empirical expressions of Fanning friction factor f_c available for estimation of such helical tube damping in the prototype will be considered and evaluated based on their accuracy and ability to represent the measured data in Section 7.4.3.

Owing to its intended functionality, the external tube damping force ($F_{hR,1}$) could be affected by any changes of the external tube diameter (D_h), tube length (l) or helix diameter (D), as shown by Eq. (6.9). Therefore, the influence of each these tube parameters towards the external tube damping will be verified separately in Section 7.4.3. Constant velocity testing is used to generate data for comparison between the theoretical results and experimental results. To ensure the accuracy of the verification, at least 3 sets of values are selected for each tube parameter to carry out the experimental tests. The chosen parameters are listed in Table 7.2.

Table 7.2: The key design parameters of the tested prototype for the tests of each tube parameter.

Studied Parameter	**Tube length** l [m]	**Tube diameter** D_h [mm]	**Helix diameter** D [m]
Tube length l	3.88	6	0.11
	5.85		
	7.88		
	11.96		
Tube diameter D_h	6.11	4	0.075
		6	
		8	
Helix diameter D	5.81	6	0.075
			0.09
			0.11

7.4 Parameter identification

In this section, by applying the triangular displacement excitation, Test I to III are carried out to obtain the damping properties ($c_{s,2}$, $c_{v,4}$, $c_{io,1+4}$, $c_{h,1}$). Meanwhile, the coupler stiffness (k_s) and

friction (f) are also identified based on the analysis of the damping test results. Then, the other dynamic properties ($k_{c,3}$ and p) are identified through the comparison between the simulated and experimental results of the dynamic tests. Furthermore, the effects of design parameter variations on $c_{v,4}$ and $c_{h,1}$ will also be characterised.

7.4.1 Test I: Leakage damping and coupler stiffness

Although the results in Section 6.2.2 indicate negligible leakage through the piston, as new cylinder with the same specifications is used to replace the old one in the helical-tube fluid inerter prototype, the FID prototype must be tested again to identify the presence of leakage damping. Therefore, the prototype with the setup shown in Fig. 7.3(I.a) is tested at a low constant strut velocity of 2×10^{-5} m/s. The test results are shown in Fig. 7.4, in which the recorded strut forces (F) are plotted versus the strut displacement (Δx). It can be seen that, the strut force keeps increasing while the terminals of the prototype move with constant velocity, until the safe load limit (4.5 kN) is activated to unload the actuator. During the test, no fluid flow steady-state force plateau or response trend is observed, which evidences negligible leakage damping across the piston. The steep increase of the strut force can be explained by the varying compressibility effects in the fluid. Since the tests carried out in this work will not exceed the safety load limit, the leakage damping between the cylinder wall and the piston is assumed to be negligible, i.e. $c_{s,2} = \infty$. It is also worth mentioning that the lower boundary of potential leakage damping is $c_{s,2} = 225$ MNs/m based on the maximum strut force (4.5 kN) tested.

Furthermore, inspecting selected part of Fig. 7.4, at the start of the test, there is a response up to the strut displacement of 0.055 mm which shows no strut force. This is caused by the backlash (p) in the coupler between the load cell and piston rod. Since this test is completed only for a single direction, the value of p should be larger or equal to 0.055 mm, which will be further studied in Section 7.4.4. After the displacement of 0.055 mm, the strut force rapidly increases, which can be explained by the presence of the coupler stiffness, which is included in the effective network in Fig. 7.3(I.c). The coupler stiffness (k_s) is assumed to follow the Hooke's law and the corresponding terminal force $F_s = k_s \Delta x_s$, where Δx_s is the relative terminal displacement across k_s. Hence, the coupler stiffness in this work is estimated using the best-fit slope of this increase as $k_s = 2$ MN/m. The subsequent strut force with the value of approximately 62.5 N could be caused by the sliding friction (f) between the piston rod and cylinder. As seen in an inset of Fig. 7.4, after reaching a specific deformation, the next stage features a fast force increase and then the second sliding region. This behaviour can be caused by a sequential engagement of the sealing components in the tested prototype. The friction modelling is discussed in Section 7.4.2.

7.4.2 Test II: Friction, inlet/outlet damping and needle valve damping

Based on the assumption of no piston leakage gap established in Section 7.4.1, only flow branch Q_4 exists for Test II with the ball valves 1 & 2 and needle valve open but the ball vales 3 & 4

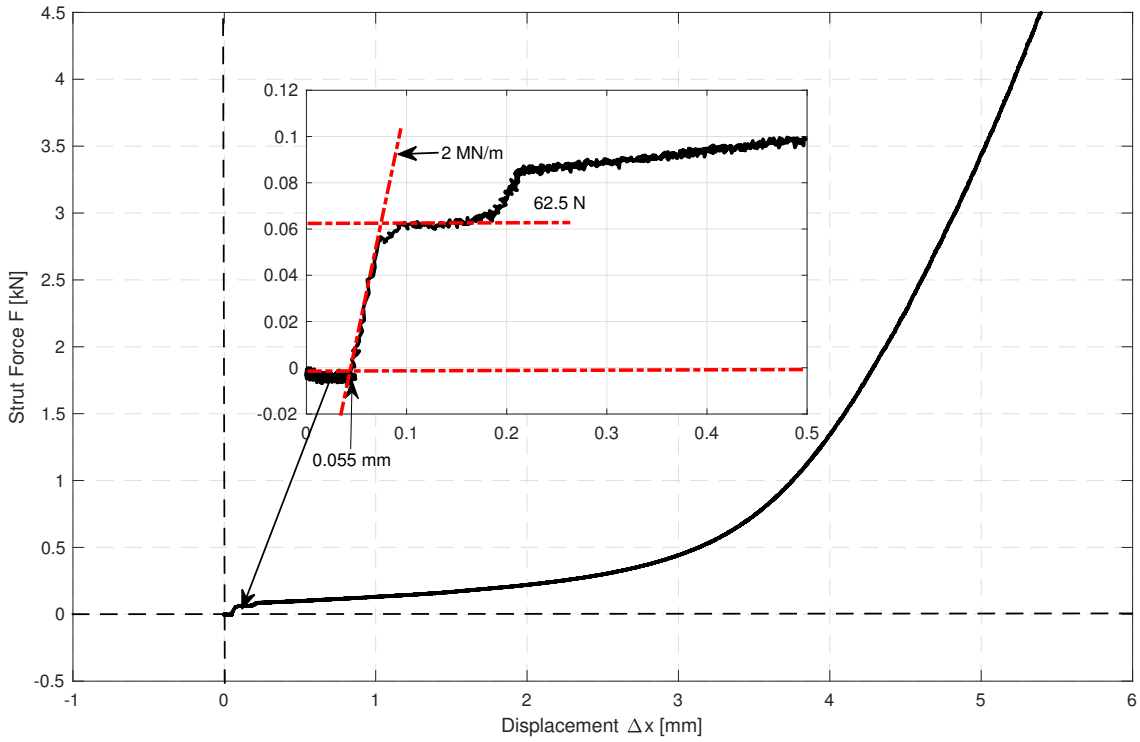

Figure 7.4: The constant velocity test at strut velocity of 2×10^{-5} m/s for Test I: $c_{s,2}$ and k_s identification.

closed, as shown in Fig. 7.3(II.b). The needle valve damping ($c_{v,4}$), inlet/outlet damping ($c_{io,1+4}$), and friction (f) are the acting effective mechanical elements during the steady-state response of the device. The relative velocity across the needle valve and inlet/outlet damping branches are both equal to the strut velocity as $v_{v,4} = v_{io,1} = \Delta v$ in Fig. 7.3(II.c). It is worth mentioning that because both the inlet/outlet damping and needle valve damping need to be identified, while having additional pressure gauges at the left and right cylinder chamber, they can also serve the purpose. With the current test rig setup, readings from both the load cell and pressure gauges are used.

During the constant velocity tests, the friction dominates the strut force at very low strut velocity. This is because other damping forces increase with the strut velocities while being negligible at low velocity. Having the needle valve open, the first sliding region estimated at the constant velocity of 2×10^{-5} m/s is approximately 62.5 N. However, this quantity, as well as the second sliding region, can reach higher values with the changing test conditions which is caused by the changing liquid pressure and, consequently, the seal friction conditions. Despite observing these rich interactions and varying conditions in the seals, to maintain the focus on the fluid flow and compressibility effects, the Coulomb model of friction with freeplay and stiffness in series is

chosen to provide the simplified representation of the observed phenomena. The applied values of the friction parameter f are further discussed in Section 7.5.1.

The characteristics of the needle valve are identified by carrying out the Test II. For each opening level (n_a), selected strut velocities are tested from 0.002 m/s to as high as the safe load limit of the load cell (4.5 kN) allows. The steady-state pressure drops across the needle valve ($\Delta p_{v,4}$ in Fig. 7.3(II.b)) are measured by the pressure gauges, and the valve damping force is calculated as $F_{v,4} = A_1 \Delta p_{v,4}$. The strut force ($F$) is recorded by the load cell, and its steady-state value is identified using the Least Absolute Residuals method implemented in MATLAB [124]. It consists of the needle valve damping force, friction and inlet/outlet damping force. According to the effective mechanical network in Fig. 7.3(II.c), the hydraulic force (F_H) is identified by removing the friction force (f) from the identified steady-state strut forces (F). In Fig. 7.5, for each tested valve opening level, the valve damping forces ($F_{v,4}$) are plotted by dashed lines, in comparison with the hydraulic forces (F_H) in solid lines. As expected, it can be seen that the smaller valve opening level leads to the larger damping force.

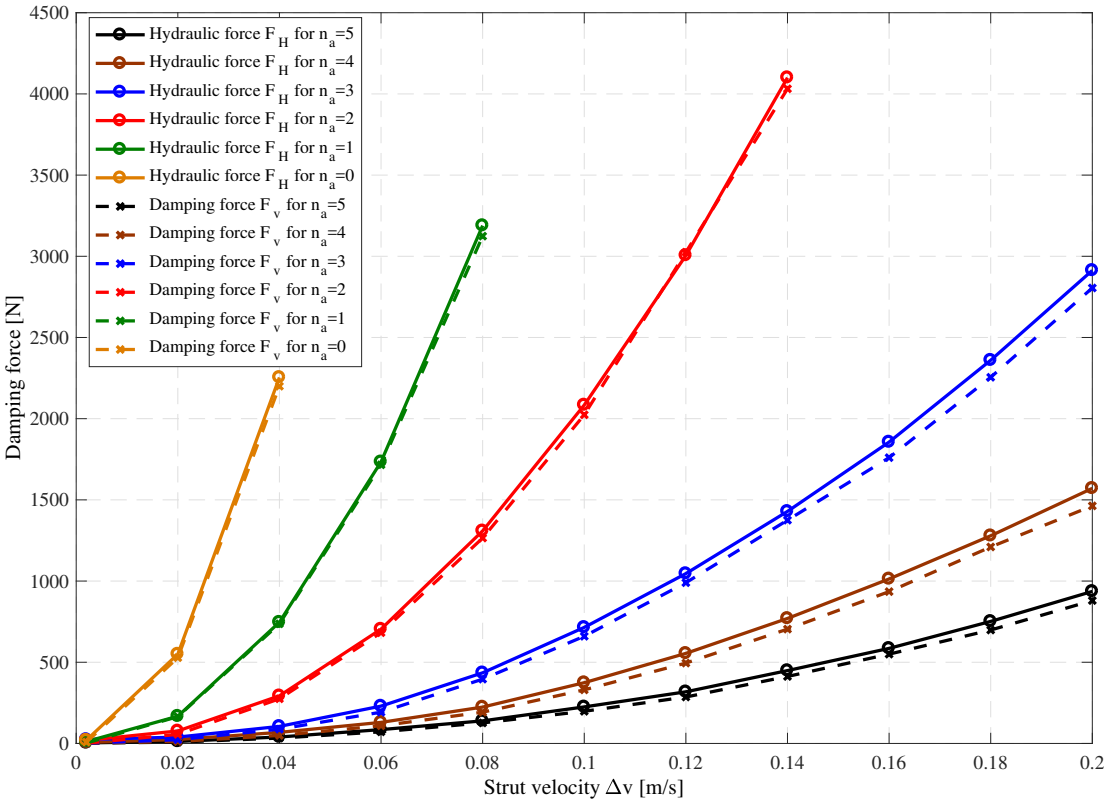

Figure 7.5: Needle valve damping properties for various valve opening levels.

In addition, based on the mechanical network in Fig. 7.3(II.c), the discrepancies between the

hydraulic forces (F_H) and needle valve damping force ($F_{v,4}$) for each opening level are caused by the inlet/outlet damping ($c_{io,1+4}$). As shown in Fig. 7.5, the difference is very small for any valve opening level (with the maximum value of 107 N when $F_H = 4100$ N, approximately 2.6 % of F_H). Hence, it is assumed that the inlet/outlet damping can be neglected in this prototype, which leads to the conclusion that the network of the prototype in Fig. 7.1(b) is equivalent to the network of the conceptual FID device in Fig. 4.10.

For the needle valve, the valve flow coefficient ($K_{v,4}$) is used to describe the relationship between the pressure drop ($\Delta p_{v,4}$) across the valves and the corresponding flow rate (Q_4) based on the Bernoulli's principle for the flows in channels and conduits [117]:

$$K_{v,4} = Q_4 \sqrt{\frac{G}{\Delta p_{v,4}}}, \tag{7.4}$$

where G is the specific gravity of the fluid, for water $G = 1$. Then, the piston valve damping force $F_{v,4}$ can be expanded by substituting Eq. (7.4) into $F_{v,4} = A_1 \Delta p_{v,4}$:

$$F_{v,4} = \frac{G {A_1}^3}{{K_{v,4}}^2} {v_{v,4}}^2. \tag{7.5}$$

It is worth mentioning that the nonlinearity is present in the needle valve damping due to the quadratic term of $v_{v,4}$ in Eq. (7.5), which demonstrates the mixed and turbulent flow through the valve. Hence, the parameter $c_{v,4}$ in the full FID model is defined as the coefficient for the quadratic velocity term $v_{v,4}$, as:

$$c_{v,4} = \frac{G {A_1}^3}{{K_{v,4}}^2}. \tag{7.6}$$

Based on Eq. (7.5), the valve flow coefficient ($K_{v,4}$) for each valve opening level is identified by fitting the experimental results of $F_{v,4}$ and Δv ($= \Delta v_{v,4}$) in Fig. 7.5, using the Bisquare method in MATLAB [124]. The summary of the fitting results is shown in Table 7.3 with the corresponding needle valve damping coefficient ($c_{v,4}$) calculated based on Eq. (7.6). It is noted that the identified values of $K_{v,4}$ are similar to the manufacturer's data for similar needle valves [132].

Subsequently, to link the needle valve damping ($c_{v,4}$) to the valve opening level (n_a) directly, the exponential equation $\alpha e^{\beta x}$ (α and β are constants) is chosen as the empirical approximating model selected from MATLAB's 'Curve fitting suite', to empirically fit the nonlinear relationship between n_a and $c_{v,4}$, again using the Bisquare method [124]. The resulting empirical formula is

$$c_{v,4} = 1.4 \times 10^6 e^{-n_a}. \tag{7.7}$$

Fig. 7.6 is presented to compare the theoretical and experimental values of the needle valve damping $c_{v,4}$ with n_a changing from 0 to 5. It can be seen that a good agreement has been achieved.

Table 7.3: Experimental fitted values of valve flow coefficient and the corresponding theoretical calculated values of valve damping coefficient.

Valve opening level n_a	**0**	**1**	**2**	**3**	**4**	**5**
Valve flow coefficient $K_{v,4}\left[\frac{\mathrm{m}^3/\mathrm{hr}}{\sqrt{\mathrm{bar}}}\right]$	0.0348	0.0597	0.0916	0.158	0.218	0.284
Valve damping coefficient $c_{v,4}\left[\frac{\mathrm{Ns}^2}{\mathrm{m}^2}\right]$	1.43×10^6	4.84×10^5	2.06×10^5	6.95×10^4	3.64×10^4	2.14×10^4

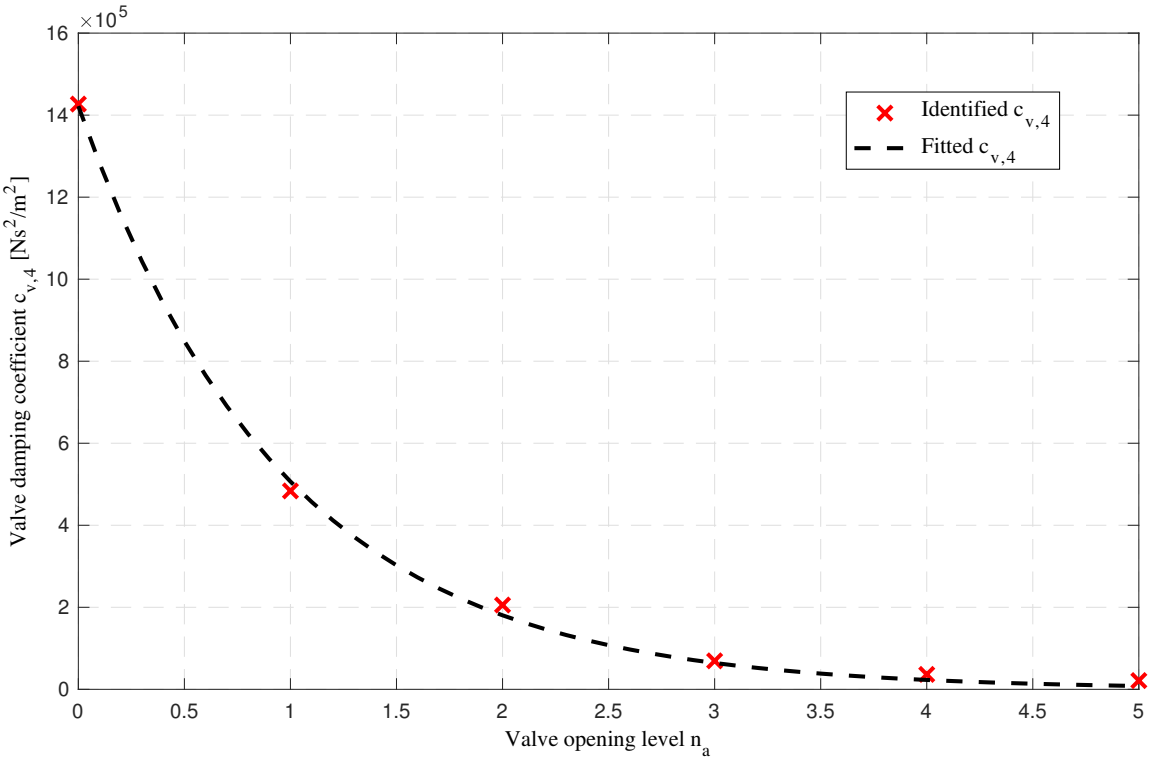

Figure 7.6: Experimental valve damping coefficients compared with the theoretical values based on Eq. (7.7).

7.4.3 Test III: External tube damping

As shown in Fig. 7.3(III.b), there is only a single flow path associated with the flow rate Q_1 when all the ball valves are opened and the needle valve is closed. The constant velocity tests for each set of the prototype's parameters in Table 7.2 are carried out to study the influence of the tube parameters' variation. During the tests, the steady-state pressure drop ($p_{hR,1}$) across the external tube channel is recorded by the two pressure gauges, the external tube damping force ($F_{hR,1}$) is then calculated by using:

$$F_{hR,1} = A_1 \Delta p_{hR,1}. \tag{7.8}$$

7.4.3.1 Tube length l

According to Eq. (6.9), the pressure drop across the external tube $\Delta p_{hR,1}$ is proportional to the tube length. The prototype with various tube lengths, as listed in Table 7.2 (3.88 m, 5.85 m, 7.88 m and 11.96 m), is tested at the constant strut velocities from 0.002 to 0.22 m/s. In Fig. 7.7(a), the experimental results of the external tube damping force versus the test velocities are plotted for each chosen tube lengths. The Reynolds number for the tested velocities, calculated using Eq. (6.6), is within the range of [585, 64353]. Since the flows with $Re > 4000$ are turbulent [117], the majority of the tested velocities generate the turbulent or mixed flow conditions. The external tube damping forces can be expressed as [133]:

$$F_{hR,1} = c_{h,1} {v_{h,1}}^2. \tag{7.9}$$

The relative velocity across the equivalent damper which represents the external tube damping is equal to the tested strut velocity as $v_{h,1} = \Delta v$ as shown in Fig. 7.3(III.c) for Test III. Combining Eqs. (4.27), (6.9), (7.8) and (7.9), the external tube damping coefficient ($c_{h,1}$) is defined as:

$$c_{h,1} = f_c \frac{2\rho l A_1}{D_h} \left(\frac{A_1}{A_2}\right)^2, \tag{7.10}$$

where the Fanning friction factor can be based on various applicable empirical formulas as listed in [119]. Based on the tube parameters (Table 5.7) and the tested flow condition (Re), the two most suitable formulas selected are:

- White [121]:

$$f_c = 0.08 Re^{-\frac{1}{4}} + 0.012 \sqrt{\frac{D_h}{D}}, \tag{7.11}$$

- Ito [131]:

$$f_c = 0.076 Re^{-\frac{1}{4}} + 0.00725 \sqrt{\frac{D_h}{D}}. \tag{7.12}$$

In Fig. 7.7(b) to 7.7(e), the resulting computed forces are plotted as the blue dashed lines for the White's formula and the red dotted lines for the Ito's formula. These predictions are compared with the experimental data, shown as the solid black lines, for each tested tube length. It can be

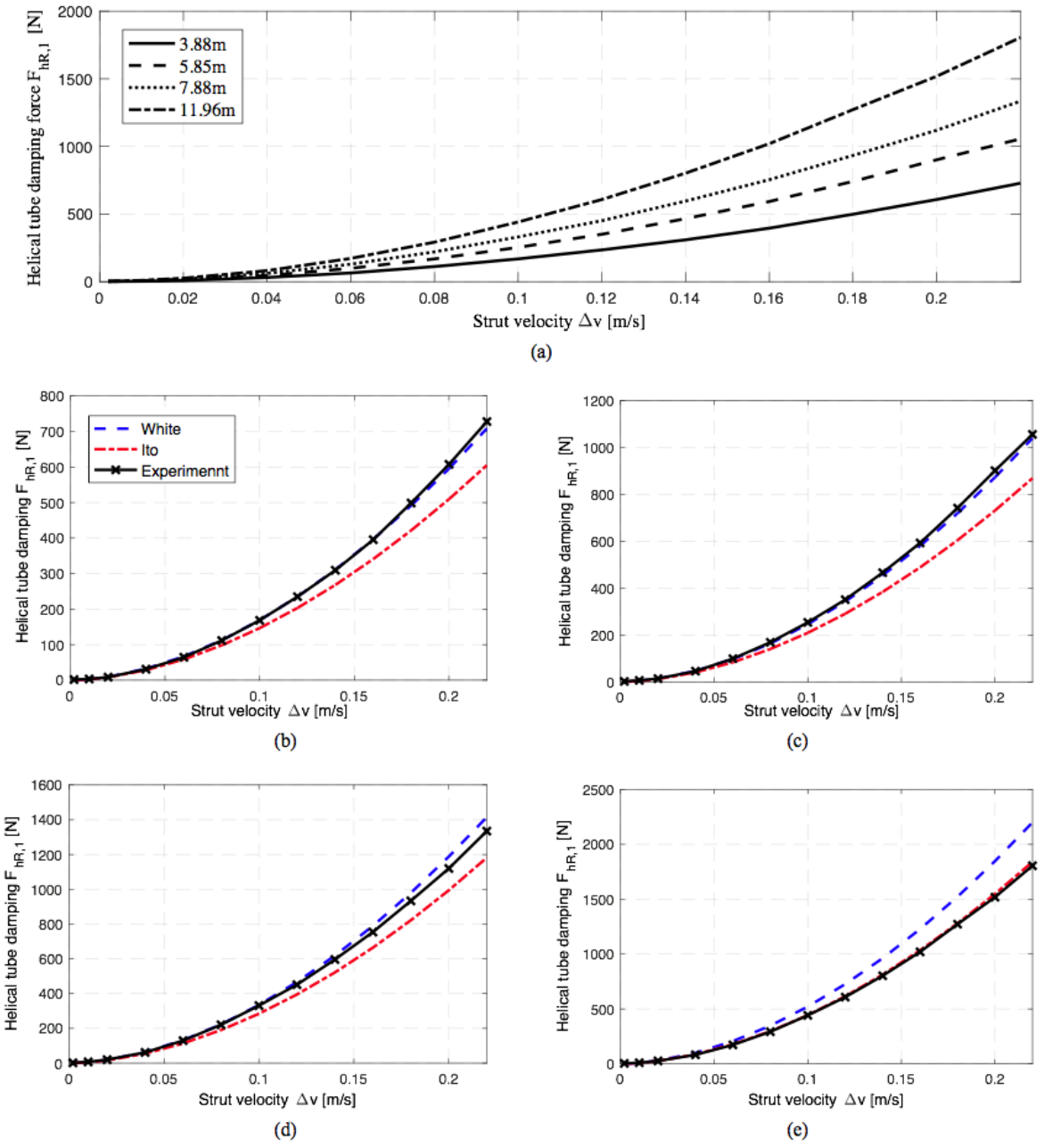

Figure 7.7: The experimental helical tube damping forces versus the strut velocity for (a) selected various tube lengths, and compared with the theoretical models for the tube lengths of (b) 3.88 m, (c) 5.85 m, (d) 7.88 m, and (e) 11.96 m.

seen that the theoretical damping values based on White's formula have good agreement with the experimental data for shorter tube lengths, while the values based on the Ito's formula present the better fit for the longest tube length.

To compare the accuracy of each formula for f_c across all the tested lengths, the root mean

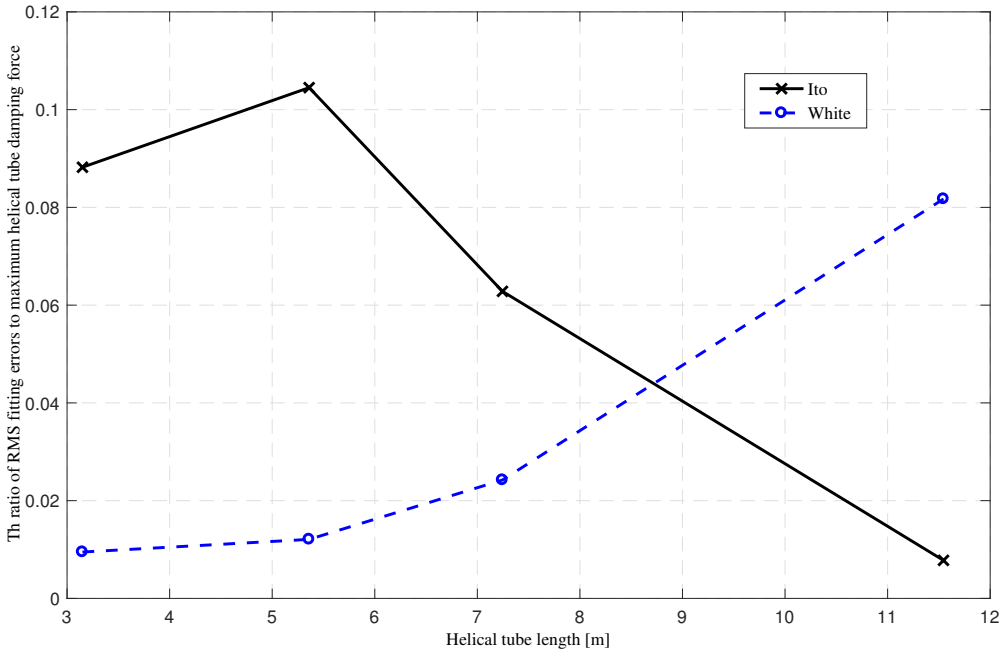

Figure 7.8: The relative errors between the experimental and theoretical helical tube damping forces for the full range of the tube lengths.

square of the differences between the experimental data and each theoretical model are calculated. The ratio of the errors to the maximum experimental helical tube damping force tested at a strut velocity of 0.22 m/s are plotted in Fig. 7.8. It is shown that the discrepancies between the theoretical values based on the White's formula and the experimental results gradually increase when the tube length becomes larger. For the Ito's formula, the trend is the opposite. It is noted that if the model established in Section 6.2.3 is used for a device with long tube length, e.g. 11.96 m, the relative fitting error will be increased by 700 % compared with the helical-tube damping modelling introduced in this section. Therefore, the external tube damping ($c_{h,1}$) is modelled by the Ito's formula for tube lengths longer than 8.7 m, while the White's formula is used to model the $c_{h,1}$ for the tube lengths shorter than 8.7 m.

7.4.3.2 Tube diameter D_h

The tube cross-sectional area (A_2) depends on the tube diameter (D_h), which then affects the ratio between the piston area and tube cross-sectional area in Eq. (7.10). Thus, three different tubes with internal diameter 4 mm, 6 mm and 8 mm are considered for the testing. Again, the tests are carried out at various constant velocities up to 0.12 m/s for each tube diameter due to the safe load limit (4.5 kN). The tube length $l = 6.11$ m < 8.7 m is selected for this set of tests, so Eqs. (7.9), (7.10) and (7.11) are used for calculation of the theoretical external tube damping forces.

In Fig. 7.9, the experimental results (red lines) are plotted and compared with the theoretical values (black lines). As the equations predict, the external tube damping force is positively correlated to the tube diameter for both the experimental and theoretical results, with only minor discrepancies between them, which could be caused by the temperature changes during the long testing or geometrical and other parameter uncertainties. It is also worth mentioning that the results efficiently validate the f_c model used in Eq. (7.11).

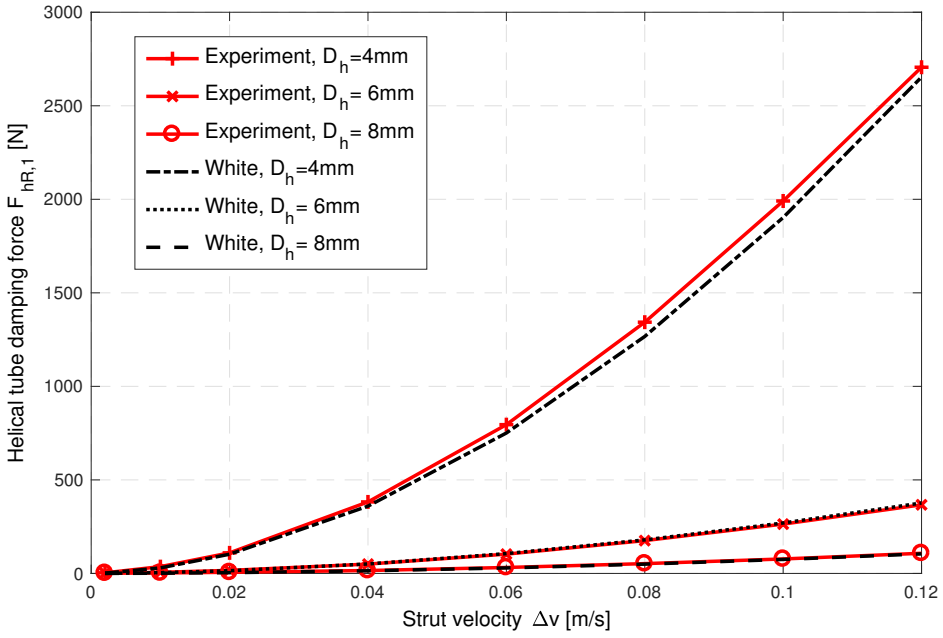

Figure 7.9: The theoretical and experimental external tube damping forces versus strut velocity for various tube diameters.

7.4.3.3 Helix diameter D

The helix diameter (D) of the tube is not presented directly in Eq. (7.10) for the external tube damping coefficient, but it is contained in the Fanning friction factor (f_c), e.g. Eq. (7.11) and Eq. (7.12). Therefore, as shown in Table 7.2, the external tube of the prototype is wrapped to a helix with diameters of 0.075 m, 0.09 m, and 0.11 m, respectively, for testing at the constant strut velocities from 0.002 to 0.22 m/s. The tube length $l = 5.81$ m < 8.7 m is selected for this set of tests, so Eqs. (7.9), (7.10) and (7.11) are used for calculation of the theoretical external tube damping forces. In Fig. 7.10, the experimental results of the tube damping force are plotted by the red lines, and the theoretical values are plotted by the black lines. The results show that the external tube damping has little variation when the helix diameter changes from 0.075 m up to 0.11 m. Meanwhile, the results also independently validate the f_c model used in Eq. (7.11).

To further verify this observation, taking the strut velocity of 0.2 m/s as an example, the

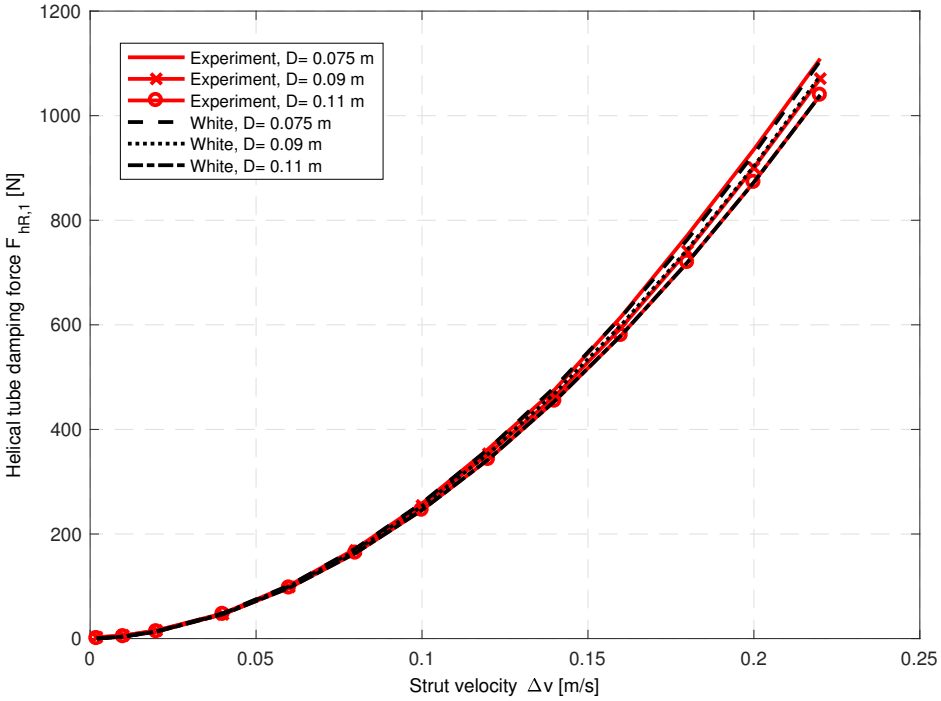

Figure 7.10: The theoretical and experimental helical tube damping forces versus strut velocity for various tube helix diameters.

theoretical tube damping forces ($F_{hR,1}$) for 5.81 m of the straight and curved tubes are calculated. Eqs. (7.9) and (7.10) are used for this theoretical calculation, and for the curved and the straight tube cases, Eqs. (7.11) and $f_c = 0.0791/Re^{-\frac{1}{4}}$ [119] respectively are adopted. The results are plotted for the range of the helix diameters (D) in Fig. 7.11. It can be seen that the difference between the damping values for the curved tube and straight tube decreases when the helix diameter increases, specifically the two damping values approach each other at $D \to \infty$. Hence, the helix diameter has decreasing influence on the external tube damping when the helix diameter becomes larger and the value of the curved tube damping gets closer to the straight tube damping. For the tested helix diameter of 0.075 m, 0.09 m and 0.11 m, as indicated in Fig. 7.11, the values of the curved tube damping forces are fairly similar, which explains the little variation of the external tube damping between the tested helix diameters. It is noted that if the external tube is wrapped to a helix with very small diameter, the external tube damping will become extremely large and very sensitive to the value of the helix diameter. It is also worth mentioning that the large difference between the values of straight tube damping force in Fig. 7.11 and meander tube damping force in Fig. 5.7 is because of the Hagen-Poieuille formula is used to calculate the straight tube damping of the meander-tube inerter for laminar flow. However, due to the calculated values of tested Reynolds numbers, the formula of f_c for turbulence flow is used to calculate the straight tube damping in Fig. 7.11.

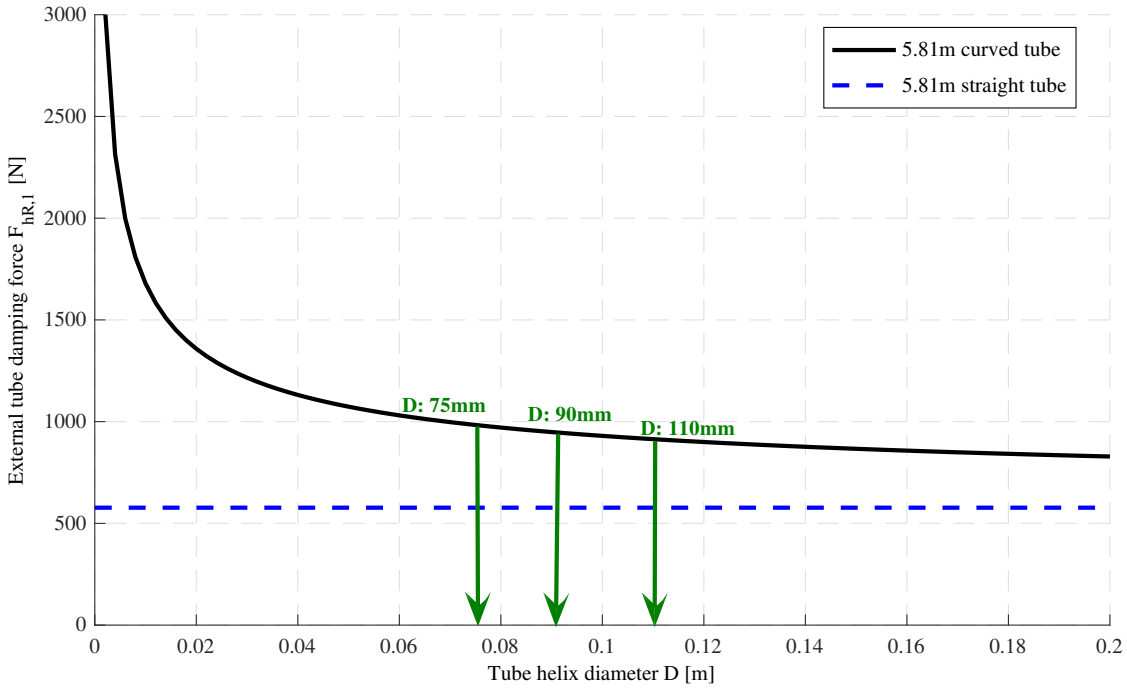

Figure 7.11: The theoretical external tube damping forces versus various tube helix diameters for 5.81 m curved tube and 5.81 m straight tube.

7.4.4 Test IV: Fluid stiffness and backlash

Assuming constant bulk modulus (B) of the working fluid, the fluid induced stiffness ($k_{c,3}$) is determined from the corresponding fluid elastic force ($F_{c,3}$) defined by Eq. (6.3). For this scenario, the fluid stiffness is proportional to the assumed constant bulk modulus.

The backlash (p) is taken as constant during the tests. It is assumed that there is no force applied on the piston rod for the distance p after changing the orientation of the piston motion.

For the Test IV, the fluid stiffness ($k_{c,3}$) and backlash (p) need to be identified through data fitting between the simulated and experimental results with harmonic displacement inputs. Accordingly, the SIMULINK model [124] is built based on the network of the prototype in Fig. 7.3(IV.c) as shown in Appendix B.1. The dynamic tests are carried out on the prototype with tube length of 5.81 m, tube diameter of 6 mm, and helix diameter of 0.11 m. The sinusoidal piston displacement inputs of various frequencies are used for the tests at amplitudes of 1 mm, 5 mm, 10 mm and 20 mm, respectively. Similar to Section 6.3.2, based on the recorded strut displacement and strut force, the non-parametric Correlation Method (Appendix A.2) is used to identify the transfer function from the strut velocity to the strut force at each tested frequency. A metric J is defined to quantify the error between the experimental and simulated results:

$$J = \sum_{i=1}^{n_f} \frac{\left|Y([k_{c,3}, p], j\omega_i) - E(j\omega_i)\right|}{|E(j\omega_i)|}, \tag{7.13}$$

where n_f is the number of frequency points, $E(j\omega_i)$ is the experimental admittance function and $Y([k_{c,3}, p], j\omega_i)$ is the computed (in Simulink) admittance function based on the model with network shown in Fig. 7.3(IV.c).

The variables $k_{c,3}$ and p are optimised by minimising the value of J, where the practical range of p is set from 0 mm to 1 mm, which is less than the minimum test amplitude 1 mm. Similar to Section 6.3.2 and Appendix A.3, the Matlab function *fminsearch* is used to minimise the value of J. The results of the identified parameters are listed in Table 7.4 for each tested amplitude. Based on the optimised results, the values of p are constant for the different amplitudes, which equals 0.07 mm. However, it is noted that the fluid stiffness varies with the amplitude, which is caused by the effective fluid compressibility effects, namely due to high sensitivity of the bulk modulus to the pressure of air contamination in the hydraulic system [129]. It is worth mentioning that it might be beneficial to use a analytical formula to predict $k_{c,3}$. However, here it is decided that the current adopted approach is compatible with the framework introduced in Section 4.4, and comparable to the approach applied to the needle valve identification $c_{v,4}$. It is also noted that the identified $k_{c,3}$ values are much lower (approximate 25% to 50%) than the results in Table 6.2 for the helical-tube fluid inerter, which could be caused by more air trapped in the FID prototype.

Table 7.4: The identified variables for Test IV at each amplitude.

Amplitude (mm)	**1**	**5**	**10**	**20**
Fluid spring stiffness $k_{c,3}$ (MN/m)	0.06	0.30	0.39	0.48
Coupler backlash p (mm)	0.07	0.07	0.07	0.07

To assess the necessity of including the coupler stiffness (k_s) and backlash (p) in the final model, the test results with an amplitude of 1 mm are plotted in Fig. 7.12 at frequencies of (a) 0.2 Hz and (b) 10 Hz, and compared with the simulation results based on the models with and without k_s and p. For the model without k_s and p, the corresponding values of the equivalent fluid spring stiffness ($k_{c,3}$) is optimised separately by the same approach. The reason for presenting the amplitude of 1 mm test case is because the influence of k_s and p is more pronounced. It can be seen that the simulated strut force without k_s and p (black dotted line) has a slight lead compared to the experimental data (red solid line). This could be caused by the unmodelled coupler compression around each directional change of the moving piston rod. The simulated strut force with k_s and p (blue dashed line) has no such discrepancy due to the inclusion of the coupler stiffness k_s in the network. Another noticeable feature is the small zero-force plateaus at the strut force responses after each directional change of the piston motion which is well represented by the backlash (p) in the coupler between the actuator and piston rod. This is

visible particularly well for the case of 0.2 Hz piston input. It is also worth mentioning that there are still additional minor discrepancies between the experimental strut force and the simulated values after each backlash event. These could be caused by the unmodelled seal and lubrication mechanics between the piston and cylinder.

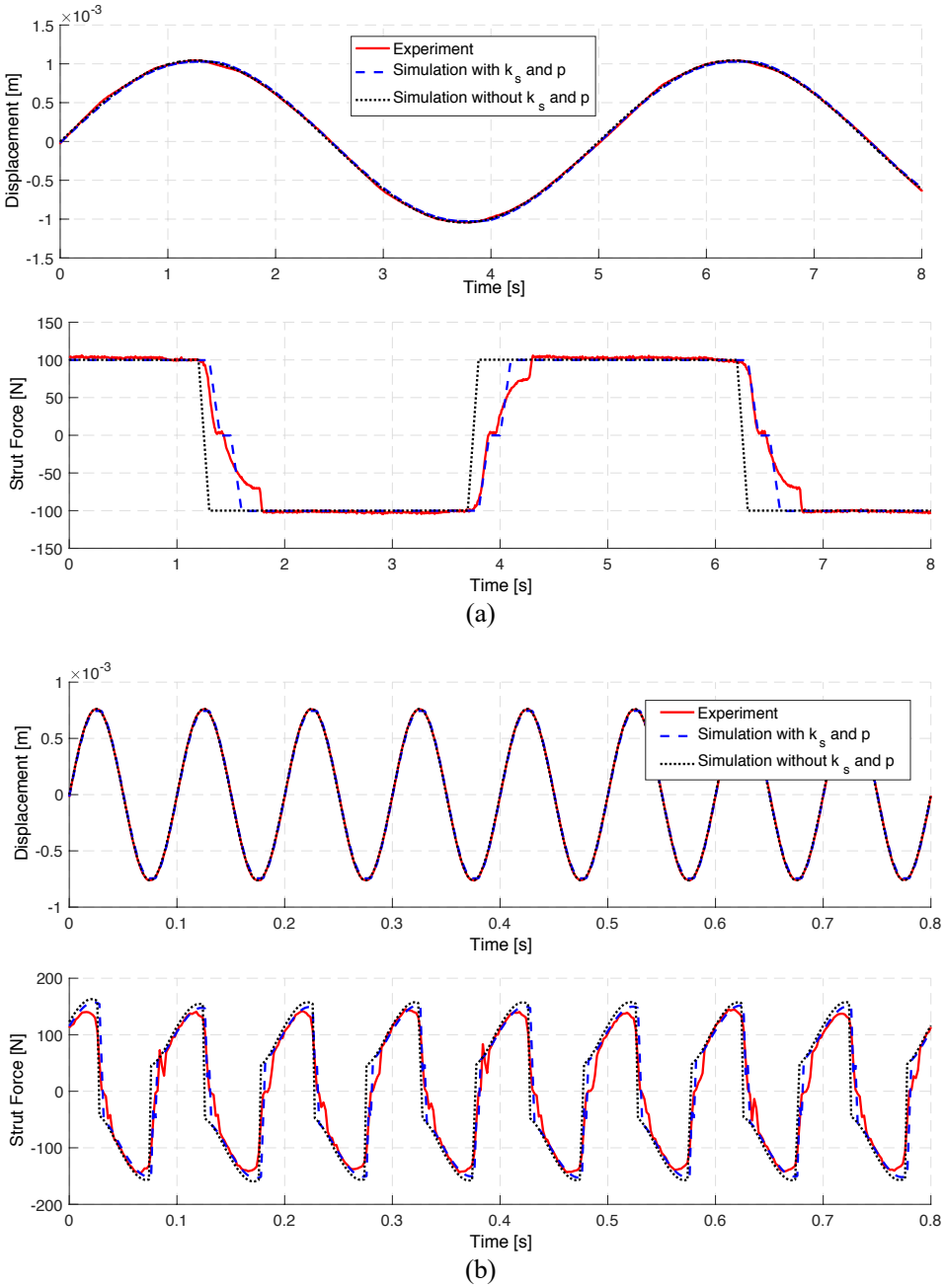

Figure 7.12: Strut displacement and strut force for dynamic tests with the amplitude of 1mm at frequencies of (a) 0.2 Hz and (b)10 Hz.

7.5 Validation of the full generalisable model

7.5.1 Generalisable model of the FID device

Based on the analysis in Section 7.4.1, the piston leakage effect is negligible. Hence, the piston leakage damping ($c_{s,2}$) is removed from Fig. 7.2. Additionally, the tube inlet/outlet damping ($c_{io,1+4}$) is neglected based on the observation in Section 7.4.2. Consequently, the final full network for the generalisable model of the FID devices discussed in this study is shown in Fig. 7.13. In this model, some parameters are experimentally identified for this specific prototype: the value of 100 N for the friction parameter f is selected as an estimation of a typical observed value of the sliding friction in the second stage identified in Fig. 7.4 and Fig. 7.12(a), the coupler stiffness (k_s) equals 2 MN/m (Section 7.4.1), and the backlash (p) is modelled as 0.07 mm (Section 7.4.4); the fluid stiffness ($k_{c,3}$) is experimentally fitted as shown in Table 7.4 for the range of the tested amplitudes; other design parameters are modelled by theoretical formulae (with measured, identified or typical values of the underlying parameters): the inertance ($b_{h,1}$) by Eq. (6.18); the needle valve damping ($c_{v,4}$) by Eq. (7.7); the external tube damping ($c_{h,1}$) by Eq. (7.10), in which the f_c is based on Eq. (7.11) (the White's formula) for tube length $l < 8.7$ m and Eq. (7.12) (the Ito's formula) for $l > 8.7$ m.

Formulae and associated validity ranges of the design parameters are summarised in Table 7.5. This table could facilitate future design of similar FID devices to achieve desired performance. For example, assuming that for a vibration absorber design problem where both the allowable fluid type and geometric dimensions match the ranges defined in Table 7.5, an optimisation problem against the desired performance criteria can then be formed using the model in Fig. 7.13 and formulae from Table 7.5 to find the optimum values for the key design parameters. It is also worth mentioning that all these validity ranges are selected based on the available parameter settings of the tested prototype. The presented generalisable model development approach can be directly applied with different design parameters ranges, and other FID device designs to pursue further enhancement of defined performance criteria.

Table 7.5: The key design parameters with the corresponding formulae and validity ranges.

Variables	**Formulae**	**Validity ranges of key design parameters**
$b_{h,1}$	$\rho l \frac{{A_1}^2}{A_2}$	$100 \le \rho \le 20000$ kg/m^3(liquid)
$c_{h,1}$	$f_c \frac{2\rho l A_1}{D_h}\left(\frac{A_1}{A_2}\right)^2$*	$\rho \approx 1000$ kg/m^3(water), $3.88 \le l \le 11.96$ m, $4 \le D_h \le 8$ mm, $0.075 \le D \le 0.11$ m
$c_{v,4}$	$1.4 \times 10^6 e^{-n_a}$	between $n_a = 0$ ($h = 0.765$ mm) and $n_a = 5$ ($h = 4.59$ mm)

*$f_c = 0.08Re^{-\frac{1}{4}} + 0.012\sqrt{\frac{D_h}{D}}$ for $l < 8.7$ m, $f_c = 0.076Re^{-\frac{1}{4}} + 0.00725\sqrt{\frac{D_h}{D}}$ for $l \ge 8.7$ m

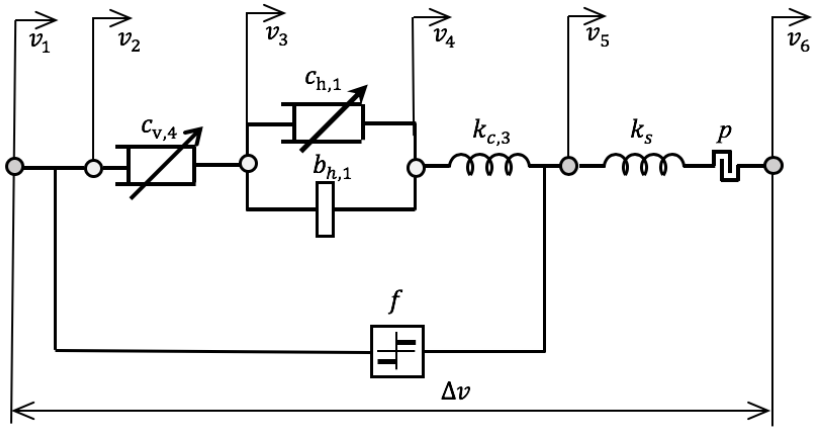

Figure 7.13: The final full network of the generalisable model of the helical-tube inerter damper device.

7.5.2 Model validation case studies

The established generalisable model is particularly useful to predict the FID device with untested design parameter settings. This is very important for optimum damping device design. In this subsection, to validate the established generalisable model, the prototype with 2 new design parameter settings listed in Table 7.6, is dynamically tested for various frequencies from 0.2 to 20 Hz at amplitudes of 1 mm, 5 mm, 10 mm and 20 mm, respectively. These data are compared with the simulated results based on the generalisable model, when using the identified fluid stiffness ($k_{c,3}$) for the corresponding amplitude in Table 7.4. It is worth mentioning that each parameter in Table 7.6 is selected to have the value different from those detailed in Section 7.3 and 7.4, which were used for establishing the model.

Table 7.6: The two new design parameter settings used for generalisability verification.

	Needle valve opening level n_a	**Helical tube length** l [m]	**Helical tube diameter** D_h [m]	**Tube helix diameter** D [m]
Set 1	1.5	4.98	0.007	0.1
Set 2	4.5			

Applying the Correlation Method [126], the experimental and simulated magnitude and phase of strut force (F) over velocity (Δv) are plotted in Bode diagram in Fig.7.14 for each tested amplitude, in which the cross and circle markers represent the experimental results for Set 1 and Set 2, respectively, while the solid and dashed lines demonstrate the corresponding simulated results. It is worth mentioning that the frequency range for the experimental results does not extend to the range for theoretical results because of the test rig safe load limit (4.5 kN) for experimental tests.

It can be seen that, in general, a good agreement between the experimental and simulated

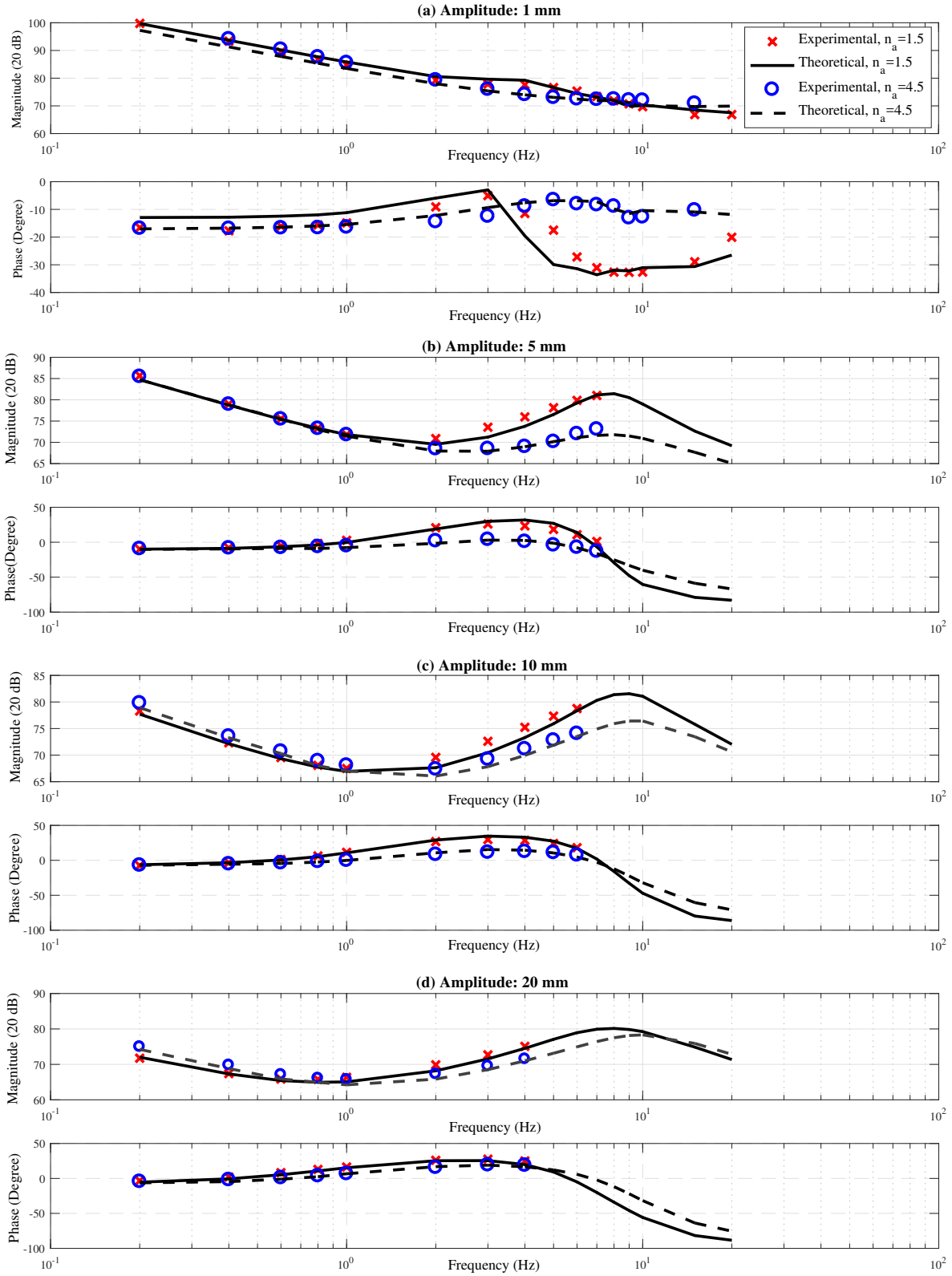

Figure 7.14: Experimental and simulated results of dynamic tests for the amplitude of (a) 1 mm, (b) 5 mm, (c) 10 mm and (d) 20 mm.

results is obtained for both selected sets of device parameters at each tested amplitude, which not only evidences the accuracy of the model for the FID devices, but also proves the generalisability of the model towards the different device scales and working conditions.

It is also noted that the curves with larger needle valve opening size (n_a = 4.5) tend to be flatter than the smaller opening size (n_a = 1.5), which indicates more contribution of the needle valve damping instead of helical tube inertance. The reason is because the flow will always prefer to choose the path with less resistance, such as the needle valve with wider opening. It also explains that, for amplitude 1 mm around high frequency excitation, the relatively large difference between the phase of the two tested opening sizes could be caused by the dominating needle valve damping for the larger opening size (n_a = 4.5) case compared with n_a = 1.5.

Finally, it is worth mentioning that the amplitudes of 5 mm to 20 mm are more representative in inducing clearly observable inertance effects in the range between 1 and 7 Hz for this FID device. The less accurate match for amplitude 1 mm during high frequencies could be caused by the relatively inaccurate modelling of the friction and elastic forces, $k_{c,3}$ and k_s, which in this FID device will dominate the strut forces for low velocity tests.

Given out the format similarity between Fig. 7.14 in this section and Fig. 6.10 in Section 7.4.3 it is importnat to point that Fig. 7.14 validates the model generalisability, while Fig. 6.10 only represents the accuracy of the non-generalisable model established in Chapter 6 for a fluid-based inerter with a specific design parameter setting.

7.6 Summary

The development of the generalisable model for FID device is presented in this chapter. Following the specialised procedure, four experimental tests are designed to measure each of the properties, respectively, and the test configurations with corresponding networks are demonstrated to facilitate the analysis of the results. The damping effects ($c_{s,2}$, $c_{v,4}$, $c_{io,1+4}$, $c_{h,1}$) are modelled experimentally, while the coupler stiffness (k_s) and friction (f) are obtained analytically. Other dynamic properties, the fluid stiffness ($k_{c,3}$) and backlash (p) are identified through the comparison between the simulated and experimental dynamic responses at each tested amplitude. In the meantime, to enable the generalisability of the model, the effects of key design parameters variation are studied towards the needle valve damping and external tube damping. Furthermore, the validity of the established generalisable model is verified by comparing the simulated dynamic response with the experimental results based on two additional device parameter settings.

The model identification methodology presented in this chapter could help to better understand the physical phenomenon in hydraulic network and be directly linked with the mechanical terminal behaviour, as well as minimise the required experimental tests by separating the identification of each property. More importantly, this approach for generalisable model establishment can be directly applied to other types of FID designs.

CHAPTER 8

CONCLUSIONS AND FUTURE WORKS

8.1 Conclusions

This work aimed to investigate the modelling methodology for the fluid inerter based vibration suppression. In the thesis, following the presented modelling procedure for the fluid-based inerter devices, the hydraulic and equivalent mechanical networks of the helical-tube fluid inerter have been obtained. A novel system identification procedure for the fluid-based devices was introduced with focused identification of friction, stiffness and various damping effects. A nonlinear model of the helical-tube fluid inerter prototype was then established to accurately characterise the prototype's dynamic properties. Furthermore, a procedure for developing an accurate generalisable model of an FID device design with adjustable design parameters has been presented. Accordingly, the established FID model has also been validated through the comparison between the simulated dynamic responses and the corresponding experimental results. The complete contributions of this work are summarised as follows:

Before the modelling of fluid inerter based vibration suppression devices, **Chapter 3** presents a numerical case study of a truck suspension design to minimise the road damage. The J_{95} index is introduced to assess the extent of road damage, with the smaller value indicating less damage. In the frequency domain, quarter-car, pitch-plane and roll-plane models with two low-complexity inerter-based linear suspension layouts are investigated by using Matlab's *fminsearch* algorithm to minimise the J_{95} index and obtained the optimum parameters of the suspension elements. In the time domain, the influence of nonlinear leaf spring on the road damage is also investigated. The J_{95} index improvement for each layout is compared with the optimised results of the conventional suspension layout. In general, it can be seen that the reduction in road damage increases with the stiffness of the suspension system.

- For the quarter-car model, the typical heavy vehicles' stiff suspension with inerter-damper series layout (S3) and inerter-damper parallel layout (S2) are predicted to offer up to 11% and 7% reduction of J_{95}, respectively.
- For the pitch-plane models, the potential J_{95} reduction can be provided by layouts S3 and S2 of 17% and 9%, respectively, while for the roll-plane models, 13% and 9% of improvement can be obtained.
- Similar levels of improvement have also been verified when the nonlinear leaf-spring is incorporated into both the S2 and S3 layouts.

In summary, this case study shows promising benefits for reduction in road damage by incorporating the inerter element into truck suspension systems and motivates the development of the inerter-based vibration suppression devices. Furthermore, as the results showed, the inerter-damper series layout (S3) always provided better improvement when compared with the inerter-damper parallel layout (S2), which further inspires and motivates the idea of the FID device with the valve damping in series with the fluid-induced inertance discussed (investigated in this work).

Chapter 4 further develops the analogy between the mechanical and hydraulic systems by replacing the mass by inerter, for the modelling of the fluid-based vibration suppression devices. With the aid of single-state pressure difference model for an ideal cylinder, the pressure-flow rate relationship for the fluid compressibility is derived. The relationships between the cross and through variables (e.g. the piston force with the pressure difference, the piston velocity with the flow rate) are identified for the external channel with assumed incompressible fluid. The admittance and series-parallel coupling are found to be convertible between the mechanical and hydraulic networks, with two example illustrated. Subsequently, the working principle of fluid-based inerters is explained and the respective flow distribution is analysed to construct the hydraulic network. By applying the selected network synthesis method and the updated analogy between the hydraulic and mechanical networks, the equivalent mechanical network is obtained, where each mechanical element is directly linked with the hydraulic counterpart. Owing to the duality between the two networks, each through variable is linked to the corresponding cross variable in the dual network, and vise versa. These findings are used for the model development in Chapter 6. Using the same procedure, the corresponding hydraulic network and equivalent mechanical network are constructed for the FID devices. The relationships between cross and through variables are also identified. Both the derived hydraulic and mechanical networks are used for the prototype design in Chapter 5 and model development in Chapter 6. The main contributions in Chapter 4 are summarised as follows:

- By involving the inerter element, the force-pressure analogy is improved between the mechanical and hydraulic networks for the modelling of the fluid-based vibration control devices.

- The mechanical and hydraulic elements are directly linked to their counterparts by applying the physical relationships between the cross/through variables, which is beneficial for understanding the physical behaviour of fluid-based vibration control devices.
- Based on the analysis of flow distribution and the updated force-pressure analogy, the corresponding hydraulic networks of the fluid-based inerters and FID devices are derived.
- A modelling procedure is established, which enables the equivalent mechanical networks of the fluid-based inerters and FID devices to be obtained by mapping the damping, inertance and stiffness effects directly to their respective hydraulic counterparts.

Chapters 5 develops the prototype of the helical-tube fluid inerter with carefully selected design parameters which is used for model development of the fluid-based inerters in Chapter 6. The customised test rig is built for this prototype, where two pressure gauges are used to precisely record the pressure drop across the external tube channel and two ball valves are used for fluid filling and helical tube replacement by isolating the helical tube channel from the cylinder chambers. An alternative prototype of the concentric helical-tube fluid inerter is also built to demonstrate the potential for incorporating the inerter into the existing damper devices, with two conceptual designs of such device are shown for a mono-tube damper and a twin-tube damper designs. Meanwhile, a new design of fluid-based inerter with the meandering tube arrangement is presented as a prototype. The corresponding meander-tube damping effect is theoretically investigated, and it is predicted to be much lower than the conventional helical-tube arrangement. Subsequently, based on the helical-tube fluid inerter design, the FID device is implemented by connecting an needle valve in parallel with the helical tube channel. The adjustable needle valve is used to model the effect of piston valve damping for the conventional dampers. The fluid-based inerter test rig is modified by adding two extra ball valves to partially isolate the needle valve flow path from the helical tube flow path for individual tests of the needle valve. The established FID device prototype is used for the model development of FID devices in Chapter 7. In the end, to ensure the accurate data capture during the experimental tests, all the measuring instruments, including the LVDT, load cell and pressure gauges, are individually calibrated. The main contributions in Chapter 5 are as follows:

- Three prototypes of the fluid-based inerter are built with selected design parameters, in which the helical-tube fluid inerter prototype is used for the first round of the experimental testing in the customised test rig.
- The prototype helical-tube FID device is built for the second round of the experimental testing with the modified and customised test rig.
- A new experimental set-up is introduced, where two pressure gauges are used to accurately measure the pressure drop across the external tube.

- A bypass needle valve design is used to model the effect of the piston valve damping with different opening sizes.

In **Chapter 6**, to enhance the modelling accuracy of the helical-tube fluid inerter built in Chapters 5, a general model identification procedure is proposed which enables the friction, stiffness and various damping effects to be identified separately. Following this procedure, the friction and damping effects are firstly identified through the tests subject to triangular wave displacement inputs at different strut velocities. With the results at very low velocity, the leakage damping is shown to be negligible and the friction is estimated by a constant value, while the White's formula describing the pressure drop through the external tube, is chosen to model the nonlinear helical tube damping by exploring the fitting error between the multiple candidate formulae, across the full tested range of velocities. The inlet/outlet damping is also estimated using an empirical formula. Subsequently, the fluid stiffness is identified based on the comparison between the theoretical and experimental dynamic responses for each tested amplitude. In addition, two comprehensive models of the tested prototype are verified by achieving the good agreement between the simulation results and the experimental data. The remaining discrepancies caused by unmodelled factors, such as the presence of air bubbles in the device, are also observed and analysed. Therefore, the model of the helical-tube fluid inerter prototype is established with quantified accuracy. The main contributions in Chapter 6 are as follows:

- An experimental procedure is presented to separate the identification of friction, stiffness and various damping effects, which allows more accurate estimation of each property.
- A dynamic model with improved accuracy is obtained using the proposed methodology for the helical-tube fluid inerter prototype.
- The validity of the established model is verified by comparing the simulated dynamic response with the experimental results.

In **Chapter 7**, a methodology for generalisable model establishment of the fluid-inerter integrated damping (FID) device is presented, which again specifies the experimental sequence to separate the identification of the friction, stiffness and various damping effects with their respective test configurations achieved by adjusting the control valve status. It is noted that the systematic use of the schematic diagrams, together with the corresponding hydraulic and equivalent mechanical networks, enables thorough understanding of the relationships between each internal hydraulic property and the corresponding mechanical parameter. Based on the equivalent mechanical network obtained in Chapter 4, the damping effect due to the needle valve and the additional mechanical properties of the FID device prototype are analysed to complete the FID device network. Then, Test I uses the constant velocity input on the isolated cylinder chambers at very low velocity. It is concluded that the negligible leakage is observed and the coupler stiffness is estimated to be a constant value. Test II carries out the constant velocity

test of the opened needle valve flow path at various velocities and valve opening levels, which is concluded that the friction is estimated by a constant value based on the low velocity test result, and the needle valve damping is identified to have the nonlinear relationship between the opening level and damping coefficient, as well as the inlet/outlet damping is observed as negligible for the tested prototype. Meanwhile, to enable the generalisability of the model, the influence of key design parameters variation are studied towards the damping properties, which is concluded that the needle valve damping exponentially decreases with the increasing opening size, and the external tube damping raises with the increasing tube length, decreasing diameter or decreasing helix diameter as the empirical formula predicted in Test III. It also can be seen from the results of Test III that the White's and Ito's formulae should respectively be used for helical-tube damping model with tube length $l < 8.7$ m and $l \geq 8.7$ m. Subsequently, Test IV carries out the sinusoidal wave tests of the helical-tube channel opened only configuration at selected amplitudes and various frequencies, the results of which is compared with the simulated dynamic response at the same amplitudes and frequencies to obtained the optimum values of the fluid stiffness and coupler backlash. In addition, the validity of the established generalisable model is verified by comparing the simulated dynamic response with the experimental results based on two unused device parameter settings. It is shown that, in general, a good agreement is obtained for both selected sets of device parameters at each tested amplitude. This not only shows the accuracy of the model for the FID devices, but it also evidences the generalisability of the model towards the different device scales and working conditions. The main contributions in Chapter 7 are:

- A methodology for the generalisable model establishment is presented, which specifies experimental sequence to separate the identification of each property with respective test configurations achieved by adjusting the control valve status.
- A generalisable model is developed for the selected fluid-inerter integrated damping(FID) design.
- The validity of the established generalisable model is verified by comparing the simulated dynamic responses with the experimental results.
- The presented methodology, after relevant modifications, is applicable to other fluid-based vibration suppression device designs.

For the FID device design problem, an optimisation can be carried out against the desired performance criteria using the models and formulae developed in this work, to obtain the optimum values of the key design parameters. The generalisable model development methodology established in this work has the advantage of providing more physical insights by linking closely the physical hydraulic elements with the device terminal force-velocity device behaviour, effectively reducing the required experimental effort because of the smaller subsets of element

properties can be identified separately, and by being directly applicable to the design and analysis of more complex damping systems.

8.2 Future works

Based on the work presented in this thesis, there are still many directions that can be extended into the future research. A few examples are listed in this section.

Air content identification
The results in Section 6.2.2 have shown that there is unexpected air presented inside the cylinder chambers. However, the air content is unknown. It also can be seen from Section 6.3.2 and Section 7.4.4 that the bulk modulus is highly sensitive to the volume of the unexpected air in a certain volume of fluid, which could significantly reduce the fluid stiffness $k_{c,3}$. Therefore, the air content identification can be considered in the future work by introducing individual tests for the fluid stiffness identification. Then, the direct use of the effective bulk modulus according to Eq. (6.5) could constitute the basis for the refined approach toward the handling of the parameter $k_{c,3}$.

Pressure-sensitive compressibility
As it is mentioned in Section 6.3.2 and Section 7.4.4 that higher pressures lead to bigger bulk modulus for the liquid-gas mixture [102, 130]. The fluid stiffness currently is identified for each tested amplitude since its value varies with the amplitude. This variation is caused by the effective fluid compressibility effects, namely due to high sensitivity of the bulk modulus to the pressure of air contamination in the hydraulic system [129]. Therefore, the pressure-sensitive compressibility can be considered for the identification of fluid stiffness using suitable theory. Due to the assumption of the incompressible fluid in the external tube channel, two additional pressure sensors need to be placed in the cylinder chambers, monitoring the pressure inside the chambers. This experimental setup would also enable the pressure drop through the cylinder inlet/outlet to be accurately measured. Thus, the inlet/outlet damping could be identified with better accuracy when compared with the previous estimation based on the empirical formula.

Applications with generalisable model
As Section 2.3 shown, the previous theoretical applications of inerters are mainly based on the model of the ideal inerter. A few other application studies also adopted the model of the flywheel-based inerter with nonlinear friction and backlash, or the model of fluid-based inerter with nonlinear damping effects. While the generalisable model of the FID devices is established in this work with improved accuracy and adjustable dynamic properties, this model can be taken into selected application studies to testify the potential benefits of the FID device in different areas. The parallel connected external tube damping and the series connected piston valve damping

could be used to compensate for the required damping in the optimum vibration suppression systems. Meanwhile, by using the method presented in Section 5.2.1, the design parameters of the device can be selected based on the optimised results obtained for each application.

Meander-tube fluid inerter

In Section 5.3.2, the meander-tube design of the fluid-based inerter is presented with theoretically lower external-tube damping generated when compared with the helical-tube design. However, due to the difficulty when building the prototype with small tube curvature, while keeping the same tube diameter as the reference design, the developed prototype of the meander-tube fluid inerter can not provide the designed damping property. As a future work, more advanced manufacturing technique could be tried to realise the prototype with the designed tube diameter and bend radius to verify the damping properties of the meander-tube design experimentally.

FID device improvement

In Section 5.3.1, two examples of the conceptual design that combines the inertial effect with the existing damper device are illustrated. It can be seen that the concentric helical tube channel is convenient to be incorporated into the hydraulic damper for either the mono-tube or the twin-tube structures. As a future work, the respective prototypes can be built by using a tailored cylinder with built-in helical tube channel. Then, the corresponding models of the FID device can be further verified by carrying out the experimental tests of these prototypes.

APPENDIX A

APPENDICES TO CHAPTER 5

A.1 Simulink models of the helical-tube fluid inerter prototype

A.1.1 Model 1

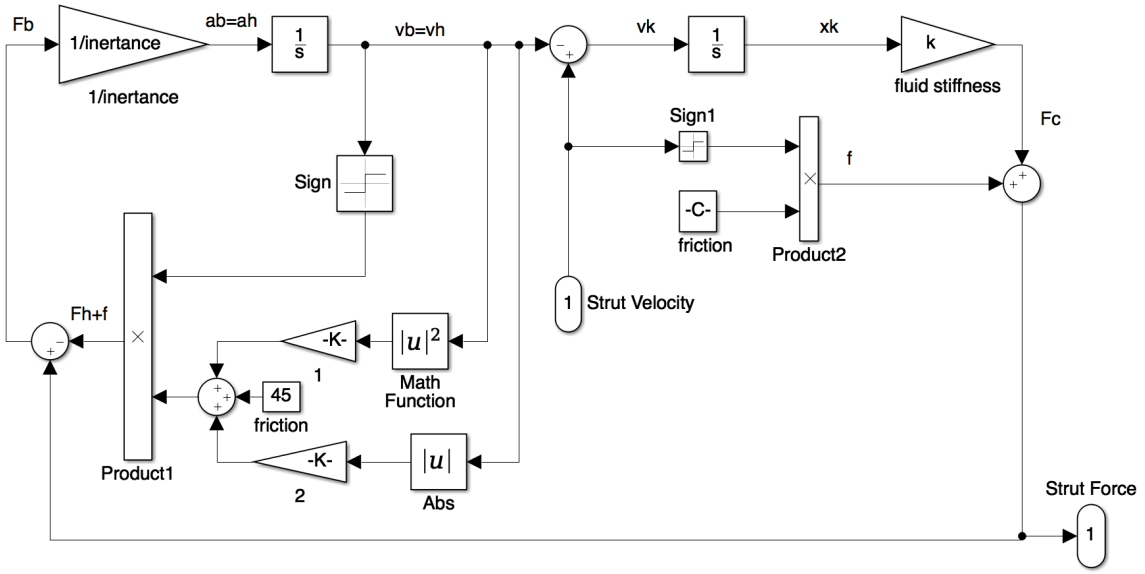

Figure A.1: Simulink Model 1 for the helical-tube fluid inerter prototype with $c_{h,1}$ calculated according to Eq. (6.14).

A.1.2 Model 2

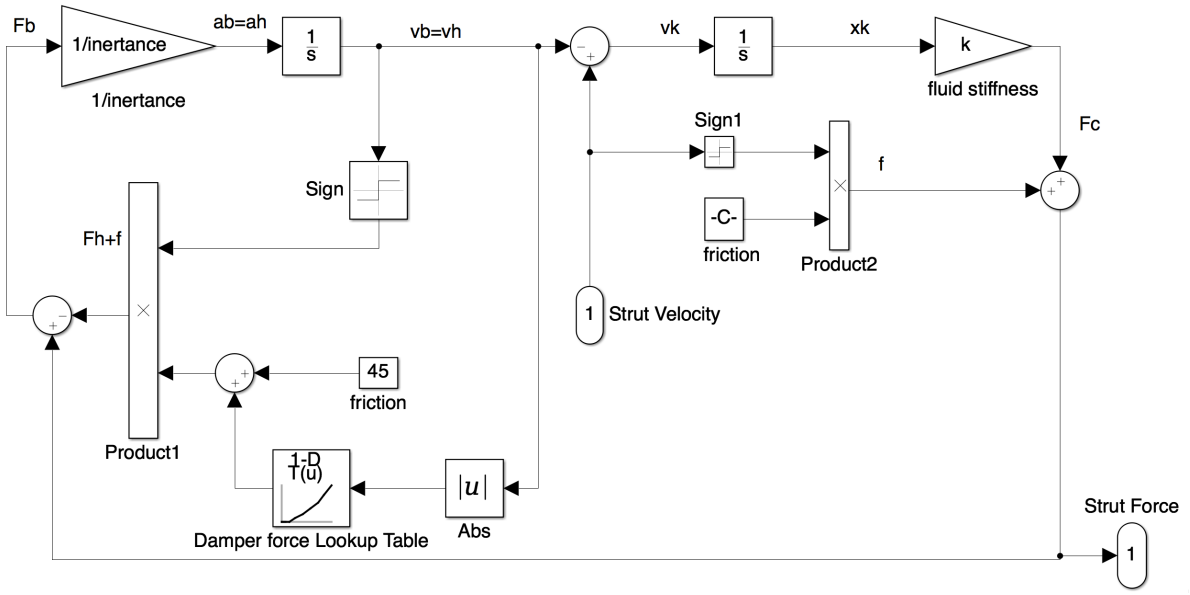

Figure A.2: Simulink Model 2 for the helical-tube fluid inerter prototype with $c_{h,1}$ obtained based on Fig. 6.4.

A.2 Correlation method

The correlation method [126] is used to calculate the gain and phase of the transfer function, while it is assumed that the system to be linear at each frequency. The noise from the experimental data will also be correlated out through this method. The gain and phase for both strut force and velocity are derived to calculate the admittance of the model. The input signal is defined as:

$$u(t) = \alpha cos(\omega t) \tag{A.1}$$

where α is the amplitude, ω is the angular frequency of input and t is the time. The output signal is then:

$$y(t) = \alpha |G_0(e^{i\omega})| cos(\omega t + \phi) + v(t) + \text{transient} \tag{A.2}$$

where $|G_0(e^{i\omega})|$ is the gain, ϕ is the phase delay with formula of $\phi = arg G_0(e^{i\omega})$, and $v(t)$ is the noise component. The output signal is repeated by a numbers of samping points to filter out the $v(t)$:

$$I_c(N) = \frac{1}{N}\sum_{i=1}^{N} y(t)cos(\omega t) \tag{A.3}$$

$$I_s(N) = \frac{1}{N}\sum_{i=1}^{N} y(t)sin(\omega t) \tag{A.4}$$

where N is the number of time sampling points. By substituting Eq. (A.2) into Eqs. (A.3) and (A.4), respectively,

$$I_c(N) = \frac{1}{2}\alpha|G_0(e^{i\omega})|cos\phi + \alpha|G_0(e^{i\omega})|\frac{1}{2}\frac{1}{N}\sum_{i=1}^{N} cos(2\omega t+\phi) + \frac{1}{N}\sum_{i=1}^{N} v(t)cos(\omega t) \tag{A.5}$$

$$I_s(N) = -\frac{1}{2}\alpha|G_0(e^{i\omega})|sin\phi + \alpha|G_0(e^{i\omega})|\frac{1}{2}\frac{1}{N}\sum_{i=1}^{N} y(t)sin(2\omega t+\phi) + \frac{1}{N}\sum_{i=1}^{N} v(t)sin(\omega t) \tag{A.6}$$

when N tends to infinity, second term for both Eqs. (A.5) and A.6 will tend to zero and the third term will disappear if $v(t)$ does not contain a pure periodic component of the input frequency. Therefore, the sums of I_c and I_s are:

$$\lim_{N\to\infty} I_c(N) = \frac{1}{2}\alpha|G_0(e^{i\omega})|cos\phi \tag{A.7}$$

$$\lim_{N\to\infty} I_s(N) = -\frac{1}{2}\alpha|G_0(e^{i\omega})|sin\phi \tag{A.8}$$

Then the gain and phase of the output signals can be estimated by:

$$|\hat{G}_N(e^{i\omega})| = \frac{\sqrt{{I_c}^2(N) + {I_s}^2}(N)}{\alpha/2} \tag{A.9}$$

$$\hat{\phi}_N = arg\hat{G}_N(e^{i\omega}) = -arctan\frac{I_s(N)}{I_c(N)} \tag{A.10}$$

Accordingly, the gain and phase of strut force and velocity are estimated using Eqs. (A.9) and (A.10), respectively. The gain and phased of the admittance with respect to strut force over velocity are then derived as:

$$|\hat{G}_{admittance}| = \frac{|\hat{G}_{force}(e^{i\omega})|}{|\hat{G}_{velocity}(e^{i\omega})|} \tag{A.11}$$

$$\hat{\phi}_{admittance} = \hat{\phi}_{force} - \hat{\phi}_{velocity} \tag{A.12}$$

A.3 Optimisation for identification of the fluid stiffness

```
%optimisation options
options = ...
    optimset('Display','iter','MaxIter',300,'MaxFunEvals',300,'TolFun',1e-2,'TolX',1e-1);

%initial value
par_init=[30.64e+06];

%optimisation
[par_opt,J_fin] = fminsearch('fluid_inerter',par_init,options);

%optimum value of stiffness
k_opt=par_opt;

%the corresponding cost
J_opt=J_fin;

%function 'fluid_inerter'
function cost = fluid_inerter(par)

% Tested frequencies for each amplitude
Amp=1;
fre=[ 1 2 3 4 5 6 7 8 9 10 13];
load 'amplitude 1.mat'

Amp=5;
fre=[0.2 0.4 0.6 0.8 1 2 3 4 5 6 7 ] ;
load 'amplitude 5.mat'

Amp=10;
fre=[0.2 0.4 0.6 0.8 1  2 3 4] ;
load 'amplitude 10.mat'

Amp=20;
fre=[0.2 0.4 0.6 0.8 1 2 ] ;
load 'amplitude 20.mat'

i=length(fre);
xx=zeros(1,i);
yy=zeros(1,i);

%parameters
inertance=219.42;
k=par;
friction=45;

cost=0;
for n=1:i;

    A=Amp/1000; % Amplitude (mm)
```

```
49      L=0.247-0.0175;   % cylinder chamber length
50
51      % Frequency (Hz)
52      f=fre(n);
53      r1=0.02;      % piston radius
54      r0=0.008;     % Rod radius
55      r2=0.003;     % Tube inner radius
56
57      A1=pi*r1^2-pi*r0^2;  % piston area
58      A2=pi*r2^2;          % channel area
59      p=995.6;             % water density at 30 degree
60
61      %%% call simulink model  %%%%%%
62      options=simset('SrcWorkspace','current','DstWorkspace','current');
63      simOut = sim('Fluid_inerter_with_c.mdl',[],options);
64      %%% get the output from simulink
65      Time=t;
66      Load=F;
67      Velocity=V;
68      N=length(Time);
69
70      %Correlation method
71      %velocity
72      Icp=0;
73      Isp=0;
74      for m=1:1:N;
75          Icp=Icp+Velocity(m)*cos(f*2*pi*Time(m));
76          Isp=Isp+Velocity(m)*sin(f*2*pi*Time(m));
77          %     Icp=Icp-f*2*pi*Position(i)*sin(f*2*pi*Time(i));
78          %     Isp=Isp+f*2*pi*Position(i)*cos(f*2*pi*Time(i));
79      end;
80      Icp=Icp/(N);
81      Isp=Isp/(N);
82      Gainp=sqrt(Icp^2+Isp^2)/(A/2);
83      Phasep=-atan(Isp/Icp)*360/(2*pi);
84
85      %Load
86      Icl=0;
87      Isl=0;
88      for m=1:1:N;
89          Icl=Icl+Load(m)*cos(f*2*pi*Time(m));
90          Isl=Isl+Load(m)*sin(f*2*pi*Time(m));
91      end;
92      Icl=Icl/(N);
93      Isl=Isl/(N);
94      Gainl=sqrt(Icl^2+Isl^2)/(A/2);
95      Phasel=-atan(Isl/Icl)*360/(2*pi);
96
97      %Calculation of gain of admittance
98      xx(n)=Gainl/Gainp;
99      yy(n)=Phasel-Phasep;
100     if yy(n)<0;
```

```
101             yy(n)=yy(n)+180;
102         end;
103         if yy(n)>90;
104             yy(n)=yy(n)-180;
105         end;
106
107         %simulation admittance
108         aa=sqrt(xx(n)^2/(1+tan(2*pi*(yy(n)/360))^2));
109         bb=aa*tan(2*pi*(yy(n)/360));
110
111         %experimental admittance
112         a=sqrt(x(n)^2/(1+tan(2*pi*(y(n)/360))^2));
113         b=a*tan(2*pi*(y(n)/360));
114
115         %comparison between experimental and theoretical admittance
116         cost=cost+sqrt((aa-a)^2+((bb-b))^2)/sqrt(a^2+b^2);
117     end
118     end
119     % }
```

APPENDIX B

APPENDICES TO CHAPTER 6

B.1 Simulink model of the FID device prototype

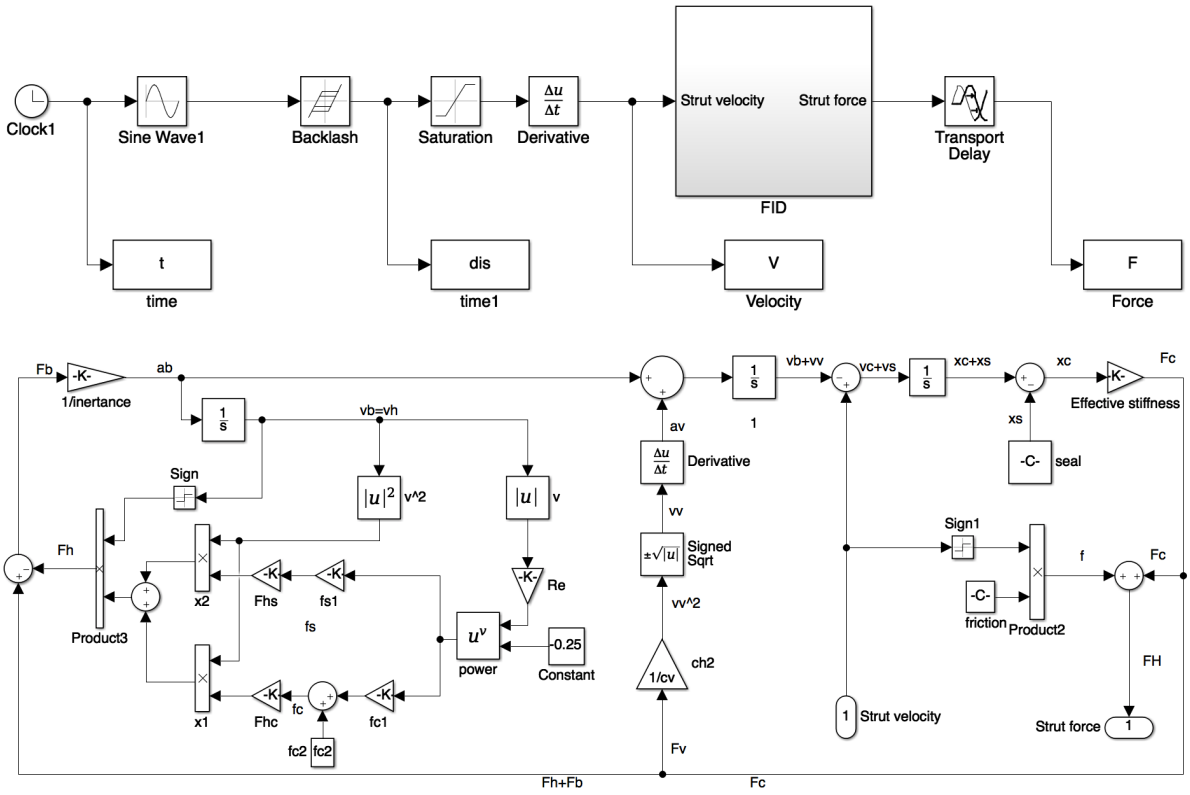

Figure B.1: Simulink Model for the fluid-inerter integrated damping (FID) device prototype.

BIBLIOGRAPHY

[1] J. Krodkiewski, "Mechanical vibration," *University of Melbourne, Melbourne, Australia*, 2008.

[2] M. C. Smith, "Synthesis of mechanical networks: the inerter," *IEEE Transactions on automatic control*, vol. 47, no. 10, pp. 1648–1662, 2002.

[3] S. Collins, "Racecar engineering articles," *https://www.racecar-engineering.com/articles/f1/understanding-the-j-damper/*, 2008.

[4] S. Swift, M. C. Smith, A. Glover, C. Papageorgiou, B. Gartner, and N. E. Houghton, "Design and modelling of a fluid inerter," *International Journal of Control*, vol. 86, no. 11, pp. 2035–2051, 2013.

[5] Y. Shen, L. Chen, Y. Liu, and X. Zhang, "Modeling and optimization of vehicle suspension employing a nonlinear fluid inerter," *Shock and Vibration*, vol. 2016, 2016.

[6] K. Craig, "Mechanical system elements," *Mechatronics, Physical Modeling - Mechanical*, 2001.

[7] N. Ho, "Modeling mechanical systems," *Modeling and Simulation of Dynamic Systems*, 2010.

[8] E. Cheever, "Elements of translating mechanical systems," *Mechanical Systems (Translating)*, 2019.

[9] M. Z. Chen, C. Papageorgiou, F. Scheibe, F.-C. Wang, and M. C. Smith, "The missing mechanical circuit element," *IEEE Circuits and Systems Magazine*, vol. 9, no. 1, 2009.

[10] F. A. Firestone, "A new analogy between mechanical and electrical systems," *The Journal of the Acoustical Society of America*, vol. 4, no. 3, pp. 249–267, 1933.

[11] H. M. Trent, "Isomorphisms between oriented linear graphs and lumped physical systems," *The Journal of the Acoustical Society of America*, vol. 27, no. 3, pp. 500–527, 1955.

[12] F.-C. Wang, M.-K. Liao, B.-H. Liao, W.-J. Su, and H.-A. Chan, "The performance improvements of train suspension systems with mechanical networks employing inerters," *Vehicle System Dynamics*, vol. 47, no. 7, pp. 805–830, 2009.

[13] F.-C. Wang and M.-K. Liao, "The lateral stability of train suspension systems employing inerters," *Vehicle System Dynamics*, vol. 48, no. 5, pp. 619–643, 2010.

[14] F.-C. Wang, M.-R. Hsieh, and H.-J. Chen, "Stability and performance analysis of a full-train system with inerters," *Vehicle System Dynamics*, vol. 50, no. 4, pp. 545–571, 2012.

[15] J. Z. Jiang, A. Z. Matamoros-Sanchez, R. M. Goodall, and M. C. Smith, "Passive suspensions incorporating inerters for railway vehicles," *Vehicle System Dynamics*, vol. 50, no. sup1, pp. 263–276, 2012.

[16] J. Z. Jiang, A. Z. Matamoros-Sanchez, R. M. Goodall, and M. C. Smith, "Performance benefit in two-axle railway vehicle suspensions employing inerters," *Developments in Control Theory Towards Glocal Control*, vol. 11, pp. 99–107, 2012.

[17] J. Z. Jiang, A. Z. Matamoros-Sanchez, A. Zolotas, R. M. Goodall, and M. C. Smith, "Passive suspensions for ride quality improvement of two-axle railway vehicles," *Proceedings of the Institution of Mechanical Engineers, Part F: Journal of Rail and Rapid Transit*, vol. 229, no. 3, pp. 315–329, 2015.

[18] T. Lewis, J. Jiang, S. Neild, C. Gong, and S. Iwnicki, "Using an inerter-based suspension to improve both passenger comfort and track wear in railway vehicles," *Vehicle System Dynamics*, pp. 1–22, 2019.

[19] F. Wang, M. Hong, and C. CW, "Building suspensions with inerters," *Proc. IMechE Part C: J. Mechanical Engineering Science*, vol. 224, pp. 1605–1616, 2009.

[20] L. Marian and A. Giaralis, "Optimal design of a novel tuned mass-damper–inerter (tmdi) passive vibration control configuration for stochastically support-excited structural systems," *Probabilistic Engineering Mechanics*, vol. 38, pp. 156–164, 2014.

[21] I. Lazar, S. Neild, and D. Wagg, "Using an inerter-based device for structural vibration suppression," *Earthquake Engineering & Structural Dynamics*, vol. 43, no. 8, pp. 1129–1147, 2014.

[22] P. Brzeski, E. Pavlovskaia, T. Kapitaniak, and P. Perlikowski, "The application of inerter in tuned mass absorber," *International Journal of Non-Linear Mechanics*, vol. 70, pp. 20–29, 2015.

[23] S. Y. Zhang, J. Z. Jiang, and S. Neild, "Optimal configurations for a linear vibration suppression device in a multi-storey building," *Structural Control and Health Monitoring*, vol. 24, no. 3, p. e1887, 2017.

[24] A. Giaralis and F. Petrini, "Wind-induced vibration mitigation in tall buildings using the tuned mass-damper-inerter," *Journal of Structural Engineering (United States)*, vol. 143, 09 2017.

[25] I. Lazar, S. Neild, and D. Wagg, "Vibration suppression of cables using tuned inerter dampers," *Engineering Structures*, vol. 122, pp. 62–71, 2016.

[26] J. Luo, J. Z. Jiang, and J. H. Macdonald, "Cable vibration suppression with inerter-based absorbers," *Journal of Engineering Mechanics*, vol. 145, no. 2, p. 04018134, 2018.

[27] D. Xin, L. Yuance, and Z. C. Michael, "Application of inerter to aircraft landing gear suspension," in *2015 34th Chinese Control Conference (CCC)*, pp. 2066–2071, IEEE, 2015.

[28] Y. Li, J. Z. Jiang, and S. Neild, "Inerter-based configurations for main-landing-gear shimmy suppression," *Journal of Aircraft*, vol. 54, no. 2, pp. 684–693, 2016.

[29] Y. Li, C. Howcroft, S. Neild, and J. Z. Jiang, "Using continuation analysis to identify shimmy-suppression devices for an aircraft main landing gear," *Journal of Sound and Vibration*, vol. 408, pp. 234–251, 2017.

[30] Y. Li, J. Z. Jiang, S. Neild, and W. Huailei, "Optimal inerter-based shock–strut configurations for landing-gear touchdown performance," *Journal of Aircraft*, vol. 54, no. 5, pp. 1901–1909, 2017.

[31] M. C. Smith and F.-C. Wang, "Performance benefits in passive vehicle suspensions employing inerters," *Vehicle system dynamics*, vol. 42, no. 4, pp. 235–257, 2004.

[32] F. Scheibe and M. C. Smith, "Analytical solutions for optimal ride comfort and tyre grip for passive vehicle suspensions," *Vehicle System Dynamics*, vol. 47, no. 10, pp. 1229–1252, 2009.

[33] A. Kuznetsov, M. Mammadov, I. Sultan, and E. Hajilarov, "Optimization of improved suspension system with inerter device of the quarter-car model in vibration analysis," *Archive of Applied Mechanics*, vol. 81, no. 10, pp. 1427–1437, 2011.

[34] C. Li, M. Liang, Y. Wang, and Y. Dong, "Vibration suppression using two-terminal flywheel. part ii: application to vehicle passive suspension," *Journal of Vibration and Control*, vol. 18, no. 9, pp. 1353–1365, 2012.

[35] Y. Hu, M. Z. Chen, and Z. Shu, "Passive vehicle suspensions employing inerters with multiple performance requirements," *Journal of Sound and Vibration*, vol. 333, no. 8, pp. 2212–2225, 2014.

[36] X. Zhang, M. Ahmadian, and K.-H. Guo, "On the benefits of semi-active suspensions with inerters," *Shock and Vibration*, vol. 19, no. 3, pp. 257–272, 2012.

[37] M. Z. Chen, Y. Hu, C. Li, and G. Chen, "Performance benefits of using inerter in semiactive suspensions," *IEEE Transactions on Control Systems Technology*, vol. 23, no. 4, pp. 1571–1577, 2015.

[38] Y. Zhang and Y. Hu, "The realization of inerter for suspension of heavy truck," in *Control Conference (CCC), 2014 33rd Chinese*, pp. 6273–6278, IEEE, 2014.

[39] S. Guo, Y. Liu, L. Xu, X. Guo, and L. Zuo, "Performance evaluation and parameter sensitivity of energy-harvesting shock absorbers on different vehicles," *Vehicle System Dynamics*, vol. 54, no. 7, pp. 918–942, 2016.

[40] C. Papageorgiou, N. E. Houghton, and M. C. Smith, "Experimental testing and analysis of inerter devices," *Journal of dynamic systems, measurement, and control*, vol. 131, no. 1, p. 011001, 2009.

[41] K. Ikago, K. Saito, and N. Inoue, "Seismic control of single-degree-of-freedom structure using tuned viscous mass damper," *Earthquake Engineering & Structural Dynamics*, vol. 41, no. 3, pp. 453–474, 2012.

[42] R. Wang, X. Meng, D. Shi, X. Zhang, Y. Chen, and L. Chen, "Design and test of vehicle suspension system with inerters," *Proceedings of the Institution of Mechanical Engineers, Part C: Journal of Mechanical Engineering Science*, vol. 228, no. 15, pp. 2684–2689, 2014.

[43] P. Brzeski, T. Kapitaniak, and P. Perlikowski, "Novel type of tuned mass damper with inerter which enables changes of inertance," *Journal of Sound and Vibration*, vol. 349, pp. 56–66, 2015.

[44] P. Brzeski, M. Lazarek, and P. Perlikowski, "Experimental study of the novel tuned mass damper with inerter which enables changes of inertance," *Journal of Sound and Vibration*, vol. 404, pp. 47–57, 2017.

[45] M. Lazarek, P. Brzeski, and P. Perlikowski, "Design and identification of parameters of tuned mass damper with inerter which enables changes of inertance," *Mechanism and Machine Theory*, vol. 119, pp. 161–173, 2018.

[46] F.-C. Wang and W.-J. Su, "Impact of inerter nonlinearities on vehicle suspension control," *Vehicle System Dynamics*, vol. 46, no. 7, pp. 575–595, 2008.

[47] F.-C. Wang, M.-F. Hong, and T.-C. Lin, "Designing and testing a hydraulic inerter," *Proceedings of the Institution of Mechanical Engineers, Part C: Journal of Mechanical Engineering Science*, vol. 225, no. 1, pp. 66–72, 2011.

[48] F.-C. Wang and H.-A. Chan, "Mechatronic suspension design and its applications to vehicle suspension control," in *2008 47th IEEE Conference on Decision and Control*, pp. 3769–3774, IEEE, 2008.

[49] M. C. Smith, "Force-controlling mechanical device," U.S. Patent 7316303, Jan. 8, 2008.

[50] R. Tuluie, "Fluid inerter," U.S. Patent App. 13/575,017, 2013.

[51] M. C. Smith, N. E. Houghton, P. J. Long, and A. R. Glover, "Force-controlling hydraulic device," U.S. Patent 18,881,876, 2014.

[52] B. J. Gartner and M. C. Smith, "Damping and inertial hydraulic device," U.S. Patent 14/635,599, 2015.

[53] T. Matsuoka, K. Hiramoto, K. Sunakoda, N. Abe, and P.-Y. Lin, "Fluid inertia damper using mr fluid with a long spiral bypass pipe," *Mechanical Engineering Journal*, vol. 3, no. 2, pp. 15–00731, 2016.

[54] N. Smith and D. Wagg, "A fluid inerter with variable inertance properties," in *Proceedings of the 6th European Conference on Structural Control, Sheffield, England*, pp. 11–13, 2016.

[55] Y. Shen, L. Chen, Y. Liu, and X. Zhang, "Influence of fluid inerter nonlinearities on vehicle suspension performance," *Advances in Mechanical Engineering*, vol. 9, no. 11, p. 1687814017737257, 2017.

[56] P. Deastra, D. J. Wagg, and N. D. Sims, "The realisation of an inerter-based system using fluid inerter," in *Dynamics of Civil Structures, Volume 2*, pp. 127–134, Springer, 2019.

[57] D. De Domenico, P. Deastra, G. Ricciardi, N. D. Sims, and D. J. Wagg, "Novel fluid inerter based tuned mass dampers for optimised structural control of base-isolated buildings," *Journal of the Franklin Institute*, 2018.

[58] B. Titurus, "Generalized liquid-based damping device for passive vibration control," *AIAA Journal*, vol. 56, no. 10, pp. 4134–4145, 2018.

[59] F.-C. Wang and H.-A. Chan, "Vehicle suspensions with a mechatronic network strut," *Vehicle System Dynamics*, vol. 49, no. 5, pp. 811–830, 2011.

[60] F.-C. Wang and S.-Y. Wu, "Vibration control of an optical table employing mechatronic inerter networks," *Journal of vibration and control*, vol. 22, no. 1, pp. 224–234, 2016.

[61] Y. Nakamura, A. Fukukita, K. Tamura, I. Yamazaki, T. Matsuoka, K. Hiramoto, and K. Sunakoda, "Seismic response control using electromagnetic inertial mass dampers," *Earthquake Engineering & Structural Dynamics*, vol. 43, no. 4, pp. 507–527, 2014.

[62] A. I. Alliance, "Annual local authority road maintenance survey 2018," *Asphalt Industry Alliance, London, UK*, 2018.

[63] D. Cebon, "Interaction between heavy vehicles and roads," tech. rep., SAE Technical Paper, 1993.

[64] T. Potter, D. Cebon, A. Collop, and D. Cole, "Road-damaging potential of measured dynamic tyre forces in mixed traffic," *Proceedings of the Institution of Mechanical Engineers, Part D: Journal of Automobile Engineering*, vol. 210, no. 3, pp. 215–225, 1996.

[65] P. Sweatman, "Effect of heavy vehicle suspensions on dynamic road loading," 1980.

[66] J. Eisenmann, "Dynamic wheel load fluctuations-road stress," *Strasse und Autobahn*, vol. 4, no. 2, pp. 127–128, 1975.

[67] D. Cole and D. Cebon, "Truck suspension design to minimize road damage," *Proceedings of the Institution of Mechanical Engineers, Part D: Journal of Automobile Engineering*, vol. 210, no. 2, pp. 95–107, 1996.

[68] D. J. Cole, "Fundamental issues in suspension design for heavy road vehicles," *Vehicle System Dynamics*, vol. 35, no. 4-5, pp. 319–360, 2001.

[69] M. Pable, M. Gawture, and P. Seshu, "A review of 'road-friendly'suspensions," in *National Conference on Mechanisms and Machines (13th NaCoMM07)*, pp. 12–13, 2007.

[70] S. Yang, S. Li, and Y. Lu, "Investigation on dynamical interaction between a heavy vehicle and road pavement," *Vehicle System Dynamics*, vol. 48, no. 8, pp. 923–944, 2010.

[71] K. Yi and J. K. Hedrick, "Active and semi-active heavy truck suspensions to reduce pavement damage," *SAE transactions*, pp. 588–595, 1989.

[72] M. Naraghi *et al.*, "Effect of heavy vehicle suspension designs on dynamic road loading–a comparative study," tech. rep., SAE Technical Paper, 2001.

[73] D. Simon and M. Ahmadian, "Vehicle evaluation of the performance of magneto rheological dampers for heavy truck suspensions," *Journal of Vibration and Acoustics*, vol. 123, no. 3, pp. 365–375, 2001.

[74] H. Yarmohamadi and V. Berbyuk, "Kinematic and dynamic analysis of a heavy truck with individual front suspension," *Vehicle System Dynamics*, vol. 51, no. 6, pp. 877–905, 2013.

[75] G. Xu, N. Zhang, and H. M. Roser, "Roll and pitch independently tuned interconnected suspension: modelling and dynamic analysis," *Vehicle System Dynamics*, vol. 53, no. 12, pp. 1830–1849, 2015.

[76] L. R. C. Drehmer, W. J. Paucar Casas, and H. M. Gomes, "Parameters optimisation of a vehicle suspension system using a particle swarm optimisation algorithm," *Vehicle System Dynamics*, vol. 53, no. 4, pp. 449–474, 2015.

[77] Z. Yin, A. Khajepour, D. Cao, B. Ebrahimi, and K. Guo, "A new pneumatic suspension system with independent stiffness and ride height tuning capabilities," *Vehicle system dynamics*, vol. 50, no. 12, pp. 1735–1746, 2012.

[78] D. A. Mántaras and P. Luque, "Virtual test rig to improve the design and optimisation process of the vehicle steering and suspension systems," *Vehicle system dynamics*, vol. 50, no. 10, pp. 1563–1584, 2012.

[79] J. J. Zhu, A. Khajepour, E. Esmailzadeh, and A. Kasaiezadeh, "Ride quality evaluation of a vehicle with a planar suspension system," *Vehicle system dynamics*, vol. 50, no. 3, pp. 395–413, 2012.

[80] M. Alghafir and J. Dunne, "A narx damper model for virtual tuning of automotive suspension systems with high-frequency loading," *Vehicle system dynamics*, vol. 50, no. 2, pp. 167–197, 2012.

[81] M. Čorić, J. Deur, L. Xu, H. E. Tseng, and D. Hrovat, "Optimisation of active suspension control inputs for improved vehicle ride performance," *Vehicle system dynamics*, vol. 54, no. 7, pp. 1004–1030, 2016.

[82] M. Čorić, J. Deur, J. Kasać, H. E. Tseng, and D. Hrovat, "Optimisation of active suspension control inputs for improved vehicle handling performance," *Vehicle system dynamics, International Journal of Vehicle Mechanics and Mobility*, vol. 54, no. 11, pp. 1574–1600, 2016.

[83] H. Ren, S. Chen, Y. Zhao, G. Liu, and L. Yang, "State observer-based sliding mode control for semi-active hydro-pneumatic suspension," *Vehicle System Dynamics*, vol. 54, no. 2, pp. 168–190, 2016.

[84] J. Michael and M. Gerdts, "Pro-active optimal control for semi-active vehicle suspension based on sensitivity updates," *Vehicle System Dynamics*, vol. 53, no. 12, pp. 1721–1741, 2015.

[85] H. Du, N. Zhang, and L. Wang, "Switched control of vehicle suspension based on motion-mode detection," *Vehicle System Dynamics*, vol. 52, no. 1, pp. 142–165, 2014.

[86] H. Chen, C. Long, C.-C. Yuan, and H.-B. Jiang, "Non-linear modelling and control of semi-active suspensions with variable damping," *Vehicle System Dynamics*, vol. 51, no. 10, pp. 1568–1587, 2013.

[87] O. M. Anubi and C. D. Crane III, "A new active variable stiffness suspension system using a nonlinear energy sink-based controller," *Vehicle System Dynamics*, vol. 51, no. 10, pp. 1588–1602, 2013.

[88] M. Rahman and G. Rideout, "Using the lead vehicle as preview sensor in convoy vehicle active suspension control," *Vehicle system dynamics*, vol. 50, no. 12, pp. 1923–1948, 2012.

[89] L.-H. Zong, X.-L. Gong, C.-Y. Guo, and S.-H. Xuan, "Inverse neuro-fuzzy mr damper model and its application in vibration control of vehicle suspension system," *Vehicle system dynamics*, vol. 50, no. 7, pp. 1025–1041, 2012.

[90] S. B. A. Kashem, M. Ektesabi, and R. Nagarajah, "Comparison between different sets of suspension parameters and introduction of new modified skyhook control strategy incorporating varying road condition," *Vehicle system dynamics*, vol. 50, no. 7, pp. 1173–1190, 2012.

[91] M. Ahmadian and C. A. Pare, "A quarter-car experimental analysis of alternative semiactive control methods," *Journal of Intelligent Material Systems and Structures*, vol. 11, no. 8, pp. 604–612, 2000.

[92] D. Cao, X. Song, and M. Ahmadian, "Editors' perspectives: road vehicle suspension design, dynamics, and control," *Vehicle system dynamics*, vol. 49, no. 1-2, pp. 3–28, 2011.

[93] K. Kamash and J. Robson, "The application of isotropy in road surface modelling," *Journal of Sound and Vibration*, vol. 57, no. 1, pp. 89–100, 1978.

[94] D. Newland *et al.*, "Random vibrations and spectral analysis," *Longmann, New York, London*, 1975.

[95] P. Fancher, R. Ervin, C. MacAdam, and C. Winkler, "Measurement and representation of the mechanical properties of truck leaf springs," tech. rep., SAE Technical Paper, 1980.

[96] A. Heath, "Application of the isotropic road roughness assumption," *Journal of Sound and Vibration*, vol. 115, no. 1, pp. 131–144, 1987.

[97] F. Yu and Y. Lin, "Vehicle system dynamics and control," *Machine Press, Beijing, China*, 2005.

[98] S. Karamihas and T. Gillespie, "Characterizing trucks for dynamic load prediction," *International Journal of Heavy Vehicle Systems*, vol. 1, no. 1, pp. 3–19, 1993.

[99] Y. J. Lu, S. H. Li, C. Y. Wang, and S. Y. Li, "Research on test and parameter identification for nonlinear stiffness characteristics of leaf spring," in *Advanced Materials Research*, vol. 602, pp. 460–463, Trans Tech Publ, 2013.

[100] E. Guillemin, "A summary of modern methods of network synthesis," in *Advances in Electronics and Electron Physics*, vol. 3, pp. 261–303, Elsevier, 1951.

[101] B. Titurus, J. D. Bois, and N. Lieven, "Modeling and testing of a semiactive hydraulic damper in periodic working regimes," *AIAA journal*, vol. 50, no. 4, pp. 844–854, 2012.

[102] H. Merritt, H. E. Merritt, and H. E. Merritt, "Hydraulic control systems," *John Wiley & Sons*, 1967.

[103] B. Titurus and N. Lieven, "Modeling and analysis of semi-active dampers in periodic working environments," *AIAA Journal*, vol. 47, no. 10, pp. 2404–2416, 2009.

[104] J. Schönfeld, "Analogy of hydraulic, mechanical, acoustic and electric systems," *Applied Scientific Research, Section A*, vol. 3, no. 1, pp. 417–450, 1954.

[105] W. C. Flower, "Understanding hydraulic mounts for improved vehicle noise, vibration and ride qualities," *SAE transactions*, pp. 832–841, 1985.

[106] R. Singh, G. Kim, and P. Ravindra, "Linear analysis of automotive hydro-mechanical mount with emphasis on decoupler characteristics," *Journal of sound and vibration*, vol. 158, no. 2, pp. 219–243, 1992.

[107] J. Z. Jiang and M. C. Smith, "Regular positive-real functions and five-element network synthesis for electrical and mechanical networks," *IEEE Transactions on Automatic Control*, vol. 56, no. 6, pp. 1275–1290, 2011.

[108] X. Liu, J. Z. Jiang, B. Titurus, and A. Harrison, "Model identification methodology for fluid-based inerters," *Mechanical Systems and Signal Processing*, vol. 106, pp. 479–494, 2018.

[109] B. Kumar, N. Nordi, B. Quayle, and M. Wright, "The design, testing and modelling of fluid inerters," 2016.

[110] J. Pfitzner, "Poiseuille and his law," *Anaesthesia*, vol. 31, no. 2, pp. 273–275, 1976.

[111] M. Hino, M. Sawamoto, and S. Takasu, "Experiments on transition to turbulence in an oscillatory pipe flow," *Journal of Fluid Mechanics*, vol. 75, no. 2, pp. 193–207, 1976.

[112] M. OHMI and M. Iguchi, "Critical reynolds number in an oscillating pipe flow," *Bulletin of JSME*, vol. 25, no. 200, pp. 165–172, 1982.

[113] M. Ohmi, M. Iguchi, and I. Urahata, "Flow patterns and frictional losses in an oscillating pipe flow," *Bulletin of JSME*, vol. 25, no. 202, pp. 536–543, 1982.

[114] L. Fishler and R. Brodkey, "Transition, turbulence and oscillating flow in a pipe a visual study," *Experiments in fluids*, vol. 11, no. 6, pp. 388–398, 1991.

[115] G. F. Franklin, J. D. Powell, A. Emami-Naeini, and J. D. Powell, "Feedback control of dynamic systems," *Addison-Wesley Reading, MA*, vol. 3, 1994.

[116] A. Marazzi, "Algorithms, routines, and s-functions for robust statistics," *CRC Press*, 1993.

[117] D. C. Rennels and H. M. Hudson, "Pipe flow: A practical and comprehensive guide," *John Wiley & Sons*, 2012.

[118] S. Liu, A. Afacan, H. A. Nasr-El-Din, and J. H. Masliyah, "An experimental study of pressure drop in helical pipes," *Proceedings of the Royal Society of London. Series A: Mathematical and Physical Sciences*, vol. 444, no. 1921, pp. 307–316, 1994.

[119] S. Ali, "Pressure drop correlations for flow through regular helical coil tubes," *Fluid dynamics research*, vol. 28, no. 4, p. 295, 2001.

[120] S. Rodman and F. Trenc, "Pressure drop of laminar oil-flow in curved rectangular channels," *Experimental thermal and fluid science*, vol. 26, no. 1, pp. 25–32, 2002.

[121] C. White, "Friction factor and its relation to heat transfer," *Trans. Inst. Chem. Eng.*, vol. 18, pp. 66–68, 1932.

[122] B. S. Massey and J. Ward-Smith, "Mechanics of fluids," *Crc Press*, vol. 1, 1998.

[123] A. A. Geisberger, "Hydraulic engine mount modeling, parameter identification and experimental validation," *University of Waterloo Ontario*, 2000.

[124] MATLAB, "Simulink," *Ver. 8.1, Math Works, Natick, MA*, 2008.

[125] G. Kerschen, K. Worden, A. F. Vakakis, and J.-C. Golinval, "Past, present and future of nonlinear system identification in structural dynamics," *Mechanical systems and signal processing*, vol. 20, no. 3, pp. 505–592, 2006.

[126] L. Ljung, "System identification: Theory for the user," *New Jersey: Prentice-Hall Inc.*, 1987.

[127] J. Z. Jiang, M. C. Smith, and N. E. Houghton, "Experimental testing and modelling of a mechanical steering compensator," in *2008 3rd International Symposium on Communications, Control and Signal Processing*, pp. 249–254, IEEE, 2008.

[128] B. Titurus, J. Du Bois, N. Lieven, and R. Hansford, "A method for the identification of hydraulic damper characteristics from steady velocity inputs," *Mechanical systems and signal processing*, vol. 24, no. 8, pp. 2868–2887, 2010.

[129] D. M. Ford, "An analysis and application of a decoupled engine mount system for idle isolation," tech. rep., SAE Technical Paper, 1985.

[130] B. Titurus, "Complete semi-analytical damper model identification using triangular displacement inputs," *Proceedings of ISMA2014 including USD2014*, pp. 3179–3188, 2014.

[131] H. Ito, "Friction factors for turbulent flow in curved pipes," *Trans. ASME, J. Basic Engng, D*, vol. 81, pp. 123–134, 1959.

[132] H. Inc, "Catalogue 79352 eng hoke needle valves 10.15.13," 2018.

[133] A. Ghosh, V. Verma, and H. Kushwaha, "Evaluation of dynamic stiffness and damping factor of a hydraulic damper," tech. rep., Bhabha Atomic Research Centre, 2000.